THE EFFECT OF ION TRANSPORT AND ELECTROLYTE RHEOLOGY ON MORPHOLOGICAL INSTABILITIES IN ELECTRODEPOSITION

A Dissertation

Presented to the Faculty of the Graduate School

of Cornell University

In Partial Fulfillment of the Requirements for the Degree of

Doctor of Philosophy

by

Mukul Tikekar

August 2017

THE EFFECT OF ION TRANSPORT AND ELECTROLYTE RHEOLOGY ON MORPHOLOGICAL INSTABILITIES IN ELECTRODEPOSITION

Mukul Tikekar, Ph. D.

Cornell University 2017

Morphological instabilities in electrodeposition have long been studied due to their important applications in electroplating and energy storage. They are receiving increased attention due to their prevalence in batteries with lithium metal anodes which are critical to next generation energy storage devices. These instabilities are driven by preferential charge transport across an electrolyte to the tips of perturbations to the metal surface.

Using linear stability analysis, four models are developed to study the growth of morphological instabilities in electrodeposition under the action of various driving forces. The first model considers the ion transport across an electrolyte with fixed anions and demonstrates that spatial immobilization of anions can significantly reduce the electric field at the metal surface. The following model develops a framework to include the mechanical response of an elastic solid separator, which is then used to show that the combined effect of reduced electric field and elasticity-induced suppression can stabilize the deposition at all length scales. The next idea investigates the effect of an interfacial layer and yields that homogenization of cation concentration at the metal surface by lateral transport can weaken the growth of the instability. Finally, polymer additives are studied as a means to stabilize electroconvection-induced destabilization of the metal surface.

BIOGRAPHICAL SKETCH

Mukul Tikekar was born, brought up, and educated in Mumbai, India. From 2006 to 2011, he attended the Dual Degree program in Mechanical Engineering at the Indian Institute of Technology Bombay. His Masters dissertation was titled “Blood flow in stenosed and bifurcating microchannels”, and experimentally studied the steady and pulsatile flow characteristics of water and blood in microchannels with stenosed and bifurcating geometries.

In 2011, he joined Cornell University as a Ph.D. student in the Sibley School of Mechanical and Aerospace Engineering. Under the guidance of Prof. Donald Koch and Prof. Lynden Archer, he has since studied the morphological instabilities in electrodeposition, particularly focused on the recharge process in lithium metal batteries and devising strategies to suppress the formation of lithium dendrites. His research interests are modeling and simulation of physical and chemical phenomena in polymers and complex fluids and lies at the intersection of such fields as fluid mechanics, polymer dynamics, rheology, and ion transport.

In Fall 2017, he will join the group of Prof. Glenn Fredrickson at University of California, Santa Barbara as a postdoctoral scholar to study non-equilibrium phenomena and phase behavior in macromolecular systems.

Dedicated to my family

ACKNOWLEDGMENTS

I am indebted to my advisors Prof Donald Koch and Prof Lynden Archer for all the guidance, encouragement and mentorship throughout the PhD process. It has taken significant effort on their part to help me with the transition from an experimental fluid dynamics background to a theoretical transport and rheology researcher. I would also like to thank Prof Brian Kirby for all the feedback and information to fill out gaps in my knowledge, and to Prof Claude Cohen who helped with the understanding of several concepts in polymer physics that were used in the final project.

I am grateful to many colleagues in the Koch and Archer groups who have provided many directions for personal and professional growth as well as fruitful discussions – Jennifer Schaefer, Yingying Lu, Snehashis Choudhury, Zhengyuan Tu, Pooja Nath, Shuya Wei, Lin Ma, and Rahul Mangal, who introduced me to many of concepts in the field of polymer physics. I'm confident that the future of this project rests in the capable hands of Alex Warren and Gaojin Li, who will take it to greater heights. I am thankful for the mentorship of Prof Charles Williamson, Prof Tom Avedisian, Prof Donald Koch and Prof Roseanna Zia for helping me improve my teaching skills. I would like to mention the assistance of Marcia Sawyer, assistant DGS at the Sibley School of Mechanical and Aerospace Engineering, and the office staff of Olin Hall for all their help with the procedural duties necessary throughout the six years at Cornell. My Cornell experience would be incomplete without all the friends who made life in Ithaca all the more enjoyable.

Finally, I'd like to thank my parents and my brother for their support and their constant efforts to try to understand what it is that I do.

This material is based on work supported by the Energy Materials Center at Cornell, an Energy Frontier Research Center funded by the U.S. Department of Energy, Office of Science, and Office of Basic Energy Sciences under Award Number DESC0001086, the KAUST Cornell Center for Energy and Sustainability, which is supported by the King Abdullah University of Science and Technology (KAUST) through Award # KUSC1–018–02.

TABLE OF CONTENTS

Biographical sketch iv
Dedication v
Acknowledgements vi
Table of contents viii
List of figures x
List of tables xiii
List of abbreviations xiv
Preface xv
1 Introduction 1
1.1 Three schools of thought about Li dendrite formation 5
1.1.1 Unstable ion transport drives unstable deposition 5
1.1.2 Mechanically weak separators facilitate growth 6
1.1.3 Unregulated surface reactions nucleate dendrites 6
1.2 Experimental approaches 8
1.2.1 Modifying ion transport in electrolytes 8
1.2.2 Improving mechanics 10
1.2.3 Creating artificial SEI 11
1.3 Theoretical and simulation studies 13
1.3.1 Linear stability analysis 14
1.3.2 Phase field simulations 15
1.3.3 Diffusion-limited aggregation 16
1.3.4 Electroconvection 17
1.4 Summary and scope 17
References 19

2 The tethered anion electrolyte 25
2.1 Model for the tethered anion electrolyte 27
2.1.1 Large current densities 35
2.1.2 Small current densities 38
2.2 Linear stability analysis 38
2.2.1 Large current densities 40
2.2.2 Small current densities 43
2.3 Conclusion 47
References 51

3 Elastic deformation of the tethered anion electrolyte 53
3.1 The transport problem 53
3.2 The deformation problem 56
3.3 Linear stability analysis 60
3.3.1 Large current densities 61
3.3.2 Small current densities 72
3.3.3 Dimensional analysis 76

3.3.4 Marginal stability 84
3.4 Conclusions 88
References 92

4 Diffusion of ions in and elasticity of the interfacial layer 95
4.1 Interfacial diffusion 97
4.1.1 Linear stability 99
4.2 Interfacial layer elasticity 102
4.3 Conclusions 103
References 105

5 Electroconvection with polymer additives 106
5.1 The two-fluid model and transport equations 107
5.2 Base state 114
5.3 Linear stability analysis at low current densities 117
5.4 Electroconvection at high current densities 123
5.5 Conclusion 131
References 132

6 Concluding remarks 134
References 137

Appendix 138

LIST OF FIGURES

1.1 Schematic illustrating different stages of dendrite growth on a planar Li metal surface. For less reactive metals, the passivation layer is absent. However, Stages II and III remain as before. 3

1.2 Summary of the literature on dendrite suppression strategies that tracks the three practiced methods discussed in the text 8

2.1 The proposed fixed anion electrolyte to stabilize the electrodeposition (a) An illustration of the electrolyte. The large blue circles represent the fixed anions and comprise a fraction C_a^f of the total number of anions (b) A porous matrix implementation of the fixed anion electrolyte (c) Nanoparticles with tethered anions used by Schaefer et al 26

2.2 Conductivity of the fixed anion electrolyte as a function of overpotential and fraction of fixed anions 31

2.3 Base state solution to the transport problem at steady state (a) Cation concentration profiles, (b) Electrical potential profiles, and (c) Electric field profiles at various current densities for $C_a^f = 0.1$. The dashed black line corresponds to the critical current density while the dashed gray line corresponds to the two-region approximation for $JL/D_cFC_0 = 7.2$. 32

2.4 Critical overpotential as a function of fixed anion proportion 33

2.5 Electric field at the metal electrode as a function of fraction of fixed anions. The various curves are for different values of FV_0/RT going from bottom to top as, 0.5 (solid black), 1, 2, 3, 5, 10, 20 (solid gray). 34

2.6 An illustration of the approximate model at high current densities (a) Base state and (b) The sinusoidally perturbed electrodes used in the stability analysis 38

2.7 Growth rate of perturbations of varying wavenumbers at high current densities ($FV_0/RT = 11$; or $V_0 = 275$ mV). The solid black line is obtained by performing a stability analysis on the base state solution given by Chazalviel, while the dashed black line is the result for single-ion conductor 43

2.8 Base state and the sinusoidally perturbed electrodes used in the stability analysis at low current densities 44

2.9 Growth rate of perturbations of varying wavenumbers at low current densities ($FV_0/RT = 1$; or $V_0 = 25$ mV). The result for single-ion conductor (black dashed line) is obtained from the large current densities analysis since transport in single-ion conductors is always driven by migration 46

2.10 Two important parameters of the stability analysis. (a) Critical wavenumber and (b) Growth rate of most unstable mode at varying overpotentials for various fixed anion fractions. 47

3.1 An approximate solution to the base state problem at steady state for: (a) High current densities and, (b) Low current densities, as shown in a

previous work. Above the critical current density $J_{cr} = 4D_cFC_0(1 - 2C_{a,f0})/L$, the migration region which is devoid of mobile anions forms near the metal electrode. The same solution is valid even with the inclusion of pressure gradient driven transport, since pressure in the separator is uniform in the base state. 60

3.2 Base state solution to the steady state transport problem: (a) Cation concentration, (b) Electric potential, and (c) Electric field profiles. The fraction of immobilized anions $C_{a,f0}$ is 0.1, yielding a critical current density J_{cr} of $3.2D_cFC_0/L$. The profiles at the critical current density are indicated by the solid black lines. 60

3.3 (a) Base state and (b) perturbed state of the problem at high current densities 63

3.4 Large current density growth rate vs wavenumber plots for (a) $C_{a,f0} = 0.1$ with varying G^s, and (b) $G^s = 1$MPa with varying $C_{a,f0}$. The black line in Fig 3.4a corresponds to the result with elasticity excluded and only the effect of surface tension being considered. 70

3.5 (a) Critical wavenumber and (b) Growth rate of the most unstable mode as a function of separator shear modulus for various fractions of immobilized anions 72

3.6 (a) Base state and (b) perturbed state of the problem at low current densities 73

3.7 Growth rate as a function of wavenumber for (a) $C_{a,f0} = 0.1$ with varying G^s, and (b) $G^s = 1$MPa with varying $C_{a,f0}$ at small current densities. 74

3.8 (a) Critical wavenumber and (b) Growth rate of the most unstable mode as a function of separator shear modulus for various fractions of immobilized anions at small current densities. 75

3.9 Critical wavenumber vs current density for (a) $C_{a,f0} = 0.1$ with varying G^s, and (b) $G^s = 1$MPa with varying $C_{a,f0}$ 76

3.10 Dominant mechanism in the stability of electrodeposition at various dimensionless wavenumbers and separator moduli for (a) small current densities and (b) large current densities. The shaded region is unstable. See text for the definitions of the various dimensionless groups. 80

3.11 Marginal stability curves – Relation between separator modulus and current density at varying fixed anion fractions for which the deposition is stable for all modes. The deposition is fully stable at any point to the right of the corresponding curve. 88

3.12 (a) Marginal stability curves for $C_{a,f0} = 0.1$ and $\nu^s = 0.33$ for various values of cation partial molar volume. The partial molar volumes of the mobile anion ($v_{a,m}$) and the metal (v_m) are held constant at 1.78×10^{-4} m^3/mol and 1.3×10^{-5} m^3/mol respectively. (b) Marginal stability for $C_{a,f0} = 0.1$, $v_c = -8 \times 10^{-6}$ m^3/mol, $v_{a,m} = 1.78 \times 10^{-4}$ m^3/mol, and $v_m = 1.3 \times 10^{-5}$ m^3/mol, for various values of separator Poisson ratio. 91

4.1 A schematic illustration of the two-step process model 97

4.2 Perturbation growth rate versus wavenumber for (a) infinite Da and

varying Ld and (b) zero Ld and varying Da 101
4.3 Shear mode deformation of the interfacial layer for small deposits can be seen from the change in the shape of the dashed square 103

5.1 Cation and anion concentration, electric potential and polymer volume fraction profiles for $FV_0/RT = 4$ at current densities below the diffusion limit, $\phi_0 = 0.05$ (a) $\Lambda = -0.73\times10^{-10}$ C/m, i.e. n = 2, $z_P = -1$ and (b) $\Lambda = 0.73\times10^{-10}$ C/m, i.e. n = 2, $z_P = +1$. The metal electrode is at z = 0. 117
5.2 (a) Critical current density and (b) Critical transport overpotential for depletion of negatively charged polymer with $z_P = -1$ at the metal electrode as a function of volume fraction for various values of n. 117
5.3 Growth rate versus wavenumber for $z_P = -1$ and varying values of (a) Equilibrium polymer concentration ϕ_0 with n = 2 and (b) $\phi_0 = 0.05$ and varying values of n. 123
5.4 Salt concentration profile at increasing times. The current density considered here is four times the diffusion limit. The black line shows the profile at Sand's time. 125
5.5 Linear growth rates of the purely electroconvective and electroconvective and morphological instabilities in a Newtonian fluid 130
5.6 Growth rate versus wavenumber varying values of (a) Polymerization index N at $\phi_0 = 0.05$ and (b) Volume fraction ϕ_0 for N = 2000. 130

A1 Transient concentration profiles at 3/4th the diffusion limit 138
A2 Concentration at the metal electrode over time 138

LIST OF TABLES

3.1	Transport mechanisms and their stabilizing behavior, based on parameter values used in Table 3.2	67
3.2	Standard parameter values	68

LIST OF ABBREVIATIONS

Lithium ion battery	LIB
Lithium metal battery	LMB
Solid electrolyte interphase	SEI
Monroe-Newman	M-N
Joint density functional theory	JDFT
Density functional theory	DFT
Coulombic efficiency	CE
Diffusion limited aggregation	DLA

PREFACE

The best way to read this dissertation is to not read it at all. All of the work herein appears in the journal articles: MD Tikekar, S Choudhury, Z Tu, and LA Archer, 2016, *Nature Energy*, **1**, 16114 (Parts of Chapter 1); MD Tikekar, LA Archer, and DL Koch, 2014, *Journal of the Electrochemical Society*, **161 (6)**, A847 (Part of Chapter 1, and Chapter 2); and MD Tikekar, LA Archer, and DL Koch, 2016, *Science Advances*, **2 (7)**, e1600320 (Part of Chapter 1, and Chapter 3). The remaining chapters will be published in due course and may be found on the author's Google Scholar page.

Nonetheless, an intrepid reader might want to take stock of additional matter included in the Introduction to get a broad sense of the author's views on the subject, particularly on the topic of theoretical and simulation studies of dendritic electrodeposition which was excluded from the article in Nature Energy.

Final warning, it gets pretty boring pretty fast. Please turn back now.

CHAPTER 1

INTRODUCTION

The instability of a planar surface during electrodeposition has been long studied among the classical morphological instabilities in material science. It has received renewed recent interest due to its relevance to rechargeable batteries that use metallic anodes. Lithium metal batteries (LMBs), known for their very high energy storage capacities, are susceptible to dendrite formation and internal shorting on recharging due to unstable electrodeposition on the lithium metal electrode [1, 2]. Although lithium-ion batteries (LIBs) are designed to eliminate this problem by hosting the lithium in a carbon substrate, the potential difference (< 100 mV) separating lithium intercalation versus lithium plating onto graphite is so small that a too quickly charged or overcharged LIB may just as easily fail by dendrite nucleation, growth and short circuits as a LMB [3]. This possibility has fueled interest in new experiments and theoretical approaches that can inform strategies to inhibit dendritic growth.

Dendrite proliferation is understood to be a key limiting factor affecting next generation battery chemistries such as Li-S [4] and Li-O_2 [5], which are gaining research interest due to their high energy storage capacities and low cost. Sulfur, for example, has the highest theoretical capacity among all the solid state cathode materials, thus making the Li-S chemistry an attractive battery design [4]. Li-O_2 batteries have theoretical capacities of around 11,680 Wh/kg, which are comparable to the theoretical energy density of gasoline, which makes it a strong candidate for automotive

applications [5]. Although much of the current research focuses on improving the cathode architecture and composition for enhancing cycle life and efficiency, a lithiated cathode is required for cell operation and a metallic lithium cathode is essential for achieving the high theoretical capacities offered by both chemistries. This means that Li-S and Li-O_2 batteries are vulnerable to failure by short circuit due to dendritic growth on the recharge cycle.

Dendritic deposition typically progresses in three stages (Fig 1.1). In the first stage, microscopic seeds nucleate on the metal surface, acting as points of local deposition. In transition metals such as copper, zinc, nickel etc., nucleation takes place due to depletion of the salt near the metal surface on polarization [6,7]. Highly reactive metals such as lithium and sodium react parasitically with the electrolyte to form a thin passivation layer called the solid-electrolyte-interphase (SEI) on the metal surface. Inhomogeneities in the SEI present as a result of its spontaneous formation are also a source of nucleation. Continual deposition on these nuclei leads to initiation of dendrites by growth of the seeds. The growth of the nuclei is driven by the transport of ions in deposition and resisted by thermodynamic factors such as surface tension of the metal-electrolyte interface, which favors a low surface area, homogeneous deposition. On further deposition on the nuclei, the dendrites undergo accelerated growth to form macroscopic structures, which exhibit a variety of morphologies from moss-like aggregates at low current densities to thin needles at high current densities [8]. These structures pierce through the separator and bridge the inter-electrode gap causing short circuits. This growth is highly nonlinear and unrestrained. Thus, dendritic deposition is difficult to control in the first nucleation and the final

accelerated growth stages. It is therefore, more effective to address the problem in the second stage, viz. growth of nuclei.

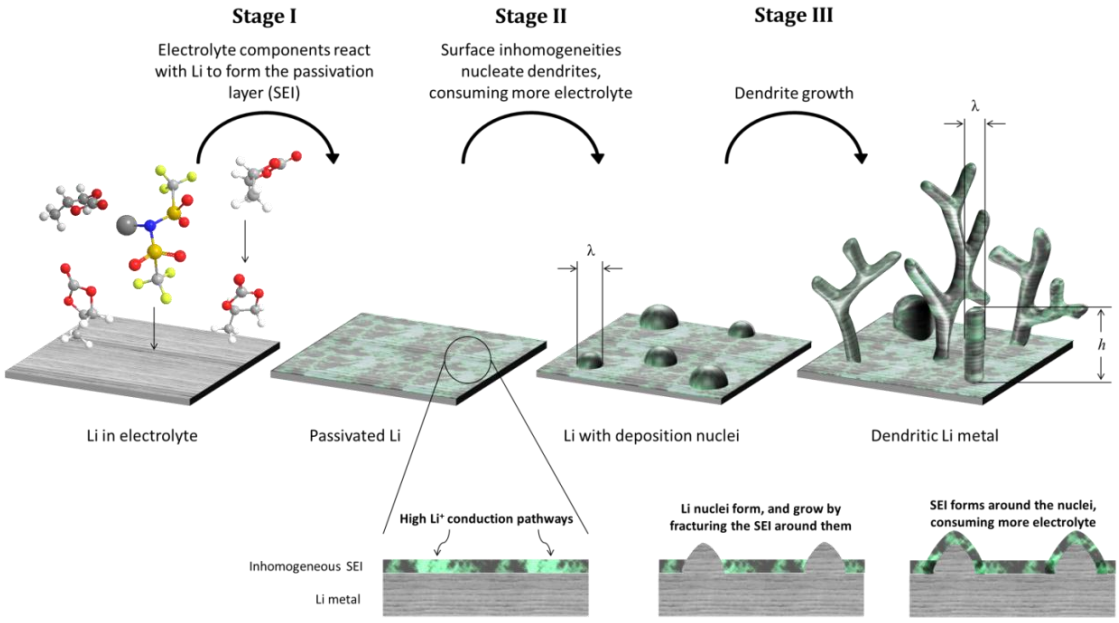

Figure 1.1: Schematic illustrating different stages of dendrite growth on a planar Li metal surface. For less reactive metals, the passivation layer is absent. However, Stages II and III remain as before.

The mechanism of dendrite growth has quite fundamental physical origins. At low current densities, concentration of electric field lines and preferential transport of ions to rough regions on the electrode surface produce a morphological instability. Whereas, at high current densities, depletion of anions in the electrolyte near the anode creates a space charge that drives a hydrodynamic instability termed electro-convection [9]. (This depletion does not occur at low current densities. See Appendix.) This electro-convection draws ions away from regions surrounding a growing dendrite and focuses them on the dendrite tip, enhancing dendrite growth. Thus, for quite

fundamental physical reasons, recharge of a LMB at either low or high currents produces rough/dendritic deposition of the metal. Reactivity of Li with commonly used aprotic liquid electrolytes also favors spontaneous, parasitic chemical reactions to form a porous, ion-conducting solid electrolyte interphase (SEI) layer on the metal [10]. A uniform and stable SEI can passivate the Li surface, preventing further reaction between the bulk lithium and electrolyte, but spontaneously formed SEIs on Li are typically inhomogeneous and mechanically fragile. An inhomogeneous SEI creates spatial variations in interfacial resistance to Li-ion transport across the electrolyte-electrode interface, which provides nucleation sites for dendrite formation at any current density, while a fragile SEI may crack or delaminate during battery cycling, exposing fresh Li to the electrolyte each cycle. Because the two processes (dendrite formation and electrolyte loss) occur in tandem, it is a formidable challenge to create a LMB that cycles stably.

The factors affecting dendritic deposition of highly reactive metals being a superset of those involved in electrodeposition, motivates an approach where a study of highly reactive metals only will provide useful lessons for the process of electrodeposition in general. To that end, we will continue to look at dendrite formation in Li as a tool to study the roles of transport, rheological and interfacial effects in electrodeposition. It is, however, important to remember the general nature of the results so obtained. We will first look at the three guiding principles for these efforts, followed by a short review of the experimental techniques used to realize the suggested routes, and finally address the theoretical studies of the subject.

1.1 Three schools of thought about Li dendrite formation

The literature on dendrite suppression in Li metal derives its motivation from three ideas in general.

1.1.1 Unstable ion transport drives unstable deposition

Much of the initial effort to stabilize the Li anode sought to take advantage of principles borrowed from the field of electrodeposition, where significant efforts have been given to eliminating rough deposition of metals such as Zn, Ni, Pb, Cu, etc. In most cases, these metals form dendrites when the current density approaches the limiting value beyond which diffusion is unable to replenish ions depleted from regions in an electrolyte by electromigration [11]. Chazalviel and coworkers [12] studied the transport processes in dilute electrolytes that lead to space-charge formation and showed that dendrites begin to nucleate at the Sand's time, which scales inversely as the anion transference number squared. Thus, the nucleation of dendrites may be delayed – in principle indefinitely, in electrolytes for which the anion transference number is zero or in which a supporting electrolyte is present in high concentration.[13]

The requirements for stabilizing the Li anode are in reality more complex as revealed by other works [14, 15] that consider the effect of other factors such as surface tension and the nature of ion transport in an electrolyte on dendrite growth at low and high current densities. A common methodology is to analyze the growth of small sinusoidal perturbations to the electrode surface, with current density driving roughening and surface tension resisting roughening. This analysis reveals that

dendrite growth is suppressed under a range of conditions, including at low current density and in electrolytes with high surface tension, high Li^+ transference number, and high ionic conductivity.[15]

1.1.2 Mechanically weak separators facilitate growth

While modification of transport and improvement of surface tension can suppress dendrite growth, they cannot eliminate it in liquid electrolytes. The analytical work of Monroe and Newman (M-N)[16] introduced the idea that dendrite growth may be stopped completely using a mechanically strong separator. By evaluating the effect of elastic deformation of the electrode and separator on the deposition reaction kinetics, the authors found that non-uniform Li deposition is completely arrested when the condition $G > 1.8G_{Li}(T)$ is met. Here G and G_{Li} are, respectively, the shear modulus of the separator and metallic lithium. This condition is met for $G \approx 6$ GPa at room temperature, but could be achieved at much lower separator modulus as one approaches the melting temperature ($T = 180.5°C$) of Li. To our knowledge only one study has attempted to evaluate this prediction quantitatively.[17] The guidance provided by the M-N analysis is nonetheless intuitive, which has fuelled a common perception that a solid-state electrolyte-separator with high modulus is a requirement for a practical room-temperature lithium metal battery.

1.1.3 Unregulated surface reactions nucleate dendrites

The approaches discussed thus far assume that even at the moderate current densities where most batteries are operated, the morphology of the Li anode makes it

prone to failure. They are silent however on the important role the surface reactivity Li plays. Work by Aurbach [10], shows that none of the commonly used liquid electrolytes are stable in contact with Li and all form a resistive passivation layer that is typically heterogeneous and unstable. Significant effort has therefore been placed on creating artificial SEIs, either designed ex-situ or formed in-situ by electrolyte additives that stabilizes the interface by preventing over-exposure of the Li anode to electrolyte.

Recent Joint Density Functional Theoretical (JDFT) calculations[18] show that a cleverly engineered SEI can not only control Li surface reactivity, but may also be used to alter Li-ion transport and surface tension. In particular, the analysis shows that energy barriers E_a for Li^+ diffusion at the anode are substantially lower in a SEI composed of halide salts (e.g. $E_{a,LiBr} \approx 0.03$ eV; $E_{a,LiF} \approx 0.16$ eV), compared to an SEI comprised of Li_2CO_3 ($E_{a,Li2CO3} \approx 0.24$ eV), which forms naturally when aprotic solvents react with Li. This difference means that at any current density, ions can more easily rearrange before deposition on a Li electrode passivated with a thin halide salt SEI. An important achievement of the JDFT analysis is that it explains why electrodes based on Mg, which possesses low barriers for surface diffusion and exceptionally high surface energies, do not form dendrites [19].

We will next take a look at how these lessons influence the experimental studies of the subject.

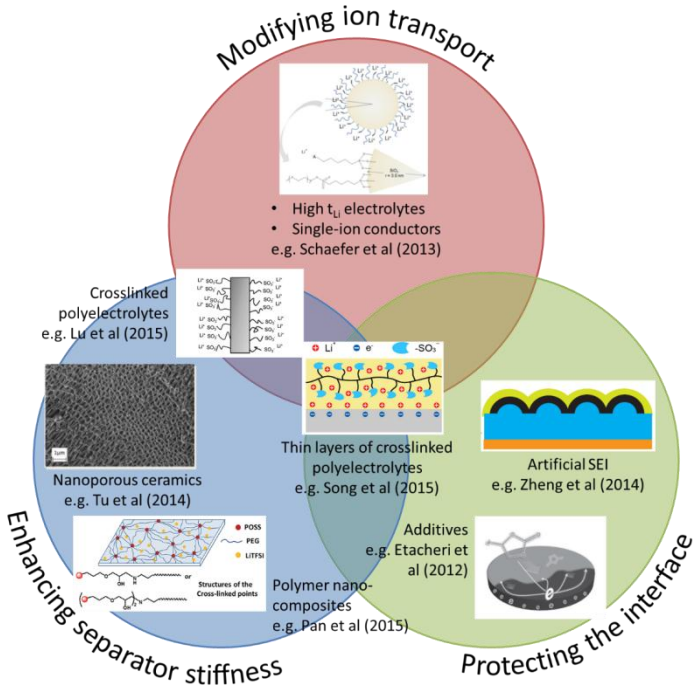

Figure 1.2: Summary of the literature on dendrite suppression strategies that tracks the three practiced methods discussed in the text

1.2 Experimental approaches

All of the approaches discussed in the previous section have been practiced to an extent (Fig 1.2), but this is often done without explicit knowledge of the principles that underpin the method's effectiveness. An undesirable consequence is that most studies focus on one approach to the exclusion of others.

1.2.1 Modifying ion transport in electrolytes

Inorganic glasses such as lithium phosphorus oxynitride ($Li_{2.9}PO_{3.3}N_{0.46}$; LiPON) [20] and solid solutions such as $Li_{4-x}Ge_{1-x}P_xS_4$ (thio-LISICON) [21] are single-ion Li conductors that also offer high mechanical moduli. Permeability of these materials is also low, which prevents parasitic side reactions with conversion cathodes (e.g. S_8,

O_2, CO_2) or their reduction products with Li, a requirement for the most energetic LMBs. A generic shortcoming is that solid electrolytes such as LiPON ($\sigma_{25°C}$ = 2.3 × 10^{-6} S/cm) that provide attractive chemical stability possess too low ionic conductivity. Bates et al. have nonetheless shown that the poor conductivity of LiPON can be overcome by deploying the electrolyte as RF coated films (1 – 2μm thick) in micro-LMBs, [22] but maintaining good adhesion with the current collector during cell recharge still remains an unresolved challenge. Newer solid-state electrolytes, such as thio-LISICON ($\sigma_{25°C}$ = 2.3 × 10^{-3} S/cm; with x = 0.75), are not limited by σ, but present other challenges related to chemical stability and cost. Significant opportunities therefore exist for research on synthesis of cost-effective and mechanically strong single-ion electrolytes with LiPON-like stability and thio-LISICON-like conductivities that are manufacturable. Older work by De Jonghe et al. [23] also provides other grounds for caution. These authors observed that Na dendrites form and proliferate even in cells employing liquid Na anodes and solid $NaBAl_2O_3$ ceramic electrolytes by growing into and expanding cracks in $NaBAl_2O_3$. This means that even when acceptable solid electrolytes are found, rigorous manufacturing, assembly, and crack inspection regimens are required to avoid batch-to-batch variations in performance and lifetime.

Single- or near-single ion conductors based on polymers, including Nafion, have received significant attention as alternatives to ceramics. [24, 25] Recent work by Lu et al. [24] show that the lifetime of a LMB employing lithiated Nafion soaked in a liquid electrolyte solvent is a strong increasing function of t_{Li}, with up to 40-fold increases in cell lifetime observed relative to the pure liquid electrolyte. A limitation of such

electrolytes is that the solvent compromises other attractive traits of solid electrolytes, such as low permeability and high modulus. Work by Song et al.[25] take these ideas a step further both in terms of simplicity and potential efficacy. Coatings of Nafion directly applied to Li anodes were shown to protect the anode and extend its operating lifetime. All theories that predict stable Li deposition by modification of transport in single-ion conductors only require the material to be present in a region near the anode that is of thickness about ten times the Debye screening length, meaning that a thin, solid Nafion or ceramic coating on Li might be used in conjunction with a liquid electrolyte solvent for stable deposition. Single-ion conductors based on other materials chemistries, including tri-block copolymers [26], nanoparticle salts [27], tetraarylborate networks [28], and holographic membranes with high transport anisotropy [29] have recently become available, which increases the number of electrolyte options. A recent promising approach is the use of nanostructured lithium metal anodes, thus reducing the local current density and yielding significantly attenuated dendrite growth. [30]

1.2.2 Improving mechanics

Ceramics, polymers and polymer-ceramic hybrids have been studied extensively as platforms for suppressing dendrite growth in LMBs. Solid electrolytes based on LiPON [20], LISICON [21], $Li_{10}SnP_2S_{12}$ [31], and Li_3N [32], among others offer room-temperature mechanical moduli well above that of metallic lithium, but suffer from the aforementioned challenges related to their room temperature conductivity, cost, and propensity to crack during cell assembly. Recently, Tu et al.[33] proposed a

novel electrolyte design in which a liquid electrolyte is hosted in the pores of a ceramic membrane with a high areal density of nanometer-sized pores, well below typical Li dendrite sizes. The authors showed that this design enables electrolytes with solid-like mechanical moduli and liquid-like ion mobilities. When used in LMBs, these materials combine the dendrite suppression characteristics of solids with fast transport of liquids, which facilitate battery operation at practical current densities.

Nanostructured electrolytes based on Li-ion conducting block co-polymers [17, 34, 35], cross-linked polymers [36, 37], and polymer nanocomposites [38, 39] utilize a similar hard-soft design to overcome conventional trade-offs between modulus and conductivity. These materials all show promise for stabilizing Li even when the electrolyte modulus is well below that of Li metal. For example, Li/Li symmetric cells based on cross-linked PE/PEO gel electrolytes have moduli in the range 100kPa – 1MPa, but are reported to increase LMB lifetime by over an order of magnitude, relative to high-molecular-weight PEO of similar modulus.[36] Likewise, LMBs based on crosslinked polyhedral oligomeric silsesquioxane or hairy nanoparticles [37] exhibit long-term (>2500 hrs) stability, even though their moduli rarely exceed 20 MPa. In a very recent demonstration of this concept, aramid nanofiber-PEO composites with a shear modulus measuring 1.8 GPa [39] formed by layer-by-layer assembly were shown to block growth of 130 GPa copper dendrites. Taken together, these results conclusively show that the criterion $G > 1.8G_{Li}(T)$ is not a requirement for stable LMB operation.

1.2.3 Creating artificial SEI

With few exceptions, liquid electrolytes used in lithium ion batteries form

fragile and unstable SEI layers on lithium metal. Carbonate based electrolytes for example all form unstable, thick and heterogeneous passivation layers on Li comprised predominantly of Li_2CO_3 salts and polymerized electrolyte molecular fragments. The Coulombic efficiency (CE) of a Li/copper or Li/stainless steel asymmetric cells provides a convenient way to quantify the ability of electrolytes to form stable SEI layers on Li. Carbonate electrolytes rarely exhibit CEs above 80% [40] while electrolytes such as 1,3-dioxalane (DOL) undergoes ring opening polymerization to form an elastic SEI that is more stable and which produces a high CE > 99% [41]. Similarly, glyme-based electrolytes like dimethoxyethane (monoglyme), diglyme, tetraglyme spontaneously form a tough, alkoxy SEI (ROLi), which stabilizes electrodeposition of Li and Na [42, 43]. A large body of work shows that a more reliable strategy for forming stable SEI on reactive metals is to employ additives, including $LiNO_3$ [44], vinylene carbonate [45] and sultones [46]. An open area where intrusive experimentation is needed concerns the SEI formation processes enabled by these additives and methods for characterizing the physical properties and mechanics of the SEI films produced. Many electrolyte salts used in lithium batteries contain fluorine; their breakdown in the presence of Li is also known to generate LiF among other fluorinated organics. Work by Lu et al. [47] shows that directly mixing poorly soluble LiF into liquid electrolytes produces a SEI enriched in the salt, which not only protects Li, but dramatically reduces dendrite formation in carbonate electrolytes [48]. It is possible that similar processes are at work in the remarkable ability of $CsPF_6$ [40], fluoro-ethylene carbonate [49], and dual LiTFSI and LiFSI salts to stabilize Li anodes [41], because experiments and theory show the materials are broken down by Li to produce

SEI rich in LiF. As already discussed, DFT analysis shows that coatings of lithium halide salts on a Li anode provides a mechanism for enhancing Li transport at the interface, reducing its tendency to form dendrites. The results from Lu et al. are in qualitative agreement with these expectations and underscore the potentially powerful role DFT and other computational tools can play in design and selection of additives.

In an important departure from in-situ SEI formation approaches, Cui and co-workers [50] recently reported that a coating of carbon nanospheres applied directly to Li provides a stable protective layer on the metal, with high CE (>99%) values reported. Work by Kozen [51] showing that thin alumina coatings on Li produced by atomic layer deposition impart both chemical and electrochemical stability take these ideas a step further, both in terms of efficacy and the possibility of creating Li anodes that can be safely handled outside the glove box and which are compatible with battery manufacturing in a standard dry-room environment.

The experimental studies are often informed by theoretical works studying the process at its various stages. The wide range of physical and chemical features of the problem, as well as complexity of the geometry involved, present a rich environment for theory and simulation studies in which to operate.

1.3 Theoretical and simulation studies

The theoretical and simulation studies take advantage of the various stages of morphology development to build relevant models for electrodeposition while incorporating a broad range of physicochemical phenomena.

1.3.1 Linear stability analysis

Linear stability analysis of a flat surface provides insight into the stability of deposition at various length scales at early times, and the relevant physical phenomena at those scales. Typically, such models examine the role of charge transport on the initial growth of small perturbations of various shapes, such as hemispheres, cylinders or sinusoids, to the metal surface. Of these, the studies based on Mullins-Sekerka type stability analysis [7, 14, 15] select the sinusoidal shape on account of its generalizability to several geometries, and examine its growth under surface tension mediated electrodeposition. The goal, here, is to examine the relative competition of factors that govern dendrite growth, rather than predicting the long-time morphology of the deposits. Dilute solution theory is typically used to model transport in conventional salt electrolytes in liquid media with surface tension as a factor stabilizing the electrodeposition. The simplicity of the approach brings in the versatility to include a wide range of physical phenomena. The downside, however, is that these studies are blind to development of large structures, and may not be useful in predicting the long-time deposit structures, which is not preferred when specific deposit shapes are desired.

Theoretical studies in electrodeposition have widely used such models and have shown that the size of the deposits is limited by the surface energy of the metal-electrolyte interface. In an attempt to include a broader scale of physical phenomena, these models also are the focus of present work.

1.3.2 Phase field simulations

Phase field models are meso-scale simulations that describe the evolution of micro-scale deposits into larger structures. These methods have been used for a wide range of problems aside from electrodeposition, such as fracture propagation, evolution of thin films, alloy solidification, etc [52]. Following the approach of Cahn and Hilliard [53], compositional and structural state of the system is defined using a set a field variables, which obey well-known time-dependent continuum-scale conservation equations. These variables are assumed to be continuous across the interface, and thus, have, a diffuse interface description. The growth of the interface is explicitly tracked and feeds into the governing equations of the field variables, thus providing a complete description of the structural evolution [52]. The biggest advantage here is the ability to model the growth of small-scale deposits into large structures, thus bridging the gap between length scales. The drawback here, however, is that current formulations are only limited to small range of transport mechanisms due to their computationally intensive nature. Interfacial effects are also difficult to include in this development.

Few studies have employed phase field simulations to study electrodeposition. Cogswell [54] showed that slowing reaction kinetics improves the stability of deposition with good agreement with experiments on tip velocities. Chen et al [55] obtained a phase diagram for the morphologies of the deposits ranging from fiber-like pattern at low voltages to a fully dendritic structure to tip splitting dendritic deposits at high voltages. In another study, Liang and Chen [56] found that faster ion diffusion led to denser deposits that grow slowly, while faster reaction kinetics at the interface give fast-

growing long deposits in agreement with Cogswell's result.

1.3.3 Diffusion-limited aggregation

Diffusion-limited aggregation (DLA) provides a structural description of the deposition process, well above the smallest length scales of the deposits. DLA models were first reported by Witten and Sander [57] for the formation of aggregates of colloidal particles and have since been used for a wide range of applications including electrodeposition and electric-field induced dielectric breakdown. Random walkers are introduced at the boundary of a discretized simulation cell and allowed to take random steps toward the cluster in the center. A walker that moves out of the simulation cell is removed. A walker that ends up at a point next to an existing cluster is incorporated into the cluster, which thus grows. This development typically leads to fractal-like structures which are then analyzed in terms of their fractal dimension or Hausdorff number. This method is useful in exploring complex deposit structures. The biggest shortcoming is that these models are currently limited only to diffusive processes and including additional mechanisms, though theoretically possible through a Brownian dynamics-like framework, may be computationally expensive.

Chen and Jorne [58] have shown through DLA simulations that more compact deposits can be obtained if the relative resistivity of the electrode and electrolyte is higher. Vicsek [59] bridged the gap between linear stability and DLA by incorporating the effect of surface tension by including a curvature-dependent sticking probability for a random walker near the growing cluster. He observed that as the surface tension increases, the deposits grow less randomly and with a higher characteristic

wavelength. A similar effect was observed by Halsey and Leibig [60] who observed a transition from dendritic to compact deposits for a solution conductivity dependent length scale.

1.3.4 Electroconvection

Some recent works have attempted to address the topic of electroconvection during electrodeposition. Electroconvection refers to the fluid flow induced by the electric field driving the deposition itself, which enhances the instability of deposition. The general nature of the highly coupled problem – the transport-driven deposit growth, with the modification to the electric field by the growing deposit, and the effect of the electric field on the convection, which in turn affects the deposit growth – makes this problem extremely difficult to simulate. A study by Tan and Ryan [61] attempts to solve this by using a mesh-free technique called Smoothed Particle Hydrodynamics, to show that reducing the electrolyte viscosity modifies the electroconvection enough to render less dendritic deposition. Druzgalski et al [62] solved the simpler problem of electroconvection at an ion-selective surface without the growing electrode front and obtained that at high electric fields, the nonlinear nature of the problem can give rise to chaotic, turbulence-like flow patterns.

1.4 Summary and scope

The vast wealth of literature reported above can be summarized into three fundamental ideas:

1. Dendrite growth is a morphological instability on the metal surface driven by unstable ion transport
2. An elastic solid separator can suppress the growth of the instability
3. Interfacial properties of the metal have significant influence on the growth of the instability
4. Electroconvection in the electrolyte can enhance the instability of deposition and dendritic growth

We can then use these ideas to look for theoretical approaches to stabilize the deposition. This is addressed sequentially in the subsequent chapters. In Chapter 2, we introduce a novel electrolyte design for reducing the instability in transport to the surface. This idea, loosely termed "tethered anion electrolyte", is based on the analysis of Chazalviel [12], who showed that migration of anions from the metal surface induces large electric fields. We perform an analysis of transport across the tethered anion electrolyte and evaluate stability of deposition across it using linear stability analysis. In Chapter 3, we study the effect of elasticity of the tethered anion electrolyte as a means to study the combined effects of modification of transport and elasticity-induced suppression of unstable deposition. In Chapter 4, we address the relatively unaddressed problem of transport in and elasticity of the interfacial layer and introduce a framework to include interfacial effects in linear stability models. Finally, in Chapter 5, we look at the possible use of polyelectrolyte additives as a means to modify electroconvection in deposition.

REFERENCES

1. Tarascon, J.-M., and Armand, M., Issues and challenges facing rechargeable lithium batteries, *Nature*, **414**, 359-367 (2001).

2. Xu, K., Nonaquoeus liquid electrolytes for lithium-based rechargeable batteries, *Chem. Rev.*, **104**, 4303-4418 (2004).

3. Shu, Z. X., McMillan, R. S., and Murray, J. J., Electrochemical intercalation of lithium into graphite, *J. Electrochem. Soc.*, **140 (4)**, 922-927 (1993).

4. Manthiram, A., Fu, Y., and Su, Y.-S., Challenges and prospects of lithium-sulfur batteries, *Acc. Chem. Res.*, **46**, 1125-1134 (2013).

5. Girishkumar, G., McCloskey, B., Luntz, A. C., Swanson, S., and Wilcke, W., Lithium-air battery: promise and challenges, *J. Phys. Chem. Lett.*, **1**, 2193-2203 (2010).

6. Bazant, M.Z., Regulation of ramified electrochemical growth by a diffusive wave. *Phys. Rev. E* **52 (2)**, 1903-1914 (1995).

7. R. Aogaki, K. Kitazawa, Y. Kose, K. Fueki, Theory of powdered crystal formation in electrocrystallization – occurrence of morphological instability at the electrode surface. *Electrochim. Acta* **25 (7)**, 965-972 (1980).

8. Stark, J. K., Ding, Y., and Kohl, P. A., Dendrite-free electrodeposition and reoxidation of lithium-sodium alloy for metal-anode battery, *J. Electrochem. Soc.*, **158 (10)**, A1100-A1105 (2011).

9. Fleury, V., Chazalviel, J.-N. & Rosso, M. Coupling of drift, diffusion, and electroconvection, in the vicinity of growing electrodeposits. *Phys. Rev. E* **48**, 1279-1295 (1993)

10. Aurbach, D., Zinigrad, E., Cohen, Y. & Teller, H. A short review of failure mechanisms of lithium metal and lithiated graphite anodes in liquid electrolyte solutions. *Solid State Ionics* **148**, 405–416 (2002)

11. Sawada, Y., Dougherty, A., Gollub, J. P. Dendritic and fractal patterns in electrolytic metal deposits. *Phys. Rev. Lett.*, **56**, 1260 (1986)

12. Chazalviel, J-N. Electrochemical aspects of the generation of ramified metallic electrodeposits, *Phys. Rev. A* **42**, 7355-7367 (1990)

13. Lu, Y., Korf, K. S., Kambe, Y., Tu, Z. & Archer, L. A. Ionic-liquid–nanoparticle hybrid electrolytes: applications in lithium metal batteries. *Angewandte Chemie. Intl Ed.*, **53**, 488-492 (2014)

14. Sundstrom, L. G. & Bark, F. H. On morphological instability during electrodeposition with a stagnant binary electrolyte. *Electrochim. Acta* **40**, 599-614 (1995)

15. Tikekar, M. D., Archer, L. A. & Koch, D. L. Stability analysis of electrodeposition across a structured electrolyte with immobilized anions. *J. Electrochem. Soc.* **161**, A847-A855 (2014)

16. Monroe, C. & Newman, J. The impact of elastic deformation on deposition kinetics at lithium/polymer interfaces, *J. Electrochem. Soc.* **152**, A396-A404 (2005)

17. Stone, G. M., et al. Resolution of the modulus versus adhesion dilemma in solid polymer electrolytes for lithium metal batteries, *J. Electrochem. Soc.* **159**, A222-A227 (2012)

18. Ozhabes, Y., Gunceler, D., Arias, T. A. Stability and surface diffusion at lithium-electrolyte interphases with connections to dendrite suppression. Preprint at http://arxiv.org/abs/1504.05799 (2015)

19. Jäckle, M. & Groß, A. Microscopic properties of lithium, sodium and magnesium battery anode materials related to possible dendrite growth. *J. Chem. Phys.* **141**, 174710 (2014)

20. Yu, X., Bates, J. B. & Jellison, G. E. A stable thin-film lithium electrolyte: lithium phosphorus oxynitride. *J. Electrochem Soc.* **144**, 524-531 (1997)

21. Kanno, R. & Murayama, M. Ionic conductor Thio-LiSICON: The Li2S-GeS2-P2S5 system. *J. Electrochem Soc.* **148**, 742-746 (2001)

22. Bates, J. B., et al. Fabrication and characterization of amorphous lithium electrolyte thin films and rechargeable thin-film batteries. *J. Power Sources* **43**, 103-110 (1993)

23. De Jonghe, L. C., Feldman, L., & Millett, P. Some geometrical aspects of breakdown of sodium beta alumina. *Mater. Res. Bull.* **14,** 589-595 (1979)

24. Lu, Y., et al. Stable cycling of lithium metal batteries using high transference number electrolytes, *Adv. Energy Mater*. **5**, 1402073 (2015)

25. Song, J., Lee, H., Choo, M.-J., Park, J-K. & Kim, H-T. Ionomer-liquid electrolyte hybrid ionic conductor for high cycling stability of lithium metal electrodes. *Sci. Rep.* **5**, 14458 (2015)

26. Bouchet, R., et al. Single-ion BAB triblock copolymers as highly efficient electrolytes for lithium-metal batteries. *Nat. Mater.* **12**, 452-457 (2013)

27. Schaefer, J. L., Yanga, D. A. & Archer, L. A. High lithium transference number electrolytes via creation of 3-dimensional, charged, nanoporous networks from dense functionalized nanoparticle composites. *Chem. Mater.* **25**, 834-839 (2013)

28. Van Humbeck, J. F., et al. Tetraarylborate polymer networks as single-ion conducting solid electrolytes. *Chem. Sci.* **6**, 5499-5505 (2015)

29. Smith, D.M., Cheng, S., Wang, W., Bunning, T. J. & Li, C. Y. Polymer electrolyte membranes with exceptional conductivity anisotropy via holographic polymerization. *J. Power Sources* **271**, 597-603 (2014)

30. Chen, Q., Geng, K. & Sieradzki, K. Prospects for dendrite-free cycling of Li metal batteries. *J. Electrochem. Soc.*, **162 (10)**, A2004-A2007 (2015)

31. Bron, P., et al. Li10SnP2S12: An affordable lithium superionic conductor. *J. Am. Chem. Soc.* **135**, 15694-15697 (2013)

32. Lapp, R., Skaarup, S., & Hooper, A. Ionic conductivity of pure and doped Li3N. *Solid State Ionics* **11**, 97-103 (1983)

33. Tu, Z., Kambe, Y., Lu, Y. & Archer, L. A. Nanoporous polymer-ceramic composite electrolytes for lithium metal batteries. *Adv. Energy Mater.* **4**, 1300654 (2014)

34. Giles, J. R. M., Gray, F. M., Maccallum, J. R. & Vincent, C. A. Synthesis and characterization of ABA block copolymer-based polymer electrolytes. *Polymer* **28**, 1977-1981 (1987)

35. Panday, A., et al. Effect of molecular weight and salt concentration on conductivity of block copolymer electrolytes. *Macromolecules* **42**, 4632–4637 (2009)

36. Khurana, R., Schaefer, J. L., Archer, L. A. & Coates, G. W. Suppression of lithium dendrite growth using cross-linked polyethylene/poly(ethylene oxide) electrolytes: a new approach for practical lithium-metal polymer batteries. *J. Am. Chem. Soc.* **136**, 7395-7402 (2014)

37. Pan, Q., Smith, D. M., Qi, H., Wang, S. & Li, C. Y. Hybrid electrolytes with controlled network structures for lithium metal batteries. *Adv. Mater.* **27**, 5995-6001 (2015)

38. Gurevitch, I., et al. Nanocomposites of titanium dioxide and polystyrene-poly(ethylene oxide) block copolymer as solid-state electrolytes for lithium metal batteries. *J. Electrochem. Soc.* **160(9)**, A1611-A1617 (2013)

39. Tung S.-O., Ho, S., Yang, M., Zhang, R. & Kotov, N. A. A dendrite-suppressing composite ion conductor from aramid nanofibres, *Nat. Commun.* **6**, 6152 (2015)

40. Ding, F., Xu, W., Graff, G. L., Zhang, J., Sushko, M. L., Chen, X., Shao, Y., Engelhard, M. H., Nie, Z., Xiao, J. & Liu, X. Dendrite-free lithium deposition via self-healing electrostatic shield mechanism. *J. Am. Chem. Soc.* **135**, 4450-4456 (2013)

41. Miao, R., et al. Novel dual-salts electrolyte solution for dendrite-free lithium-metal based rechargeable batteries with high cycle reversibility. *J. Power Sources* **271**, 291–297 (2014)

42. Qian, J. et. al. High rate and stable cycling of lithium metal anode. *Nat. Commun.* **6**, 6362 (2015)

43. Seh, Z. W., Sun, J., Sun, Y., Cui, Y. A highly reversible room-temperature sodium metal anode. *ACS Cent. Sci.* **1**, 449-455 (2015)

44. Barghamadi, M., et al. Lithium–sulfur batteries—the solution is in the electrolyte, but is the electrolyte a solution? *Energy Environ. Sci.* **7**, 3902–3920 (2014)

45. Aurbach, D., et al. On the use of vinylene carbonate (VC) as an additive to electrolyte solutions for Li-ion batteries. *Electrochim. Acta* **47**, 1423–1439 (2002)

46. Li, B., Xu, M., Li, T., Li, W., & Hu, S. Prop-1-ene-1,3-sultone as SEI formation additive in propylene carbonate-based electrolyte for lithium ion batteries. *Electrochem. Commun.* **17**, 92–95 (2012)

47. Lu, Y., Tu, Z. & Archer, L. A. Stable lithium electrodeposition in liquid and nanoporous solid electrolytes. *Nat. Mater.* **13**, 961-969 (2014)

48. Choudhury, S. & Archer, L. A. Lithium fluoride additives for stable cycling of lithium batteries at high current densities. *Adv. Electron. Mater.* **2**, 1500246 (2016)

49. Etacheri, V., et al. Effect of fluoroethylene carbonate (FEC) on the performance and surface chemistry of Si-nanowire Li-ion battery anodes. *Langmuir* **28**, 965–976 (2012)

50. Zheng, G., et al. Interconnected hollow carbon nanospheres for stable lithium metal anodes. *Nat. Nanotech.* **9**, 618-623 (2014)

51. Kozen, A. C., et al. Next-generation lithium metal anode engineering via atomic layer deposition. *ACS Nano* **9**, 5884–5892 (2015)

52. Chen, L. Q., Phase-field models for microstructure evolution, *Annu. Rev. Mater. Sci.* **32**, 113-140 (2002)

53. Cahn, J. W., and Hilliard, J. E., Free energy of a nonuniform system. I. Interfacial free energy, *J. Chem. Phys.* **28**, 258-267 (1958)

54. Cogswell, D. A., Quantitative phase-field modeling of dendritic electrodeposition, *Phys. Rev. E* **92**, 011301(R) (2015)

55. Liang, L., and Chen, L.-Q., Nonlinear phase field model for electrodeposition in electrochemical systems, *Appl. Phys. Lett.* **105**, 263903 (2014)

56. Chen, L., et al, Modulation of dendritic patterns during electrodeposition: a nonlinear phase-field model, *J. Power Sources* **300**, 376-385 (2015)

57. Witten Jr., T. A., and Sander, L. M., Diffusion-limited aggregation, a kinetic critical phenomenon, *Phys. Rev. Lett.* **47(17)**, 1400-1403 (1981)

58. Chen, C. P., and Jorne, J., Fractal analysis of zinc electrodeposition, *J. Electrochem. Soc.* **137(7)**, 2047-2051 (1990)

59. Vicsek, T., Pattern formation in diffusion-limited aggregation, *Phys. Rev. Lett.* **53(24)**, 2281-2284 (1984)

60. Halsey, T. C., and Leibig, M., Electrodeposition and diffusion-limited aggregation, *J. Chem. Phys.* **92**, 3756-3767 (1990)

61. Tan, J., and Ryan, E. M., Computational study of electro-convection effects on dendrite growth in batteries, *J. Power Sources* **323**, 67-77 (2016)

62. Druzgalski, C. L., Anderson, M. B., and Mani, A., Direct numerical simulation of electroconvective instability and hydrodynamic chaos near an ion-selective surface, *Phys. Fluid.* **25**, 110804 (2013)

CHAPTER 2

THE TETHERED ANION ELECTROLYTE

We can, thus, state that metal dendrite formation is promoted by the concentration of mass flux on the dendrite tips and surface flaws, while the action of surface tension and the mechanical compression of the electrolyte/separator hinder growth and propagation. Once growth starts, it also appears that neither the surface tension nor the electrolyte/separator modulus is ever large enough to completely stop the dendrite from propagating through the inter-electrode space. It therefore seems important to pursue new theoretical approaches with the aim of discovering workable schemes for modifying the inter-electrode mass transfer to stop dendrites at the formation stage. Inspired by the analysis of Chazalviel [1], we herein propose a structured electrolyte (Fig 2.1a) to modify the inter-electrode mass transport to stabilize the metal surface against dendrite formation. We use continuum analysis to evaluate the effect of the structure of this electrolyte on the initial growth rate of surface perturbations. We are particularly interested in a structured electrolyte that can be employed to create an inter-electrode region wherein a fraction of anions are fixed in place. Two possible constructions for this electrolyte are illustrated in Figs 1b and 1c. In the first design (Fig 2.1b), the electrolyte consists of a porous solid matrix with the fluid containing the electrolyte filling the pores. The solid matrix dissociates ions into the fluid to form a static charge on its surface, which constitutes the fixed charge. In the second construction (Fig 2.1c), based on the work of Schaefer et al [2] and Lu et al [3, 4], nanoparticles with tethered anions or ionic liquid ligands are dispersed in a sea

of fluid with/without a mobile supporting electrolyte. In the case of the electrolytes reported by Schaefer et al [2], the anions are covalently tethered to much larger nanoparticles and dissociation in the fluid medium leaving the anion permanently tethered to the nanoparticle, while the cation enters the fluid medium and becomes mobile. For the electrolytes reported by Lu et al [3, 4], the anion is fixed to the particle via a dissociable bond with cationic 1-methy-3-propylimidazolium or 1-methy-3-propylpiperidinium species covalently anchored to the nanoparticles. In either case, the large size and concentration of particles in the electrolyte medium prevents particle migration over a large distance, even under the action of the applied electric field.

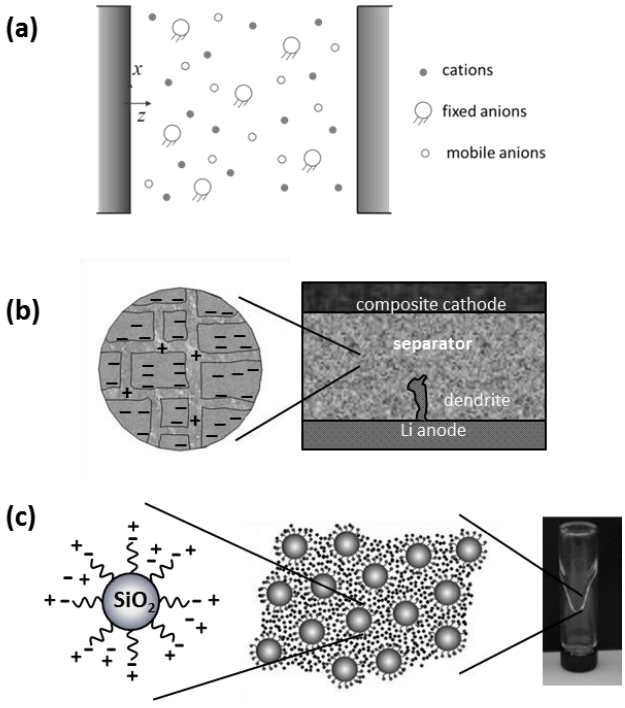

Figure 2.1: The proposed fixed anion electrolyte to stabilize the electrodeposition (a) An illustration of the electrolyte. The large blue circles represent the fixed anions and comprise a fraction C_a^f of the total number of anions (b) A porous matrix implementation of the fixed anion electrolyte (c) Nanoparticles with tethered anions used by Schaefer et al [2]

In addition to modeling the transport through the electrolyte, we perform a stability analysis of the electrode surface to study surface tension mediated electrodeposition on a metallic electrode. We first solve the transport problem for a perfectly smooth electrode analytically to show that the structured electrolyte is effective in reducing the electric field at the electrode. Based on this solution, we solve for electrodeposition on a sinusoidally perturbed electrode to determine the growth of the perturbation at various current densities and proportions of fixed anions in the electrolyte.

2.1 Model for the tethered anion electrolyte

We consider a simple model (Fig 2.1a) for a *structured electrolyte* in which a fraction C_a^f of the anions are immobilized and uniformly distributed in the inter-electrode space. The concentration of mobile anions is denoted by C_a^m and the total concentration of anions present in the system at equilibrium C_0. For simplicity, we assume quasi-steady electrodeposition, i.e. the growth of the metal electrode surface does not affect the transport. (See Appendix for justification.) We also assume that the mobile anion is neither generated nor consumed over the cell operation. The total anion concentration at any point is therefore, the sum of the fixed and mobile anions. The limit of C_a^f tending to zero approximates a conventional salt electrolyte since all the anions are in principle mobile. In the other extreme, i.e. C_a^f of unity, a so-called single ion conductor is retrieved. Lithium ion is considered to be the sole cationic

species in the electrolyte and the cationic concentration is designated as C_c. We also assume that the Li^+ exists only as a cationic species and does not form a coordination complex.

At steady-state, the structured electrolyte is subjected to a transport overpotential V_0. Considering the diffusive-migrative transport of the cation and the mobile anion, one gets:

$$\frac{\mathbf{J}}{F} = -D_c \nabla C_c - \mu_c C_c \nabla \phi \tag{2.1}$$

$$0 = -D_a \nabla C_a^m + \mu_a C_a^m \nabla \phi \tag{2.2}$$

where D_c, D_a, μ_c, μ_a are the diffusivities and mobilities of the cation and mobile anion respectively, $\mathbf{J} = J\hat{\boldsymbol{z}}$ is the current density passing through the cell, F is Faraday's constant and ϕ is the electrostatic potential. Diffusivities and mobilities of the ions are related by the Stokes-Einstein relation, viz. $D_c = RT\mu_c/F$ and $D_a = RT\mu_a/F$. We also assume local electroneutrality, i.e. $C_c = C_0 C_a^f + C_a^m$.

The boundary conditions are given by the electrochemical equilibrium at the two electrodes. The electrochemical potential of the lithium ion at the lithium electrode interface, located at $z = L$ is given by

$$\psi_c\big|_L = \psi_c^{\ominus} + RT \ln C_c\big|_L + F\,\phi\big|_L \tag{2.3}$$

The electrochemical potential of lithium in the lithium electrode is given by

$$\psi_m\big|_L = \psi_m^{\ominus} + \gamma v_m \mathrm{K} + F\phi_m \tag{2.4}$$

The superscript $\ominus$ denotes standard chemical potentials of the respective species. γ is the surface tension of the electrode-electrolyte interface, v_m is the partial molar volume

of lithium metal, K is the electrode curvature. ϕ_m is the electrostatic potential of the lithium electrode. The surface tension term is similar to that used in previous studies [5, 6]. Electrochemical equilibrium of the electrode-electrolyte interface dictates

$$\psi_m^{\Theta} + \gamma\nu_m \mathrm{K} + F\phi_m = \psi_c^{\Theta} + RT\ln C_c\big|_L + F\phi\big|_L \tag{2.5}$$

A similar equilibrium is used at the counter electrode at $z = 0$, without the surface tension term because the counter electrode does not deform.

The reference for electrostatic potential is taken to be a point in the electrolyte next to the lithium electrode. This gives

$$\phi\big|_L = 0 \tag{2.6}$$

$$\phi\big|_0 = V_0 \tag{2.7}$$

We assume the electrodes are planar in the base state and separated in the z direction. For (2.5), this gives $\phi_m = {}^{1}\!/_{F}\,(\psi_c^0 - \psi_m^0) + {}^{RT}\!/_{F}\ln C_c|_L$. The mobile anion concentration, cation concentration and spatially varying potential, can be readily found as implicit functions of the spatial coordinate z and the current density J from Eq. (2.1), (2.2), (2,7) and the electroneutrality assumption.

$$C_a^m = C_{a0}^m C_0 \exp\left[-\frac{F\left(V_0-\phi\right)}{RT}\right] \tag{2.8}$$

$$2C_c - 2C_0\left(C_a^f + C_{a0}^m\right) + C_a^f C_0 \ln\left(\frac{C_c - C_a^f C_0}{C_{a0}^m C_0}\right) = -\frac{Jz}{FD_c} \tag{2.9}$$

$$C_a^f C_0 \frac{F\left(V_0-\phi\right)}{RT} + 2C_{a0}^m C_0\left[1-\exp\left(-\frac{F\left(V_0-\phi\right)}{RT}\right)\right] = \frac{Jz}{FD_c} \tag{2.10}$$

where J is the z-component of the current density. The relationship between current

density and applied overpotential is obtained from Eq. (2.6) and (2.10) as

$$J = \frac{D_c F C_0}{L}\left[C_a^f \frac{FV_0}{RT} + 2C_{a0}^m\left[1-\exp\left(-\frac{FV_0}{RT}\right)\right]\right] \tag{2.11}$$

The mobile anion concentration follows the equilibrium Boltzmann distribution, as expected, and the pre-exponent can be evaluated by anion conservation,

$$\int_0^L C_a^m dz = \int_{V_0}^0 C_{a0}^m C_0 \exp\left(\frac{F\phi}{RT}\right)\frac{1}{d\phi/dz}d\phi = C_0\left(1-C_a^f\right)L \tag{2.12}$$

Evaluating $d\phi/dz$ from Eq. (2.10) and substituting into Eq. (2.12) gives,

$$C_{a0}^m = \frac{-\mathrm{B}+\sqrt{\mathrm{B}^2-4\mathrm{A}\Gamma}}{2\mathrm{A}} \tag{2.13}$$

where $A = 1-\exp(-2FV_0/RT)$, $\Gamma = -FV_0/RT\left(C_a^f - {C_a^f}^2\right)$ and $\mathrm{B} = \left(3C_a^f - 2\right)[1-\exp(-FV_0/RT)]$.

The conductivity of the structured electrolyte at steady state can be defined as $\chi = JL/V_0$ and is readily obtained from Eq. (2.11). The variation of conductivity with C_a^f and V_0 is plotted in Fig 2.2. Note that the conductivity varies with the applied overpotential due to the diffusion limit. The plot shows that fixing anions clearly improves the conductivity at higher potentials. In the absence of fixed anions, a large overpotential tends to deplete the ions near the metal electrode. As a result, a large electric field is required to drive the current in this region. The fixed anions prevent this by ensuring the presence of ions near the metal electrode, and thus improve the conductivity at high overpotentials.

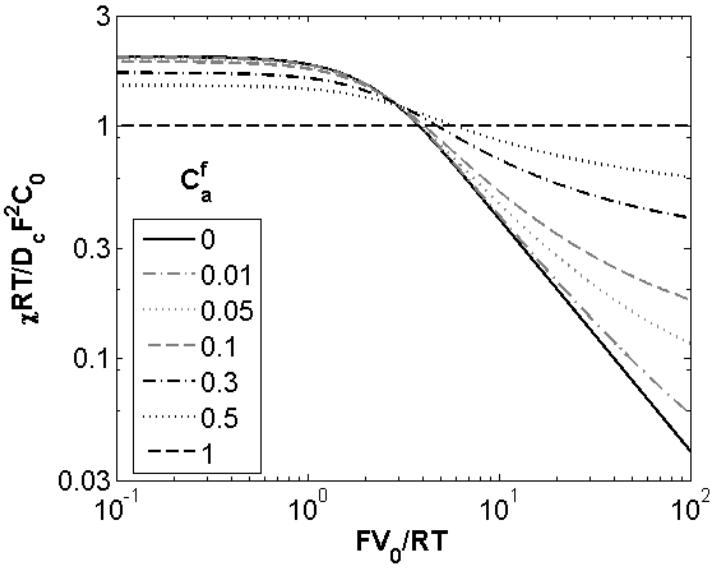

Figure 2.2: Conductivity of the fixed anion electrolyte as a function of overpotential and fraction of fixed anions

Figs 2.3a, 2.3b, 2.3c depict the dimensionless cation concentration, potential, and electric field $E = -d\phi/dz$ at various current densities for an intermediate value of C_a^f = 0.1. We clearly find two types of behavior depending on the current being passed through the cell. At low current densities, the transport is governed purely by ambipolar diffusion of the ions and the cation concentration varies approximately linearly with position in the inter-electrode space. In this regime, the electric field *E* is small and nearly uniform. Dendrite growth would be promoted by the convergence of diffusive flux lines, which have a shorter path to the dendrite tip.

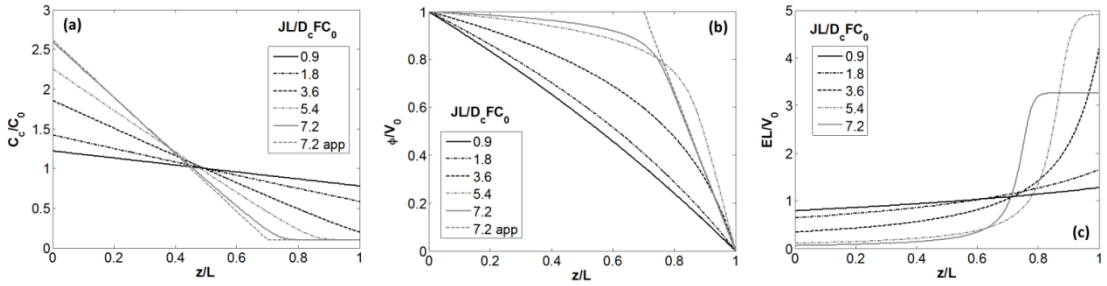

Figure 2.3: Base state solution to the transport problem at steady state (a) Cation concentration profiles, (b) Electrical potential profiles, and (c) Electric field profiles at various current densities for C_a^f = 0.1. The dashed black line corresponds to the critical current density while the dashed gray line corresponds to the two-region approximation for JL/D_cFC_0 = 7.2.

As the current is increased, a critical current density, $J_{cr} = 4D_cFC_0\left(1 - C_a^f\right)/L$, is reached above which all the mobile anions are depleted from the region near the metal electrode. Strong concentration gradients appear in the inter-electrode space and the lithium ion concentration at the metal electrode drops, reaching a finite, limiting value equal to the fixed anion concentration at a critical current density. The concentration at the counter electrode rises to maintain the initial cation concentration in the cell. On increasing the current density beyond this value, the mobile anions form a depletion region near the metal electrode and begin to accumulate against the counter electrode to accommodate the rising concentration of cations that build up at the counter electrode in response to the higher currents. In this high current density regime, the transport is controlled by electromigration in the region of constant cation concentration near the metal electrode and by ambipolar diffusion in the region near the counter electrode. The overpotential, V_{cr}, corresponding to J_{cr} is obtained using Eq. (2.11) and plotted in Fig 2.4. A small transition region seen between the two regions becomes smaller as the current density

increases further.

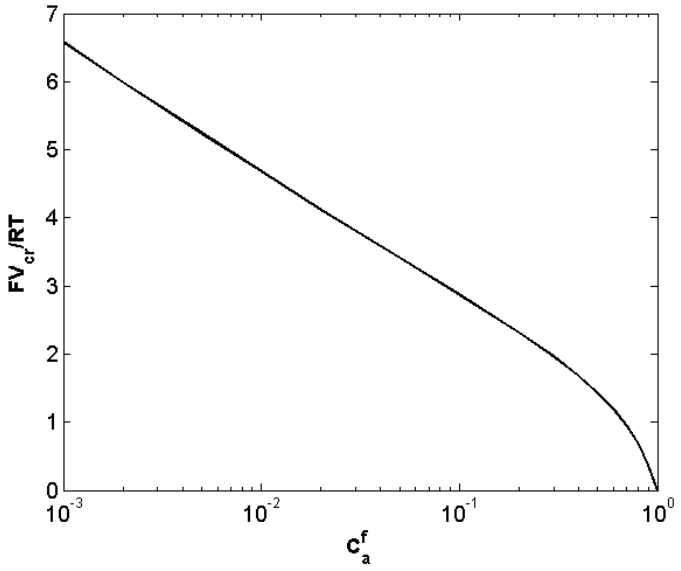

Figure 2.4: Critical overpotential as a function of fixed anion proportion

Depletion of mobile anions from the vicinity of the metal electrode produces large electric fields near it that extend further into the inter-electrode space as the current density rises above the critical value. It is evident that transport in the high-current density regime is governed essentially by the migration of lithium ions under the action of a nearly uniform electric field, as seen from the linear potential profile in Fig 2.3b. Dendrite growth, here, is expected to be due to the convergence of electric field lines on dendrite tips, as suggested by Chazalviel [1]. Fig 2.5 explicitly shows the variation of electric field at the metal electrode with the fraction of fixed anions. The structured electrolyte is seen to reduce the electric field dramatically upon inclusion of modest fractions of fixed anions. In comparison, the reduction in electric field is smaller at low current densities due to the small magnitude of applied electric field.

The transition can be seen to take place around the range of FV_0/RT from 2 to 5. At high current densities, with a smaller fraction of anions being mobile, the diffusion region shrinks and the migration region expands, leading to a larger region available for the potential drop, and hence giving a smaller electric field near the metal electrode. Additionally, the fixed anions put a lower limit on the ion concentration near the wall and thus reduce the electric field required to drive the current near the metal electrode. Whether this reduced electric field is sufficient to stabilize the metallic surface against the formation of dendrites will be determined in the next section.

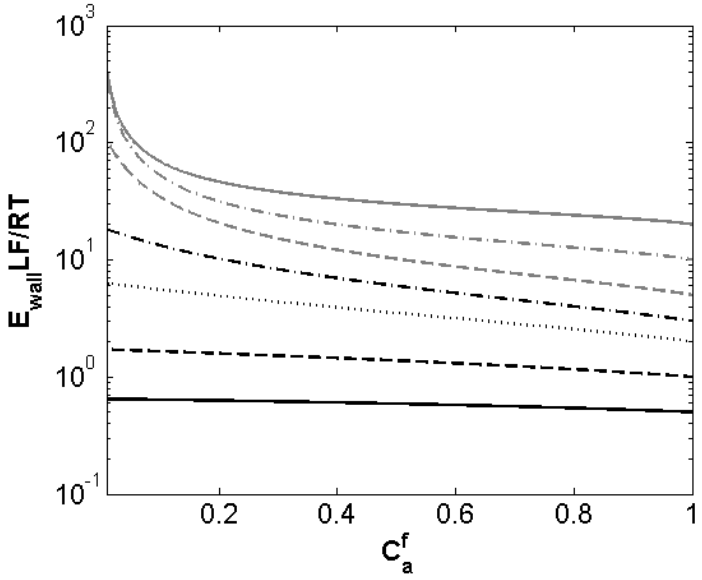

Figure 2.5: Electric field at the metal electrode as a function of fraction of fixed anions. The various curves are for different values of FV_0/RT going from bottom to top as, 0.5 (solid black), 1, 2, 3, 5, 10, 20 (solid gray).

This observation of two distinct regions with different free ion concentrations and a sharp boundary is similar to the desalination shocks seen by Mani and Bazant in

charged microchannels where the counterion is selectively consumed by an electrode. They find a sharp concentration drop that forms at the electrode and propagates away from the electrode leaving an ion depleted bulk fluid in its wake, with only the counterion present to neutralize the wall charge [7]. In the present case, we have this desalination shock propagating away from the metal electrode, while a diffusion wave caused by the generation of cations at the counter electrode moves toward the metal electrode. At steady state, the two waves meet at a point determined by the current passing through the system and form a static shock. Hence, while Mani and Bazant observe a discontinuity in ion concentration, we find a discontinuity in the concentration gradient. The large current regime is particularly pertinent to electrolytes with low ion diffusivities or low ion concentrations, where the magnitude of the critical current density is low.

We therefore, solve the problem independently for the two regimes – small currents ($J < J_{cr}$) and large currents ($J > J_{cr}$). In the intermediate zone ($J \sim J_{cr}$), the metal electrode lies in the transition region, which is harder to model analytically. We therefore extrapolate the solutions for small and large currents through this regime.

2.1.1 Large current densities

At large current densities ($J > J_{cr}$), we consider a simplification (Fig 2.6a), wherein the two regions have a sharp boundary and the smooth transition from the diffusion- to the migration-controlled region ignored. Ambipolar diffusion is taken to be the only mode of transport in the diffusion region thus accounting for the contribution of small electric field in that region seen in Fig 2.3c. The effect of electric

field on the cations neutralizing the fixed anions is ignored, both in the base and perturbed states. While this contribution may become significant at higher fixed anion proportions (C_a^f ~ 0.9-1), the reduced fraction of mobile anions in that case would make the diffusion region negligibly small. This means the concentration profile in the diffusion region is given by,

$$\nabla^2 C_c = 0 \tag{2.14}$$

and the current density is

$$\mathbf{J}^{\mathbf{diff}} = -2D_c F \nabla C_c \tag{2.15}$$

The factor of 2 appears from the application of Stokes-Einstein relation to ambipolar diffusion.

Likewise, diffusion within the migration region is ignored, and the perturbation to the fixed anion concentration is also ignored. The governing differential equations within this region, therefore, becomes

$$\nabla^2 \phi = 0 \tag{2.16}$$

with the current density taking the form

$$\mathbf{J}^{\mathbf{mig}} = -\mu_c F C_0 C_a^f \nabla \phi \tag{2.17}$$

This is illustrated in Fig 2.6a. The boundary between the two regions is obtained by implementing the requirement that the current density is the same between the two regions, i.e.

$$\mathbf{J}^{\mathbf{diff}} \cdot \mathbf{n}^{\mathbf{diff}}\Big|_l + \mathbf{J}^{\mathbf{mig}} \cdot \mathbf{n}^{\mathbf{mig}}\Big|_l = 0 \tag{2.18}$$

where $\mathbf{n}|_l$ is the normal to the boundary between the two regions taken

outwards from the respective region.

Cation concentration and electrostatic potential are also considered to be continuous across this boundary, i.e. $C_c|_l = C_0 C_a^f$ and $\phi|_l = V_0$.

Solving Eqs. (2.14) – (2.18), we obtain the solution for the simplified model as,

$$C_c = C_0 C_a^f + \frac{2C_0\left(1-C_a^f\right)}{l^2} L\left(l-z\right) \tag{2.19}$$

$$\phi = V_0 \frac{L-z}{L-l} \tag{2.20}$$

$$J = \frac{4D_c F C_0\left(1-C_a^f\right)L}{l^2} \tag{2.21}$$

where l is obtained from Eq. 18 as

$$l = L\frac{-\mathrm{B}_1 + \sqrt{\mathrm{B}_1^2 - 4\mathrm{A}_1\Gamma_1}}{2\mathrm{A}_1} \tag{2.22}$$

where $A_1 = C_a^f FV_0/RT$, $\Gamma_1 = -4\left(1 - C_a^f\right)$ and $\mathrm{B}_1 = 4\left(1 - C_a^f\right)$.

The base state concentration and potential profiles for this model are compared with the exact solution for one current density in Fig 2.3. The similarity of the profiles confirms the validity of the approximate model.

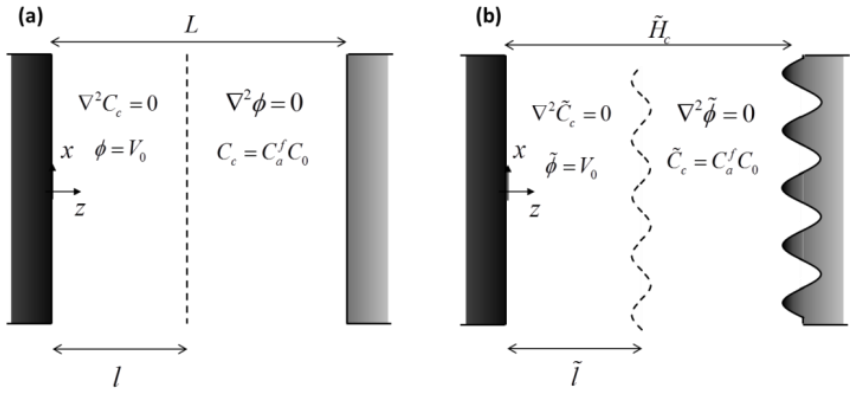

Figure 2.6: An illustration of the approximate model at high current densities (a) Base state and (b) The sinusoidally perturbed electrodes used in the stability analysis

2.1.2 Small current densities

For small current densities ($J < J_{cr}$), we have ambipolar diffusion as the only mode of transport in the interelectrode spacing. The governing equation, therefore, is simply the Laplace equation for concentration. The solution to the transport problem, in this case, is

$$C_c = C_0\left(C_a^f + C_{a0}^m\right) - \frac{Jz}{2FD_c} \tag{2.23}$$

$$C_0 C_{a0}^m \exp\left(-\frac{F\left(V_0 - \phi\right)}{RT}\right) = C_0 C_{a0}^m - \frac{Jz}{2D_c F} \tag{2.24}$$

with J and $C_{ao}{}^m$ given by Eqs. (2.11) and (2.13) respectively.

2.2 Linear stability analysis

We next perform a linear stability analysis to determine the stability of the electrode surface against the formation of dendrites. We impose a sinusoidal perturbation of a given wavenumber k (or wavelength $\lambda = 2\pi/k$) and arbitrary, but

small amplitude on the metal surface. The counter electrode surface is not perturbed because it is thought to rely upon intercalation or conversion chemistry, wherein dendrites do not form. The electric field lines converge on the crests of the wave, thus leading to higher deposition on the crests compared to the troughs. Diffusive flux is also higher on the crests compared to the troughs because of the shorter diffusion distance. In other words, transport is always likely to roughen the electrode surface. However, the deposition on the surface is altered by the surface tension of the electrolyte-electrode interface, which affects the electrochemical equilibrium of the deposition reaction and stabilizes the electrodeposition. The competing effects of the two driving forces – viz. the dendrite promoting convergence of transport lines, and the dendrite suppressing effect of surface tension determine the conditions for dendritic growth. As before, we assume quasi-steady electrodeposition.

Consider an electrode surface profile of the form: $\widetilde{H}_c = L + H_c' e^{\sigma t} e^{ikx}$ as seen in Fig 2.6b. The other parameters – concentration $\left[\tilde{C}_c = C_c + C_c'(z) e^{\sigma t} e^{ikx}\right]$, potential $\left[\tilde{\phi} = \phi + \phi'(z) e^{\sigma t} e^{ikx}\right]$ and current density $\left[\tilde{\mathbf{j}} = \mathbf{J} + \mathbf{J}'(z) e^{\sigma t} e^{ikx}\right]$ are also expected to vary in the same fashion. C_c, ϕ and $\mathbf{J}$ are the solutions of the transport problem for the flat electrode and have been derived in the previous section. These solutions are referred to as the base state solutions. The amplitude of the surface corrugation increases with time when the growth rate σ has a positive real part and decays indicating that the planar surface is stable when the real part of σ is negative. Note that the reference for potential continues to be the same as in the base state.

2.2.1 Large current densities

The base state described in Section 2.1.1 is perturbed in the fashion mentioned before. Concentration is perturbed within the diffusion region, while potential is perturbed in the migration region (Fig 2.6b). Electrostatic potential within the diffusion region and concentration within the migration region are assumed to be small in spite of the perturbation. The boundary zone between the two regions is also perturbed as $\tilde{l} = l + l' e^{\sigma t} e^{ikx}$. This leads to the following equations for concentration within the diffusion region and potential within the migration region.

$$\frac{d^2 C_c'}{dz^2} - k^2 C_c' = 0 \tag{2.25}$$

$$\frac{d^2 \phi'}{dz^2} - k^2 \phi' = 0 \tag{2.26}$$

These equations are solved with five boundary conditions viz., continuity of concentration, electrostatic potential and current density across the two-region interface, and chemical equilibrium at each of the two electrodes. Continuity of concentration, electrostatic potential and current density across the two-region interface can be mathematically expressed as

$$\tilde{C}_c\Big|_{\tilde{l}} = C_0 C_a^f \tag{2.27}$$

$$\tilde{\phi}\Big|_{\tilde{l}} = V_0 \tag{2.28}$$

$$\tilde{\mathbf{J}}^{\mathbf{diff}} \cdot \tilde{\mathbf{n}}^{\mathbf{diff}}\Big|_{\tilde{l}} + \tilde{\mathbf{J}}^{\mathbf{mig}} \cdot \tilde{\mathbf{n}}^{\mathbf{mig}}\Big|_{\tilde{l}} = 0 \tag{2.29}$$

To evaluate the concentration and potential at the perturbed two-region interface, we use Taylor expansion for the concentration around the base state

interface. In terms of the perturbed variables this transforms the above equations into

$$C_c'\Big|_l + \frac{dC_c}{dz}\Big|_l l' = 0 \tag{2.30}$$

$$\phi'\Big|_l + \frac{d\phi}{dz}\Big|_l l' = 0 \tag{2.31}$$

$$-2D_c F \frac{dC_c'}{dz}\Big|_l = -\mu_c C_a^f C_0 F \frac{d\phi'}{dz}\Big|_l \tag{2.32}$$

Chemical equilibrium at the diffusion region – counter electrode interface is the same as Eq. (2.5) without the surface tension term. The potential within the diffusion region and the surface profile of the counter electrode are not perturbed, as mentioned before. Incorporating this, we get

$$C_c'\Big|_0 = 0 \tag{2.33}$$

Chemical equilibrium at the migration region – metal electrode interface, given in Eq. (2.5), can be expressed in terms of the perturbed variables. The electrode curvature is given by $\mathrm{K} = d^2\tilde{H}_c/dx^2 = -H_c' k^2 e^{\sigma t} e^{ikx}$, assuming small curvatures. The fixed anion concentration is not perturbed.

$$-\gamma \nu_m H_c' k^2 = F\left[\phi'\Big|_L + \frac{d\phi}{dz}\Big|_L H_c'\right] \tag{2.34}$$

The growth rate of the metal surface is caused by the cation flux

$$\frac{\partial \tilde{H}_c}{\partial t} = \frac{\nu_m}{F}\tilde{\mathbf{J}}\cdot\tilde{\mathbf{n}}\Big|_{\tilde{H}_c} \tag{2.35}$$

where $\tilde{\mathbf{n}}|_{\tilde{H}_c}$ is the normal to the perturbed metal electrode surface taken into the

electrolyte. The growth rate of the perturbation is hence given by

$$H_c{}'\sigma = \nu_m \mu_c C_0 C_a^f \left.\frac{d\phi'}{dz}\right|_L \tag{2.36}$$

The values of ν_m and γ used here are 1.33 x 10^{-5} m^3/mol and 1.716 N/m respectively, which are similar to the ones used by Monroe and Newman [8].

Eq. (2.25), (2.26), (2.30) – (2.34) and (2.36) are solved to obtain

$$\sigma = \frac{\nu_m k}{F \tanh kL}\left[J - \gamma \nu_m \mu_c C_a^f C_0 k^2 \right] \tag{2.37}$$

The perturbation growth rate increases with the applied current density due to the increased rate of deposition. Therefore, we also normalize it with the current to produce a growth rate σ/J that expresses the growth in terms of the amount of deposition for fair comparison across various current densities:

$$\frac{\sigma}{J} = \frac{\nu_m k}{F \tanh kL}\left[1 - \frac{\gamma \nu_m \mu_c C_a^f C_0 k^2}{J} \right] \tag{2.38}$$

Plotting this result in Fig 2.7, we find that the system is stable at large wavenumbers and unstable at small wavenumbers. This is to be expected, as large wavenumbers imply higher curvatures, and hence a stronger effect of surface tension. The critical wavenumber at which the growth rate changes sign is given by

$$k_{cr} = \left(\frac{J}{\gamma \nu_m \mu_c C_a^f C_0} \right)^{1/2} \tag{2.39}$$

The growth rate has a maximum, which can be obtained by maximizing Eq. (2.38) with respect to the wavenumber. The wavenumber that this maximum corresponds to is called the most unstable mode. Using $d\sigma/dk = 0$, we have

$$k_{mu} \approx \frac{1}{\sqrt{3}} k_{cr} = \left(\frac{J}{3\gamma \nu_m C_0 \mu_c C_a^f} \right)^{1/2} \tag{2.40}$$

In obtaining Eq. (2.40), we dropped the tanh term in the expression for the growth rate, because its argument is always much greater than one for the most unstable mode. The growth rate of the most unstable mode is given by

$$\frac{\sigma_{mu}}{J} = \frac{2}{3} \frac{\nu_m k_{mu}}{F} \tag{2.41}$$

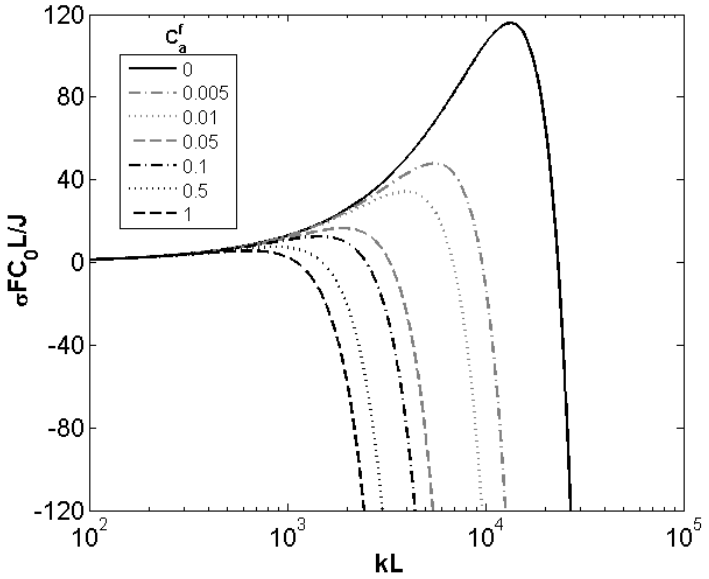

Figure 2.7: Growth rate of perturbations of varying wavenumbers at high current densities (FV_0/RT = 11; or V_0 = 275 mV). The solid black line is obtained by performing a stability analysis on the base state solution given by Chazalviel [1], while the dashed black line is the result for single-ion conductor

2.2.2 Small current densities

For small overpotentials, we consider ambipolar diffusion of the cation through the separator even after the deformation. The perturbation is illustrated in Fig 2.8. The

sole governing equation here is the diffusion equation for the cation. In terms of perturbation variables, this gives

$$\frac{d^2C_c'}{dz^2} - k^2C_c' = 0 \tag{2.42}$$

The boundary conditions are given by chemical equilibrium at the two interfaces, as before.

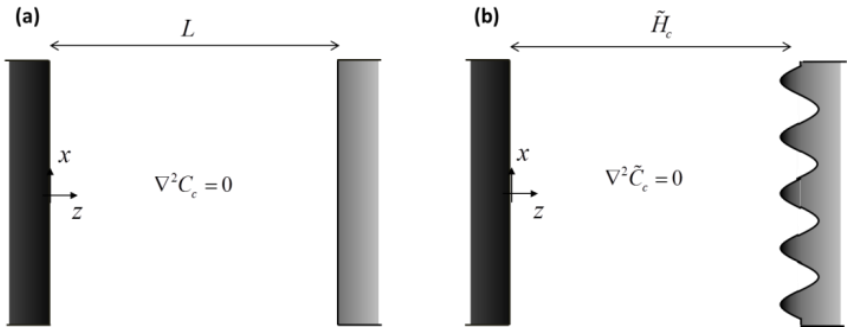

Figure 2.8: Base state and the sinusoidally perturbed electrodes used in the stability analysis at low current densities

Chemical equilibrium at the separator – counter electrode interface gives

$$RT\frac{C_c'\Big|_0}{C_c\Big|_0} + F\phi'\Big|_0 = 0 \tag{2.43}$$

Chemical equilibrium at the separator – metal electrode interface gives

$$-\gamma v_m H_c' k^2 = \frac{RT}{C_c\Big|_L}\left[C_c'\Big|_L + \frac{dC_c}{dz}\Big|_L H_c'\right] + F\left[\phi'\Big|_L + \frac{d\phi}{dz}\Big|_L H_c'\right] \tag{2.44}$$

The growth rate of the perturbation from Eq. (2.35) is,

$$H_c'\sigma = 2v_m D_c \frac{dC_c'}{dz}\Big|_L \tag{2.45}$$

Eq. (2.42) – (2.45) reveal that the current normalized growth rate is given by

$$\frac{\sigma}{J}=\frac{v_m k}{F\tanh kL}\left[1-\frac{2D_c F\gamma v_m k^2}{RTJ}\frac{C_c|_L\left(C_c|_L-C_0C_a^f\right)}{2C_c|_L-C_0C_a^f}\right] \tag{2.46}$$

where $C_c|_L = C_0C_a^f + C_{a0}^m$ is the concentration at the lithium electrode in the base state. The critical wavenumber and the most unstable wavenumber in this case, are given by

$$k_{cr}=\left[\frac{RTJ}{2D_c F\gamma v_m}\frac{2C_c|_L-C_0C_a^f}{C_c|_L\left(C_c|_L-C_0C_a^f\right)}\right]^{1/2} \tag{2.47}$$

$$k_{mu}\approx\frac{1}{\sqrt{3}}k_{cr}=\left[\frac{RTJ}{6D_c F\gamma v_m}\frac{2C_c|_L-C_0C_a^f}{C_c|_L\left(C_c|_L-C_0C_a^f\right)}\right]^{1/2} \tag{2.48}$$

Plotting the current density normalized perturbation growth rate (Fig 2.9), we see that surface tension stabilizes the surface for large wavenumbers, while the concentration of diffusive flux proves destabilizing at small wavenumbers. It is noteworthy that tethering anions does not create much of a difference to the electrode stability in this case. This is due to the fact that most of the current is carried by the mobile ions in this case, hence the tethered anions cause a small difference.

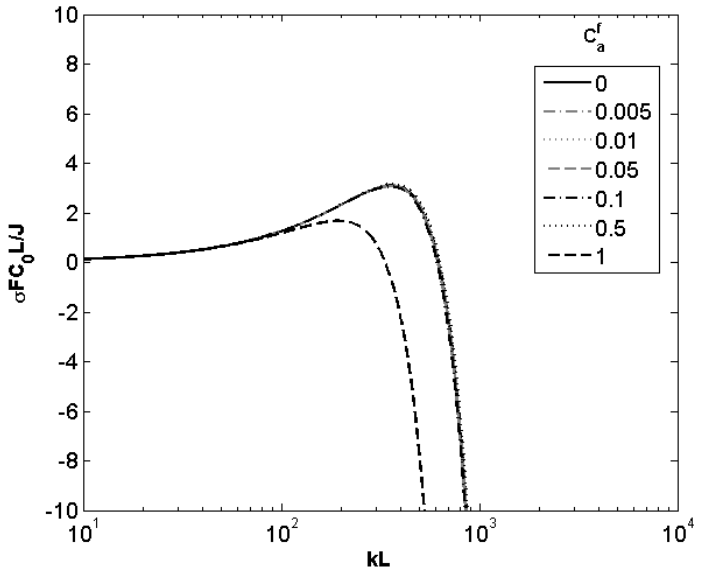

Figure 2.9: Growth rate of perturbations of varying wavenumbers at low current densities (FV_0/RT = 1; or V_0 = 25 mV). The result for single-ion conductor (black dashed line) is obtained from the large current densities analysis since transport in single-ion conductors is always driven by migration

The key results are summarized in Fig 2.10. In Fig 2.10a, we have the critical wavenumber, while Fig 2.10b shows the normalized growth rate corresponding to the most unstable wavelength against the applied overpotential. At low overpotentials, we find that tethering of anions makes little difference to the surface stability. Near the critical overpotential, however, the effect of tethering anions becomes apparent. As we further increase the applied overpotential, the stability parameters follow a different, but flatter variation. Tethering the anions has a strong influence on where this regime appears. In other words, both the critical wavenumber and the growth rate of the most unstable mode are reduced in the high overpotential (i.e. high current density) regime. The dashed line corresponding to single ion conductors is seen to be more stable than

conventional electrolytes at all potentials.

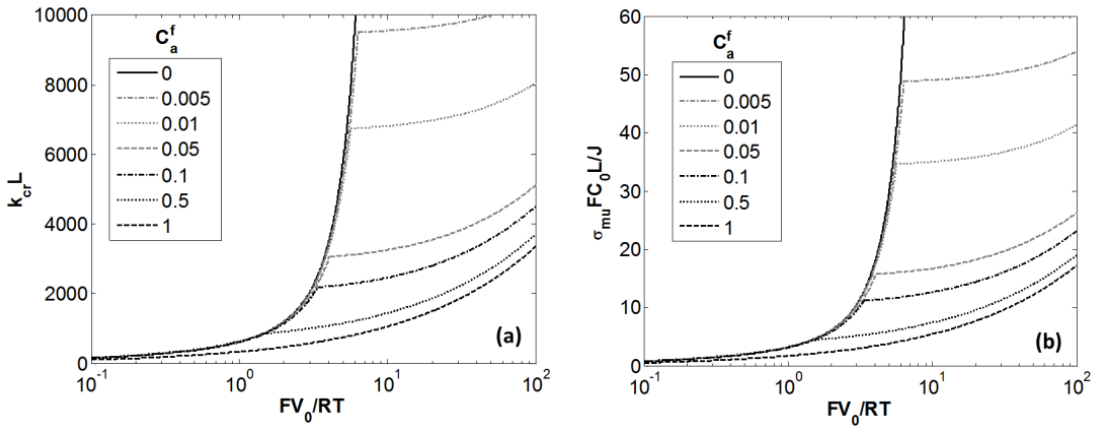

Figure 2.10: Two important parameters of the stability analysis. (a) Critical wavenumber and (b) Growth rate of most unstable mode at varying overpotentials for various fixed anion fractions.

2.3 Conclusion

We have thus shown that the tethered anion electrolyte improves the stability of the metal surface under electrodeposition, by improving the electrolyte conductivity at the metal electrode. This effect is particularly prominent at current densities where using a conventional salt electrolyte would lead to ion depletion and hence, large electric fields. At these current densities, the mobile ions in the tethered anion electrolyte are depleted at the metal. However, the fixed anions and their corresponding cations are still present and place a lower limit on the electrolyte conductivity at the metal electrode. Under these conditions, the electrolyte can be divided into two regions, a layer near the counter electrode with mobile anions in which transport is dominated by ambipolar diffusion and a layer near the metal

electrode devoid of mobile anions in which transport is dominated by the electromigration of the cations associated with the fixed anions. For cation diffusivity of 10^{-7} cm^2/s in a 1M total cation concentration with 10% fixed anions in a cell with 1 mm interelectrode spacing, the current density at which this region appears is 0.35 mA/cm^2 and the corresponding overpotential is 72 mV. The improvement in conductivity is seen very strongly at high overpotentials – at an overpotential of 144 mV, a 10% tethered anion electrolyte shows a 13% improvement in conductivity over a salt electrolyte, while a single ion conductor has 45% more conductivity compared to a salt electrolyte.

We then performed a stability analysis to determine the effect of fixed anions and surface tension on the stability of electrodeposition. In general, the growth rate of perturbations to the electrode surface grows with increasing wavelength due to the increasing concentration of mass flux lines on the more rapidly undulating surface until one reaches wavelengths at which the surface tension of the electrode is significant. At still smaller wavelengths, the growth rate decreases and eventually becomes negative indicating that the electrode is stable to small wavelength perturbations. Thus, there is a most unstable wavelength corresponding to the most rapidly growing perturbations and a critical wavelength below which the perturbations decay. We found that the critical wavelength can be increased and the growth rate of the most unstable mode reduced by increasing the fraction of tethered anions. An interesting outcome of the analysis is that the surface is significantly stabilized even when only a small amount portion (such as 10%) of the anions are immobilized. This indicates that even imperfect single ion conductors should be effective in curbing

dendritic growth compared to conventional salt based electrolytes.

In summary, we predict that tethering anions is effective in curbing dendrite growth at larger current densities and improving the electrolyte conductivity at large overpotentials. Experiments of Schaefer et al [2] have demonstrated an effective way of synthesizing tethering anions electrolytes that are electrochemically stable in lithium metal batteries and show improved conductivity. A single-ion Li^+ conducting electrolyte with all anions anchored to a porous membrane would provide another realization of this concept. However, a strict experimental comparison of the electrode stability in the presence of tethered anion electrolytes and salt electrolytes remains to be performed.

Based on the results for the critical wavenumber and growth rate of the most unstable mode, we expect the following strategies to be effective in curbing unstable electrodeposition of lithium. One strategy is to improve the conductivity of the electrolyte at the electrode surface. This is equivalent to reducing the electric field at the electrode surface, as proposed by Chazalviel [1]. An electrolyte containing a fraction of permanently anchored anions is one way of doing this. Using pulsating currents instead of continuous currents for charging can also reduce the electric field at the electrode surface [9, 10]. In this case, the square-wave charging currents prevent ion depletion at the electrode caused by continuous currents, thereby maintaining the electrolyte conductivity at the electrode surface and reducing the electric field. While the aforementioned approaches cannot stabilize the surface at all wavenumbers, this is not required to stop dendrite formation since the lateral dimension of the cell places a lower limit on the possible wavenumbers in the system. If the critical wavenumber is

brought below this value ($k_{cr} < \pi/w$, where w is the width of the cell), the electrodeposition will be stable at all wavenumbers in the cell and no dendrite growth should be observed. Alternately, the dendrite growth may be suppressed by constricting the transport to a length scale smaller than the critical wavelength such as, by using a porous separator of a pore size smaller than the critical wavelength [11]. A third strategy is to increase the surface tension of the salt-electrode couple to stabilize the electrodeposition. This may be done by using an appropriate solvent [12] and/or additives for the electrolyte [13-15]. The last, and perhaps obvious, strategy is to lower the charging current densities as can be seen from the low values of k_{cr} and σ_{mu} in Fig 10 at low overpotentials. This can explain the experimental observations of Barton and Bockris [6], who observed dendrite growth was absent at low overpotentials and current densities.

It should be noted that while none of these strategies may stabilize the electrodeposition by themselves, they should be more effective if used in conjunction. Improving the electrolyte conductivity at the electrode surface and lowering the charging currents can reduce the growth rate while enhancement of surface tension and constricting the length scale of the transport can lead to overall stability.

REFERENCES

1. Chazalviel, J-N. Electrochemical aspects of the generation of ramified metallic electrodeposits, *Phys. Rev. A*, **42**, 7355-7367 (1990)

2. Schaefer, J. L., Yanga, D. A. & Archer, L. A. High lithium transference number electrolytes via creation of 3-dimensional, charged, nanoporous networks from dense functionalized nanoparticle composites. *Chem. Mater.* **25**, 834-839 (2013)

3. Lu, Y., Das, S. K., Moganty, S. S., and Archer, L. A., Ionic-liquid nanoparticle hybrid electrolytes and their application in secondary lithium metal batteries, *Adv. Mater.*, **24 (32)**, 4430-4435 (2012).

4. Lu, Y., Korf, K. S., Kambe, Y., Tu, Z. & Archer, L. A. Ionic-liquid–nanoparticle hybrid electrolytes: applications in lithium metal batteries. *Angewandte Chemie. Intl Ed.,* **53**, 488-492 (2014)

5. Sundstrom, L. G. & Bark, F. H. On morphological instability during electrodeposition with a stagnant binary electrolyte. *Electrochim. Acta* **40**, 599-614 (1995)

6. Barton, J. L., and Bockris, J. O'M., The electrolytic growth of dendrites from ionic solutions, *Proc. R. Soc. Lond. A*, **268 (1355)**, 485-505 (1962).

7. Mani, A., and Bazant, M. Z., Deionization shocks in microstructures, *Phys. Rev. E*, **84 (6)**, 061504 (2011).

8. Monroe, C. & Newman, J. The impact of elastic deformation on deposition kinetics at lithium/polymer interfaces, *J. Electrochem. Soc.* **152**, A396-A404 (2005)

9. Mayers, M. Z., Kaminski, J. W., and Miller III, T. F., Suppression of dendrite formation via pulse charging in rechargeable lithium metal batteries, *J. Phys. Chem. C*, **116 (50)**, 26214-26221 (2012).

10. Popov, K. I., Stojilkovic, E. R., Radmilovic, V. and Pavlovic, M. G., Morphology of lead dendrites electrodeposited by square-wave pulsating overpotential, *Powder*

Tech., **93**, 55-61 (1997).

11. Tu, Z., Kambe, Y., Lu, Y. & Archer, L. A. Nanoporous polymer-ceramic composite electrolytes for lithium metal batteries. *Adv. Energy Mater.* **4**, 1300654 (2014)

12. Xu, K., Nonaquoeus liquid electrolytes for lithium-based rechargeable batteries, *Chem. Rev.*, **104**, 4303-4418 (2004).

13. Roha, D., and Landau, U., Mass transport of leveling agents in plating: steady-state model for blocking additives, *J. Electrochem. Soc.*, **137 (3)**, 824-834 (1990).

14. Ding, F., Xu, W., Graff, G. L., Zhang, J., Sushko, M. L., Chen, X., Shao, Y., Engelhard, M. H., Nie, Z., Xiao, J. & Liu, X. Dendrite-free lithium deposition via self-healing electrostatic shield mechanism. *J. Am. Chem. Soc.* **135**, 4450-4456 (2013)

15. Diggle, J. W., and Damjanovic, A., The inhibition of the dendritic electrocrystallization of zinc from doped alkaline zincate solutions, *J. Electrochem. Soc.*, **119 (12)**, 1649-1658 (1972).

CHAPTER 3

ELASTIC DEFORMATION OF THE TETHERED ANION ELECTROLYTE

In this section, we consider the effect of elastic deformation on the transport of ions through the tethered anion separator. The elastic deformation problem is solved assuming linear, elastic, Hookean deformations of the separator and metal electrode. The counterelectrode is assumed to be rigid. The growth of the electrode and separator is dictated by transport of ions across their interface and the electrode profile is obtained by imposing the constraint that the separator and electrode are to remain in contact with each other at all times. The elastic stresses also change the pressure in the separator, which in-turn affects the concentrations of the ions through its contribution to their chemical potentials, and therefore the equilibrium condition at the electrode surface. We thus, have a coupled problem wherein transport affects the deformation of the separator and metal electrode, and the deformation of the separator drives the transport of ions through the separator.

We discuss the deformation and transport problems in the two subsequent subsections while noting the factors that lead to their coupling. These, then, can be solved together to obtain the solution for growth of the electrode profile with time.

3.1 The transport problem

In formulating our transport equations, we model our electrolytes as ideal solutions for simplicity. The local chemical potential of the lithium ion (μ_c) and the mobile anion ($\mu_{a,m}$) in the separator can be written in terms of concentrations C_c and

$C_{a,m}$, electrostatic potential ϕ and pressure in the separator p^s,

$$\psi_c = \psi_c^{\ominus} + RT \ln C_c + F\phi + v_c p^s \tag{3.1}$$

$$\psi_{a,m} = \psi_{a,m}^{\ominus} + RT \ln C_{a,m} - F\phi + v_{a,m} p^s \tag{3.2}$$

Here v_c and $v_{a,m}$ are the partial molar volumes of the cation and the mobile anion in the separator. T represents temperature, and R and F are the ideal gas constant and Faraday's constant respectively. The fluxes of each ion can be derived from the gradients of chemical potentials as,

$$\mathbf{N}_c = -\mu_c C_c \nabla \psi_c = -RT\mu_c \nabla C_c - F\mu_c C_c \nabla\phi - v_c \mu_c C_c \nabla p^s \tag{3.3}$$

$$\mathbf{N}_{a,m} = -\mu_{a,m} C_{a,m} \nabla \psi_{a,m} = -RT\mu_{a,m} \nabla C_{a,m} + F\mu_{a,m} C_{a,m} \nabla\phi - v_{a,m} \mu_{a,m} C_{a,m} \nabla p^s \tag{3.4}$$

In each of the two equations above, the first term on the right hand side represents diffusion of the respective ion, the second term describes the migration of the ion under the action of the externally applied electric field, and the third term refers to the motion of the ion under the local pressure gradient [1-3]. The expressions assume the Einstein relation between diffusivity and mobility for both the cation and mobile anion, i.e. $D_c = RT\mu_c$ and $D_{a,m} = RT\mu_{a,m}$. We also assume that the mobile anion is in equilibrium and the current is carried entirely by the cation. We also assume local electroneutrality, which gives $C_c = C_{a,m} + C_0 C_{a,f}$.

The concentration of the fixed anions is also affected by the local deformation field, which compresses the matrix. Consider a three-dimensional element of volume ~~V~~ in the stress-less matrix of fixed anion concentration $C_{a,f0}$. Post deformation, the volume of the element becomes ~~V~~ + δ~~V~~ and the concentration of the fixed anions becomes $C_{a,f}$. By conservation of fixed charges within the element, we have,

$$C_{a,f0}\cancel{V} = C_{a,f}\left(\cancel{V} + \delta\cancel{V}\right) \tag{3.5}$$

Noting that, $\delta\cancel{V}/\cancel{V}$ is the volumetric strain in the matrix, and is related to the deformation field as $\delta\cancel{V}/\cancel{V} = \nabla\cdot\mathbf{u}^s$, we get

$$C_{a,f} = C_{a,f0}\left(1-\nabla\cdot\mathbf{u}^s\right) \tag{3.6}$$

The above governing equations are subject to boundary conditions of chemical equilibrium at the separator-counterelectrode and metal-separator interfaces. Chemical equilibrium at the metal-separator interface implies,

$$\psi_c^{\ominus} + RT\ln C_c + F\phi + \nu_c p^s = \psi_m^{\ominus} + F\phi_m + \nu_m p^m \tag{3.7}$$

The equilibrium at the separator-counterelectrode interface is similar, but without the term with the pressure in the electrode. In doing this, we assume that the storage in the counterelectrode involves intercalation which does not modify its chemical potential appreciably.

To evaluate the local pressure and deformation field, we, like Monroe and Newman [4], use the laws of linear elasticity. As will soon become apparent, the elasticity plays no role in the transport for flat, parallel electrodes. This is due to the fact that pressure in the separator is uniform in the case of planar electrodeposition. When performing the linear stability analysis with small sinusoidal perturbations, we will have small deformations of the electrode and the separator, so that linear elasticity is applicable.

3.2 The deformation problem

For an isotropic separator with linear elasticity, we can write the stress tensor in terms of the local deformation field $\mathbf{u}^s$ as,

$$\boldsymbol{\sigma}^s = \frac{2\nu^s G^s}{1-2\nu^s}\left(\nabla\cdot\mathbf{u}^s\right)\mathbf{I} + G^s\left[\nabla\mathbf{u}^s + \left(\nabla\mathbf{u}^s\right)^{\dagger}\right] \tag{3.8}$$

where G^s and ν^s are the shear modulus and the Poisson ratio of the separator. † denotes the transpose operation and $\mathbf{I}$ is the identity tensor. The pressure is given by the trace of the stress tensor as,

$$p^s = -\frac{1}{3}\mathrm{tr}\left(\boldsymbol{\sigma}^s\right) = -K^s\nabla\cdot\mathbf{u}^s \tag{3.9}$$

K^s is the bulk modulus of the separator and is related to G^s and ν^s as,

$$K^s = \frac{2\left(1+\nu^s\right)}{3\left(1-2\nu^s\right)}G^s \tag{3.10}$$

The local force balance on the separator implies $\nabla\cdot\boldsymbol{\sigma}^s = \mathbf{0}$. This gives,

$$\nabla^2\mathbf{u}^s + 2\alpha^s\nabla\left(\nabla\cdot\mathbf{u}^s\right) = \mathbf{0} \tag{3.11}$$

A similar balance for the metal and the pressure in the metal is obtained as,

$$\nabla^2\mathbf{u}^m + 2\alpha^m\nabla\left(\nabla\cdot\mathbf{u}^m\right) = \mathbf{0} \tag{3.12}$$

$$p^m = -K^m\nabla\cdot\mathbf{u}^m \tag{3.13}$$

Here α^s and α^m are related to the Poisson ratios of the separator and metal as,

$$\alpha^s = \frac{1}{2\left(1-2\nu^s\right)} \tag{3.14}$$

$$\alpha^m = \frac{1}{2\left(1-2\nu^m\right)} \tag{3.15}$$

The counterelectrode is assumed to be rigid.

The boundary conditions to the deformation problem are given by force balance and continuity of deformation at the separator-metal and separator-counter-electrode interfaces. At the separator-metal interface, we consider surface tension of the interface to act as a normal force on the metal electrode. The force balance, then, can be written as,

$$\mathbf{e}_n \cdot \boldsymbol{\sigma}^s\big|_{H_c} = \mathbf{e}_n \cdot \boldsymbol{\sigma}^m\big|_{H_c} + \gamma \mathrm{K} \mathbf{e}_n \tag{3.16}$$

Here, $\mathbf{e}_n$ is the unit normal to the surface of the electrode into the separator, γ is the surface tension and K is the local electrode curvature. For small deformations of the electrode surface profile H_c in the x-direction, the curvature is given by $\mathrm{K} = d^2 H_c / dx^2$.

The continuity of tangential deformation is written similarly as,

$$\left(\mathbf{I} - \mathbf{e}_n \mathbf{e}_n\right) \cdot \mathbf{u}^m\big|_{H_c} = \left(\mathbf{I} - \mathbf{e}_n \mathbf{e}_n\right) \cdot \mathbf{u}^s\big|_{H_c} \tag{3.17}$$

The normal deformation of the metal electrode and separator is given by the difference between the final electrode profile and its stress-free state. The stress-free state of the electrode is modified by transport, and grows due to the cations getting assimilated on the electrode surface. Likewise, the separator surface is also determined by the transport of cations across the metal-separator interface. This interpretation assumes that the growth of the unstressed electrode and separator due to transport remains stress-less. The stress in the deformed electrode and separator and their surface profiles comes from the constraint that the electrode and separator are required to remain in contact with each other at all times.

The stress-free profiles of the electrode (H_{sf}^{m}) and separator (H_{sf}^{s}) surfaces are, hence, given as,

$$\frac{\partial H_{sf}^{m}}{\partial t} = -v_m \frac{\left(\mathbf{e}_n \cdot \mathbf{J}\right)\big|_{H_c}}{F} \tag{3.18}$$

$$\frac{\partial H_{sf}^{s}}{\partial t} = -v_c \frac{\left(\mathbf{e}_n \cdot \mathbf{J}\right)\big|_{H_c}}{F} \tag{3.19}$$

Here, **J** is the current density vector of magnitude *J*, and v_m is the partial molar volume of the metal in the electrode. The current density vector is obtained from Faraday's laws of electrolysis as $\mathbf{J} = F\left(\mathbf{N}_c - \mathbf{N}_{a,m}\right)$. The deformation of the separator and electrode at the surface is given by,

$$\mathbf{e}_n \cdot \mathbf{u}^m\big|_{H_c} = H_c - H_{sf}^{m} \tag{3.20}$$

$$\mathbf{e}_n \cdot \mathbf{u}^s\big|_{H_c} = H_c - H_{sf}^{s} \tag{3.21}$$

This boundary condition is different from the corresponding one used by Monroe and Newman [4]. They regard the normal deformation as the imposed perturbation, which may be obtained by eliminating H_{sf}^{m} and H_{sf}^{s} from equations (3.20) and (3.21) respectively. This will be the case if the interface is deformed by an external force and will hence, yield an unusually conservative estimate of the separator modulus required to suppress the instabilities. The present formulation incorporates transport-driven growth of the electrode profile, thus expressing the stability as a net result of the competing factors of transport-driven destabilization and elasticity-promoted stabilization.

We start by solving the problem for planar, parallel, semi-infinite electrodes, with all deformations and fluxes in the *z*-direction, normal to the electrodes. In this case, we find that the pressure gradient terms in the transport equations vanish, because pressure in the separator is uniform. This gives,

$$N_c = -RT\mu_c \frac{dC_c}{dz} - F\mu_c C_c \frac{d\phi}{dz} \tag{3.22}$$

$$N_{a,m} = -RT\mu_{a,m} \frac{dC_{a,m}}{dz} + F\mu_{a,m} C_{a,m} \frac{d\phi}{dz} \tag{3.23}$$

The transport is governed by diffusion-migration of the cation and mobile anion with fast reaction kinetics at the two interfaces. We have previously shown that the solution for transport for such a case exhibits two qualitatively different behaviors (Fig 3.2). At small current densities, the transport is governed primarily by ambipolar diffusion of the cation throughout the separator (Fig 3.2b). Above a critical current density given as $J_{cr} = 4D_c FC_0 \left(1-2C_{a,f0}\right)/L$, the mobile anions are depleted at the metal electrode, leading to the formation of a depletion zone, wherein the cation exists solely to neutralize the fixed anions [5]. The mobile anions accumulate against the counter-electrode causing the interelectrode region to be divided into two zones – the diffusion region having ambipolar diffusion of the cation, and the migration region which is depleted of the mobile anion and where the primary transport mechanism is the electric-field-driven migration of the cations neutralizing the mobile anions (Fig 3.1a). The plots for the exact base state solutions for the cation concentration, electric potential and electric field profiles are shown in Fig 3.2 [6].

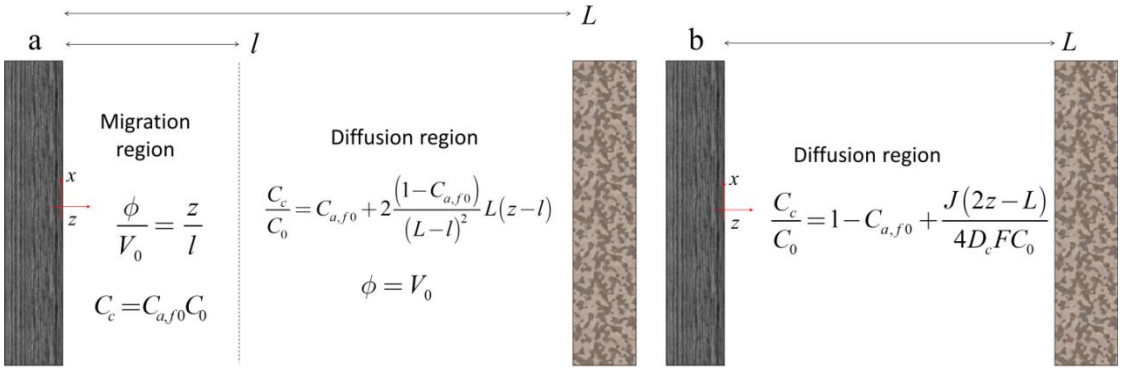

Figure 3.1: An approximate solution to the base state problem at steady state for: (a) High current densities and, (b) Low current densities, as shown in a previous work [6]. Above the critical current density J_{cr} = $4D_cFC_0(1 - 2C_{a,f0})/L$, the migration region which is devoid of mobile anions forms near the metal electrode. The same solution is valid even with the inclusion of pressure gradient driven transport, since pressure in the separator is uniform in the base state.

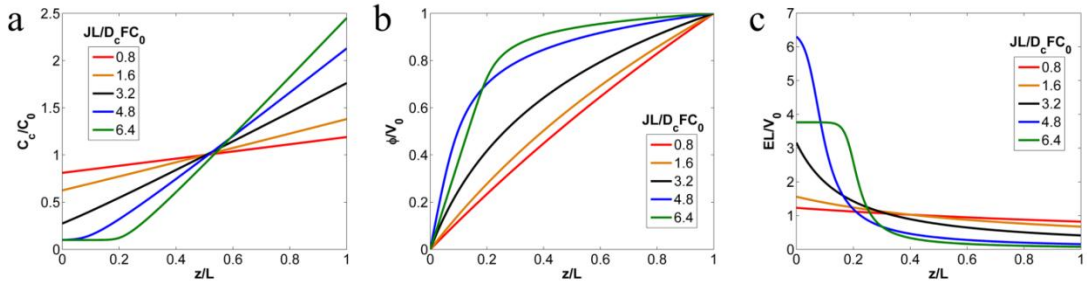

Figure 3.2: Base state solution to the steady state transport problem: (a) Cation concentration, (b) Electric potential, and (c) Electric field profiles. The fraction of immobilized anions $C_{a,f0}$ is 0.1, yielding a critical current density J_{cr} of $3.2D_cFC_0/L$. The profiles at the critical current density are indicated by the solid black lines.

3.3 Linear stability analysis

We perform a linear stability analysis of the base state transport solution by introducing regular perturbations to the electrode surface [$\tilde{H}_c = H_c + \varepsilon e^{\sigma t} e^{ikx}$] of arbitrarily small amplitude ε and known wavenumber k. For small amplitudes, the

perturbations to the concentration [$\tilde{C}_c = C_c + \varepsilon C_c'(z)e^{\sigma t}e^{ikx}$], potential [$\tilde{\phi} = \phi + \varepsilon\phi'(z)e^{\sigma t}e^{ikx}$] and current density [$\tilde{\mathbf{J}} = \mathbf{J} + \varepsilon\mathbf{J}'(z)e^{\sigma t}e^{ikx}$] are also expected to vary in the same manner. The deformation fields in the separator [$\tilde{\mathbf{u}}^s = \mathbf{u}^s + \varepsilon\mathbf{u}^{s'}(z)e^{\sigma t}e^{ikx}$] and the electrode [$\tilde{\mathbf{u}}^m = \mathbf{u}^m + \varepsilon\mathbf{u}^{m'}(z)e^{\sigma t}e^{ikx}$] are also perturbed in a regular fashion. The amplitudes of the perturbations grow with time if the real part of σ is positive, which implies unsteady electrodeposition leading to dendritic structures.

3.3.1 Large current densities

The two region model for high current densities is linearly perturbed as illustrated in Fig 3.3. This includes a perturbation to the boundary *l* between the diffusion and migration regions. The governing equations for transport are given by Stokes equations for cation concentration and potential in the diffusion and migration regions respectively. It is important to note that the pressure gradient term is no longer absent since the perturbation gives non-uniform pressure within the separator. The equations for the perturbed cation concentration and electrical potential are:

$$\frac{d^2C_c'}{dz^2} - k^2C_c' + \frac{v_c + v_{a,m}}{2RT}\frac{dC_c}{dz}\frac{dp^{s'}}{dz} = 0 \tag{3.24}$$

$$\frac{d^2\phi'}{dz^2} - k^2\phi' + \frac{1}{K^s}\frac{d\phi}{dz}\frac{dp^{s'}}{dz} = 0 \tag{3.25}$$

This gives the perturbation to current density in the diffusion and migration regions respectively as,

$$\mathbf{e}_z \cdot \mathbf{J}' = J' = -2RTF\mu_c \frac{dC_c'}{dz} - \mu_c F\left(v_c + v_{a,m}\right)C_c \frac{dp^{s'}}{dz} \quad \text{for } z > l \tag{3.26}$$

$$\mathbf{e}_z \cdot \mathbf{J}' = J' = -\mu_c F C_0 C_{a,f0}\left[F\frac{d\phi'}{dz} + F\frac{1}{K^s}p^{s'}\frac{d\phi}{dz} + \frac{RT}{K^s}\left(1+\frac{K^s v_c}{RT}\right)\frac{dp^{s'}}{dz}\right] \quad \text{for } z < l \tag{3.27}$$

The perturbations to the governing deformation equations (3.9), (3.11), (3.12), (3.13) yield,

$$\frac{d^2u_x^s}{dz^2} - k^2u_x^s + 2\alpha^s ik\left(iku_x^s + \frac{du_z^s}{dz}\right) = 0 \tag{3.28}$$

$$\frac{d^2u_z^s}{dz^2} - k^2u_z^s + 2\alpha^s \frac{d}{dz}\left(iku_x^s + \frac{du_z^s}{dz}\right) = 0 \tag{3.29}$$

$$\frac{d^2p^{s'}}{dz^2} - k^2p^{s'} = 0 \tag{3.30}$$

$$\frac{d^2u_x^m}{dz^2} - k^2u_x^m + 2\alpha^m ik\left(iku_x^m + \frac{du_z^m}{dz}\right) = 0 \tag{3.31}$$

$$\frac{d^2u_z^m}{dz^2} - k^2u_z^m + 2\alpha^m \frac{d}{dz}\left(iku_x^m + \frac{du_z^m}{dz}\right) = 0 \tag{3.32}$$

$$\frac{d^2p^{m'}}{dz^2} - k^2p^{m'} = 0 \tag{3.33}$$

where,

$$\mathbf{u}^{s'} = u_x^s\mathbf{e}_x + u_z^s\mathbf{e}_z \tag{3.34}$$

$$\mathbf{u}^{m'} = u_x^m\mathbf{e}_x + u_z^m\mathbf{e}_z \tag{3.35}$$

with $\mathbf{e}_x$ and $\mathbf{e}_z$ being the unit vectors in the x and z directions respectively.

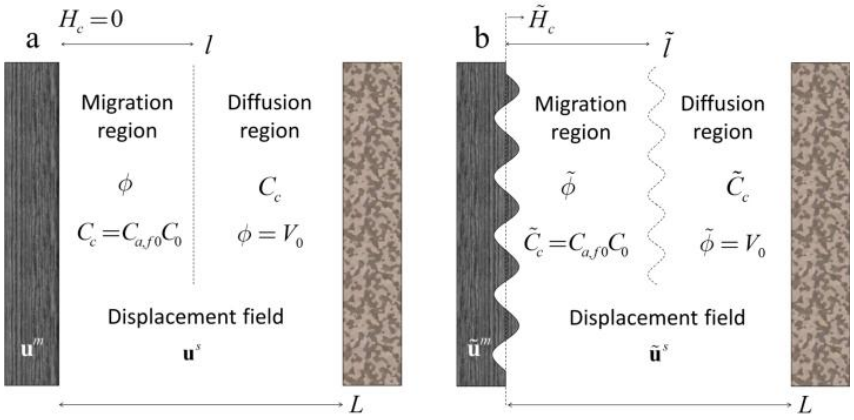

Figure 3.3: (a) Base state and (b) perturbed state of the problem at high current densities

The boundary conditions are given by continuity of concentration, potential and current density across the two region interface, and chemical equilibrium at the two electrodes. Continuity of concentration, potential and current density across the two region interface are written as,

$$C_c'\big|_l + \left.\frac{dC_c}{dz}\right|_l l' = 0 \tag{3.36}$$

$$\phi'\big|_l + \left.\frac{d\phi}{dz}\right|_l l' = 0 \tag{3.37}$$

$$-2RTF\mu_c \left.\frac{dC_c'}{dz}\right|_l = -\mu_c F C_0 C_{a,f0} \left[F \left.\frac{d\phi'}{dz}\right|_l + \frac{F}{K^s} p^{s\prime}\Big|_l \left.\frac{d\phi}{dz}\right|_l + \frac{RT}{K^s}\left(1 + \frac{K^s \nu_c}{RT}\right) \left.\frac{dp^{s\prime}}{dz}\right|_l \right] \tag{3.38}$$

The equilibrium at the metal-separator interface gives,

$$\nu_m\, p^{m\prime}\Big|_0 = F\left(\phi'\big|_0 + \left.\frac{d\phi}{dz}\right|_0\right) + \frac{RT}{K^s}\left(1 + \frac{K^s \nu_c}{RT}\right) p^{s\prime}\Big|_0 \tag{3.39}$$

Similarly, the equilibrium at the counter-electrode-separator interface is obtained as,

$$2RT\frac{C_c'\big|_L}{C_c\big|_L}+\left(\nu_c+\nu_{a,m}\right)p^{s\prime}\Big|_L=0 \tag{3.40}$$

The deformation boundary conditions based on force balance at the metal-separator interface and continuity of tangential and normal deformation in equations (3.16) – (3.21) at the metal-separator interface yield,

$$G^s\left[\left(2\alpha^s-1\right)ik\,u_x^s\big|_0+\left(2\alpha^s+1\right)\frac{du_z^s}{dz}\Big|_0\right]=G^m\left[\left(2\alpha^m-1\right)ik\,u_x^m\big|_0+\left(2\alpha^m+1\right)\frac{du_z^m}{dz}\Big|_0\right]+\gamma k^2 \tag{3.41}$$

$$G^m\left[ik\,u_z^m\big|_0+\frac{du_x^m}{dz}\Big|_0\right]=G^s\left[ik\,u_z^s\big|_0+\frac{du_x^s}{dz}\Big|_0\right] \tag{3.42}$$

$$u_x^s\big|_0=u_x^m\big|_0 \tag{3.43}$$

$$u_z^m\big|_0=1+\nu_m\frac{J'\big|_0}{F\sigma} \tag{3.44}$$

$$u_z^s\big|_0=1+\nu_c\frac{J'\big|_0}{F\sigma} \tag{3.45}$$

The corresponding boundary conditions at the counter-electrode-separator interface give,

$$u_x^s\big|_L=0 \tag{3.46}$$

$$u_z^s\big|_L=\nu_c\frac{J'\big|_L}{F\sigma} \tag{3.47}$$

Equations (3.36) – (3.47) can be solved in the large *kL* limit analytically. This limit is appropriate for describing LMB experiments, for which the widths of morphological instabilities (~1μm) are much smaller than typical inter-electrode distance (~1mm). The following results are for values of $kL > 5$, which corresponds to

dendrite widths of less than 628μm. Under such conditions, the counter-electrode is so far away that the perturbations to cation concentration and separator deformation field decay to insignificant values before they reach it. Therefore, equations (3.40), (3.46) and (3.47) can be replaced with $\lim_{kz\to\infty} C_c' = 0$, $\lim_{kz\to\infty} u_x^s = 0$, and $\lim_{kz\to\infty} u_z^s = 0$ respectively. Solving equations (3.36) – (3.55) gives,

$$\sigma = \frac{v_m}{\left(1-c_3^m\right)F}\left[kJ - v_m\mu_c K^m F C_{a,f0} C_0 k Z_1^m - \frac{1}{2}\left(1-\mathrm{e}^{-2kl}\right)JZ_1^s + \frac{K^s\left(v_c+v_{a,m}\right)}{4RT}JZ_1^s\,\mathrm{e}^{-2kl}\right] \quad (3.48)$$

where Z_1^m, c_3^m and Z_1^s are obtained from the solutions of,

$$Z_1^m\left[\frac{1+2\alpha^m}{1+2\alpha^s}G + \frac{1+\alpha^m}{1+\alpha^s}\right] - c_3^m k\left[\frac{2\left(G-V\right)}{1+2\alpha^s} + \frac{1+V}{1+\alpha^s}\right] = -k\frac{1-V}{\left(1+\alpha^s\right)\left(1+2\alpha^s\right)} \quad (3.49)$$

$$Z_1^m\left[1+\alpha^m+\alpha^m G\right] - c_3^m k\left[1-V\right] = -\frac{1}{2}\frac{\gamma}{G^s}k^2 - k\left[1-V\right] \quad (3.50)$$

$$Z_1^s\left[1+\alpha^s\right] = Z_1^m\left[1+\alpha^m\right] - c_3^m k\left[1+V\right] - k\left[1-V\right] \quad (3.51)$$

with G and V related to the moduli and partial molar volume of the cation in the two phases viz. separator and electrode as,

$$G = \frac{G^m}{G^s} \quad (3.52)$$

$$V = \frac{v_c}{v_m} \quad (3.53)$$

Thus, to obtain the growth rate of the perturbations, we first solve a set of linear algebraic equations, (3.49) – (3.51), for Z_1^m, c_3^m and Z_1^s, and then calculate σ from equation (3.48). Equations (3.49) – (3.51) are derived from the deformation problem represented by equations (3.41) – (3.47). Equation (3.48), which yields the growth rate

is derived from the solution to the transport problem (3.36) – (3.40) and substituting into (3.44) for σ.

The result in equation (3.48) is unaffected by the boundary conditions at the counter-electrode because we have assumed $kL >> 1$ so that the perturbations decay before they reach the counter-electrode. The net result is therefore solely dependent on the conditions in the neighborhood of the metal electrode. Each term in equation (3.48) represents a particular mechanism influencing the perturbation growth rate, as summarized in Table 3.1. The first term of the expression in the square brackets refers to the *convergence of electrical flux* on the tips of the perturbation caused by interfacial deformation alone. This is the primary mechanism for the roughening of the interface. This term varies linearly with the deposition rate, and is hence proportional to the current density. The second term represents the effect of stresses on the equilibrium at the electrode-separator interface. Regions of higher pressure in the electrode experience *elasticity-induced reaction retardation* due to the larger pressure work needed to reduce a cation and form a metal atom at the interface. For separators with small moduli, *surface tension* of the metal-separator interface serves the role of modulating the electrode pressure and thereby altering the reaction equilibrium. The third term reflects the effect of *spatial variations in electrolyte conductivity* near the electrode surface caused by *separator deformation*. As seen before, compression of the separator matrix increases the local concentration of the tethered anions. In a separator with a spatially varying deformation field, this matrix compression causes a spatial variation in the concentration of the tethered anions and, through electroneutrality the local cation concentration and ionic conductivity. This also

affects the current distribution to the electrode surface, as regions of higher conductivity experience higher current densities and faster deposition. Finally, the last term reflects the influence of the diffusion region on the stability of deposition. While high pressure tends to increase the concentration of the immobilized salt by compression of the solid matrix to which the salt is tethered, the mobile salt is driven by the *pressure-driven flux* from high to low pressure locales in the separator due to the chemical potential gradient mentioned earlier in equations (3.3) and (3.4). For perturbation wavelengths comparable to or smaller than the migration region thickness, the diffusion region has a significant contribution to the growth of such perturbations. This phenomenon will predictably supplant the matrix compression effect at small current densities, where the migration region is absent.

Table 3.1: Transport mechanisms and their stabilizing behavior, based on parameter values used in Table 3.2.

Term no.	**Term in eq. (56)**	**Transport mechanism**		**Destabilizing/ Stabilizing**
1	kJ	Electric flux due to surface deformation		Destabilizing
2	$\nu_m \mu_c K^m F C_{a,f0} C_0 k Z_1^m$	Change of reaction equilibrium due to electrode pressure caused by:	(a) Separator modulus	Stabilizing
			(b) Surface tension	Stabilizing
3	$\frac{1}{2}\left(1-\mathrm{e}^{-2kl}\right) JZ_1^s$	Change in ionic conductivity in migration region due to separator compression		Destabilizing
4	$\frac{K^s\left(\nu_c+\nu_{a,m}\right)}{4RT} JZ_1^s \mathrm{e}^{-2kl}$	Pressure-driven flux in diffusion region. Pressure caused by:	(a) Separator modulus	Stabilizing
			(b) Surface tension	Destabilizing

To evaluate the growth rate of the perturbations per mole of metal electrodeposited, we scale the growth rate with current density to account for the inherent increase in growth rate with current density. The wavenumber is multiplied by the separator thickness, which is the primary length scale for transport in the base state. As the wavenumber provides the length scale for transport in the perturbed state, this scaling benchmarks the perturbed state against the base state. The scaled growth rate is plotted in Fig 3.4. The values of parameters used in these plots, shown in Table 3.2, are specific to the electrodeposition of lithium. The values for ν_c and $\nu_{a,m}$ are specifically for lithium (Li^+) and bis(trifluoromethane) sulfonimide ($TFSI^-$ or $(CF_3SO_2)_2N^-$) ions in ethylene glycol [7] and will obviously change with the electrodeposition system [8].

Table 3.2: Standard parameter values

Symbol	Parameter name	Value	Ref.
ν_c	Partial molar volume of cation in the separator	-8×10^{-6} m^3/mol	7
$\nu_{a,m}$	Partial molar volume of mobile anion in the separator	1.78×10^{-4} m^3/mol	7
ν_m	Partial molar volume of cation in the metal	1.3×10^{-5} m^3/mol	4
ν^s	Poisson's ratio of the separator	0.33	4
ν^m	Poisson's ratio of the metal	0.33	4
G^m	Shear modulus of the metal	3.4 GPa	4
γ	Surface tension of the electrode-separator interface	1.716 N/m	4
L	Inter-electrode distance	1 mm	

For the chosen parameter values, we find that the contributions of the first and third terms in equation (3.48) to σ are positive, while those of the second and last

terms are negative. The growth of the perturbation by concentration of *electric flux* lines is destabilizing, as expected. The compressive stress in the electrode is stabilizing because the pressure in the electrode is higher at the peaks, thus creating an *elasticity-induced retardation of the deposition* on the peaks. The effect of *separator matrix compression on the local ionic conductivity* is destabilizing. This is also reasonable; the separator is compressed on perturbation peaks and dilated in the valleys giving a higher fixed anion concentration on the peaks. Consequently, the conductivity is higher on the peaks, increasing the cation flux on the peaks in addition to the flux concentration mechanism of the first term. The last term, which describes the *pressure-driven flux* in the diffusion region, is stabilizing because the higher pressure in the peaks drives the ions into the low pressure valleys. This term is important for large wavelength perturbations (small k) but its significance diminishes quickly at higher k. The last two terms are absent if the analysis is performed without including the elastic deformation [6].

Fig 3.4a shows the variation of the scaled growth rate with wavenumber for a fixed anion fraction of 0.1, for various values of separator shear modulus, while Fig 3.4b depicts the same variation for varying fixed anion fractions at a constant separator modulus of 1 MPa. Both figures suggest that small wave number perturbations are unstable, while the large wave number perturbations are rendered stable by the combined effect of the *elasticity induced reaction retardation* and *surface tension*. The stability of electrodeposition is improved both by increasing the fraction of immobilized anions as well as the separator shear modulus. The small difference between the low modulus (100 kPa) case and the result obtained previously

in an analysis that ignored elastic deformation [6] originates from the second term in equation (3.48), which describes the effect of *separator matrix compression on the local ionic conductivity*. Although this mechanism makes the growth rate in a low modulus electrolyte different from that in a hypothetical case that ignores both elastic stresses and deformation, the difference is modest, meaning that for LMBs based on low modulus polymer or gel polymer electrolytes, the previous analysis provides a sufficiently accurate result to guide material design.

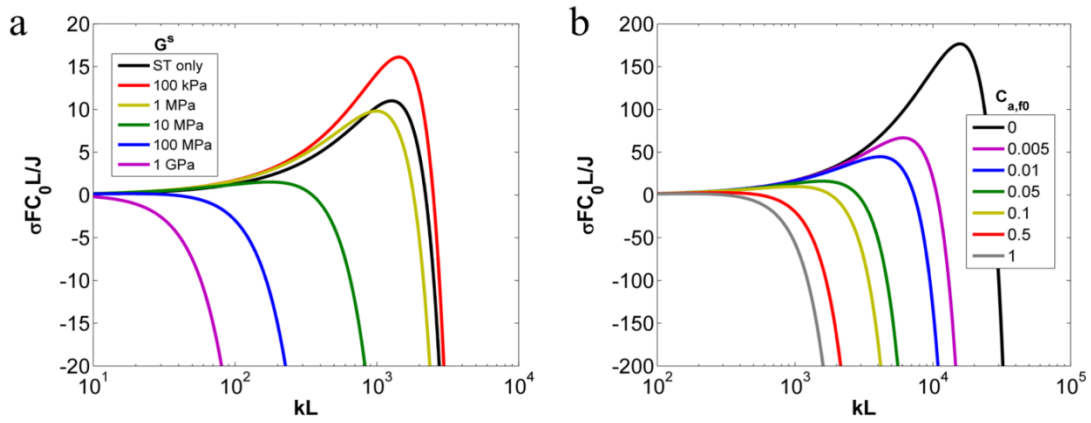

Figure 3.4: Large current density growth rate vs wavenumber plots for (a) $C_{a,f0}$ = 0.1 with varying G^s, and (b) G^s = 1MPa with varying $C_{a,f0}$. The black line in Fig 3.4a corresponds to the result with elasticity excluded and only the effect of surface tension being considered.

The wavenumber dependence in Fig 3.4 can be analyzed further by extracting the wavenumber of the marginally stable mode, also called the critical wavenumber k_{cr}, and growth rate of the least stable mode σ_{mu}. The critical wavenumber is the value of k at which σ changes sign from positive to negative. It corresponds to the physical situation where the driving forces for destabilizing the deposition, viz. transport, are

equal to the stabilizing driving forces of surface tension and elasticity. This mode is thus, neutrally stable and would correspond to the smallest observable sizes of the morphological instabilities. The most unstable mode corresponds to the value of *k* at which the largest growth rate is predicted. If the initial growth rate is indicative of the surface perturbations that continue to grow fastest at finite amplitude then this will be the most prominently observed length scale of the surface roughness or dendrite size on the metal surface. The critical wavenumber and the growth rate of the least stable mode can be obtained from equation (56) as follows.

$$\sigma\left(k_{cr}\right)=0 \tag{3.54}$$

$$\sigma\left(\frac{d\sigma}{dk}=0\right)=\sigma_{mu} \tag{3.55}$$

It is apparent from Fig 3.5 that both parameters can be reduced by increasing the fraction of fixed anions and the separator/electrolyte modulus, leading to improved stability of deposition. It is also important to note the improvement in the stability of deposition is achieved at lower separator moduli by immobilizing a fraction of anions. This effect is dramatic within the first 10% of tethering and more gradual thereafter, meaning that one need not use single ion conductors to observe them in laboratory experiments.

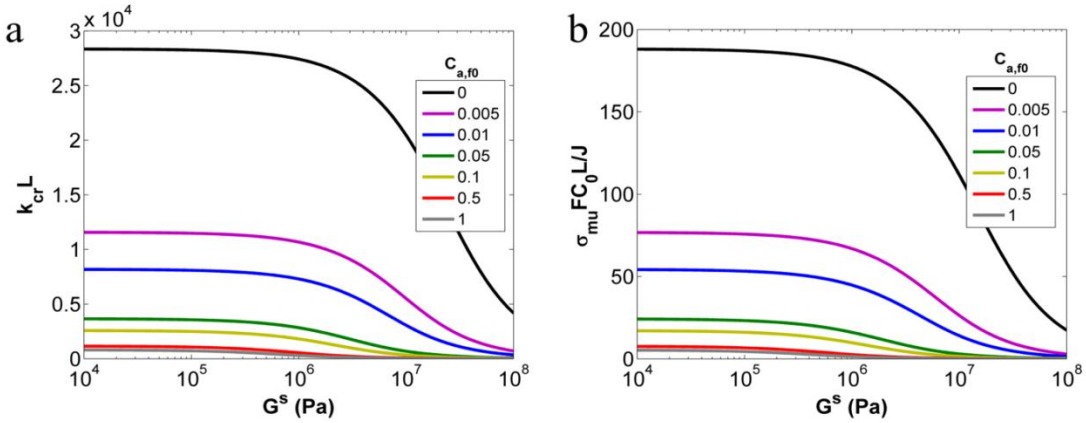

Figure 3.5: (a) Critical wavenumber and (b) Growth rate of the most unstable mode as a function of separator shear modulus for various fractions of immobilized anions

3.3.2 Small current densities

Below the critical current density, transport across the separator is driven by ambipolar diffusion and pressure-gradient driven flux. On perturbing it, therefore, as shown in Fig 3.6, the governing transport equation is,

$$\frac{d^2C_c'}{dz^2} - k^2 C_c' + \frac{v_c + v_{a,m}}{2RT}\frac{dC_c}{dz}\frac{dp^{s'}}{dz} = 0 \tag{3.56}$$

The boundary conditions are given by perturbations to the fast reaction kinetics at the two and can be written at the metal and the counter-electrode respectively as,

$$v_m\, p^{m'}\Big|_0 = \frac{2RT}{C_c\big|_0}\left(C_c'\big|_0 + \frac{dC_c}{dz}\Big|_0\right) + \left(v_c + v_{a,m}\right) p^{s'}\Big|_0 \tag{3.57}$$

$$2RT\,\frac{C_c'\big|_L}{C_c\big|_L} + \left(v_c + v_{a,m}\right) p^{s'}\Big|_L = 0 \tag{3.58}$$

The perturbed deformation governing equations and boundary conditions are the same as the high current density case, viz. equations (3.41) – (3.47) respectively. As before,

equations (3.40), (3.46) and (3.47) can be replaced by $\lim_{kz\to\infty} u_x^s = 0$, $\lim_{kz\to\infty} u_z^s = 0$, and $\lim_{kz\to\infty} C_c' = 0$ respectively in the large *k* limit. Solving these equations for the growth rate in the large *k* limit gives,

$$\sigma = \frac{v_m}{\left(1-c_3^m\right)F}\left[kJ - v_m \mu_c K^m F\, C_c\big|_0\, kZ_1^m + \frac{K^s\left(v_c + v_{a,m}\right)}{4RT} JZ_1^s\right] \tag{3.59}$$

where Z_1^m, c_3^m and Z_1^s are obtained from equations (3.49) – (3.53).

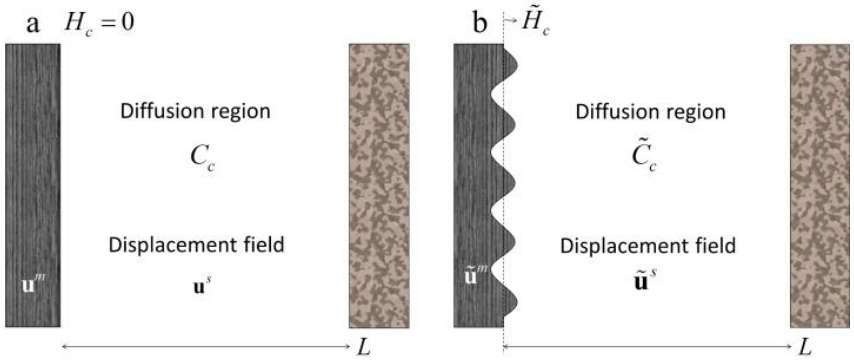

Figure 3.6: (a) Base state and (b) perturbed state of the problem at low current densities

Comparing each of the terms in square brackets in equation (3.59) to their corresponding counterparts in (3.48), we find that the first two terms represent the convergence of electrical flux and electrode compression respectively, while the last term in (3.59) is like the last term in (3.48), viz. the contribution of pressure-gradient driven transport. As with the case of high current densities, the convergence of flux on perturbation tips is destabilizing while compression of the electrode and the pressure-driven flux are stabilizing. The third term in (3.48) representing the matrix

compression effect is absent here because the current densities are lower than the critical value required for forming the migration region.

The plots for current density normalized growth rate for small current densities are shown in Fig 3.7. The critical wavenumber and the growth rate of the least stable mode, as defined in equations (3.54) and (3.55) respectively are plotted in Fig 3.8. The effect of anion tethering is less pronounced in this case because the current is primarily carried by the mobile salt. The growth rates are also smaller due to the smaller current densities. The role of separator elasticity is the same as in the high current densities case.

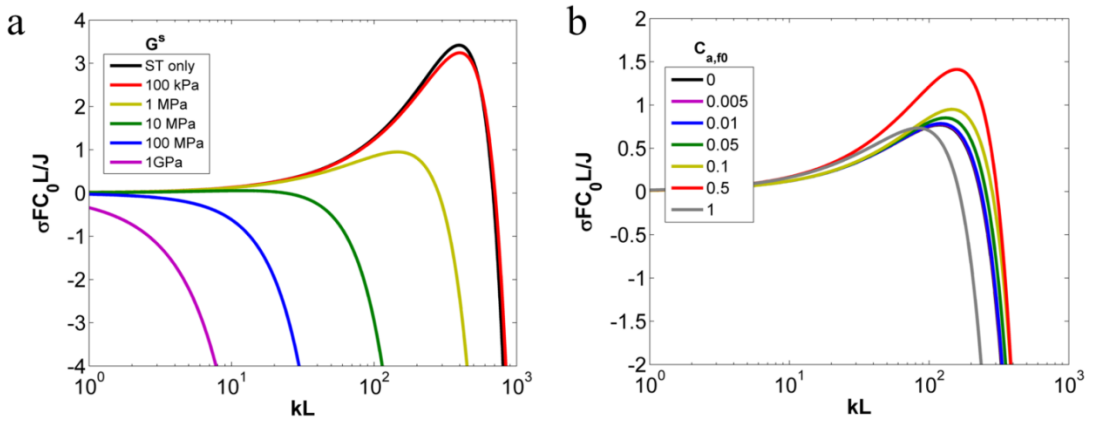

Figure 3.7: Growth rate as a function of wavenumber for (a) $C_{a,f0}$ = 0.1 with varying G^s, and (b) G^s = 1MPa with varying $C_{a,f0}$ at small current densities.

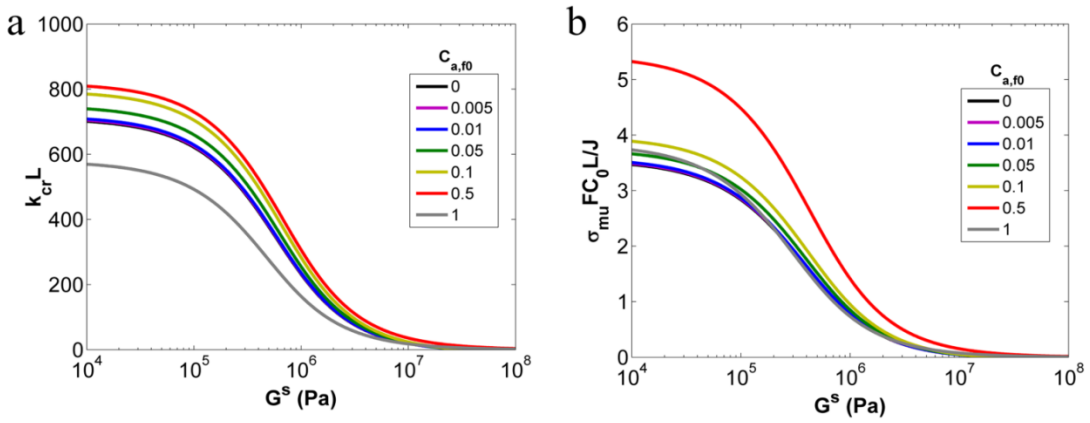

Figure 3.8: (a) Critical wavenumber and (b) Growth rate of the most unstable mode as a function of separator shear modulus for various fractions of immobilized anions at small current densities.

The large and small current density results are compiled in Fig 3.9, which shows the variation of the critical wavenumber with current density for various fixed anion fraction and separator modulus. As expected, the critical wavenumber increases with current density, reflecting the decreased stability of deposition due to higher flux concentrating on the perturbation tips. This is consistent with the observations of several studies that dendrite proliferation was promoted at higher current densities [9-17]. The effectiveness of the anion tethering (Fig 3.9a), which was demonstrated in recent studies [18-20], as well as the suppression effect of higher separator moduli (Fig 3.9b) noted by Stone et al [21] is also seen in the reduction of the critical wavenumber of the perturbation. It is also important to note that stability of all modes can be achieved, as can be seen in the cases of G^s = 1 GPa in Fig 5a and G^s = 100 MPa and 1 GPa in Fig 3.7a.

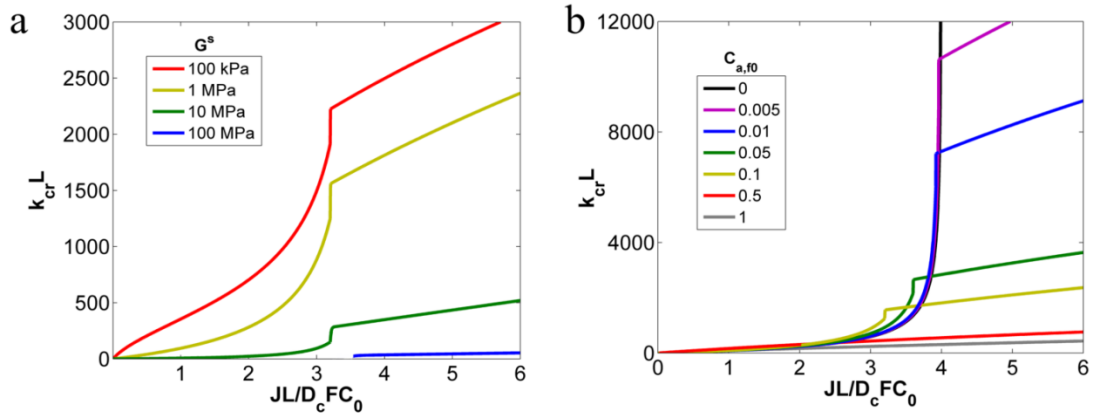

Figure 3.9: Critical wavenumber vs current density for (a) $C_{a,f0}$ = 0.1 with varying G^s, and (b) G^s = 1MPa with varying $C_{a,f0}$

3.3.3 Dimensional analysis

In the presentation above, we have shown the stability characteristics for dimensional parameters chosen to reflect lithium ion transport to a lithium metal electrode through ethylene glycol. We noted that the stability results from four mechanisms – the destabilizing effect of *convergence of electrical flux* on perturbation tips, and the stabilizing roles of *pressure driven flux* from high to low pressure regions, *elasticity-induced reaction retardation* of the deposition process and *surface tension* of the metal-separator interface. While this is an important application of current interest for high energy density LMB electrolyte and separator design, it is also valuable to consider the present analysis in a broader context. For this purpose, we introduce the dimensionless parameters that govern the problem. We choose L as the length scale for all spatial parameters in the inter-electrode space because it is the characteristic length for transport in the base state problem. Deformation field in the

electrolyte are also scaled by L. Deformation fields in the metal are scaled by LG^s/G^m to account for the difference in moduli of the separator and metal. All concentrations are scaled by the equilibrium salt concentration C_0 and chemical potentials are scaled by RT. Pressure and stresses in the separator are scaled by the separator modulus G^s, while the electrode stresses and pressure are non-dimensionalized by the electrode modulus G^m. The growth rate is scaled as J/FC_0L to account for its inherent increase with increasing current density as mentioned earlier. The above equations are, thus, non-dimensionalized as $x^* = x/L$, $z^* = z/L$, $\tilde{l}^* = \tilde{l}/L$, $\tilde{\mathbf{u}}^{s*} = \tilde{\mathbf{u}}^s/L$, $\tilde{\mathbf{u}}^{m*} = \tilde{\mathbf{u}}^m G^m/LG^s$, $k^* = kL$, $\sigma^* = \sigma FC_0 L/J$, $\tilde{C}_c^* = \tilde{C}_c/C_0$, $v_c^* = v_c C_0$, $v_{a,m}^* = v_{a,m} C_0$, $v_m^* = v_m C_0$, $\tilde{p}^{s*} = \tilde{p}^s/G^s$, $\tilde{p}^{m*} = \tilde{p}^m/G^m$, $K^{s*} = K^s/G^s$, $K^{m*} = K^m/G^m$, $J^* = JL/D_c FC_0$. Some parameters such as the Poisson ratios v^s and v^m, α^s and α^m, and the ratios of metal to separator modulus, G, and partial lithium partial molar volume, V, are dimensionless and are retained as such. The critical current density for the transition from small current densities to large current densities then becomes $J_{cr}^* = 4\left(1-2C_{a,f0}\right)$.

The non-dimensional form for the growth rate at high current densities expressed in equation (3.48) is then obtained as,

$$\sigma^* = \frac{v_m^*}{1-c_3^{m*}}\left[k^* - \frac{1}{\mathrm{Ee}}K^{m*}C_{a,f0}k^* Z_1^{m*} - \frac{1}{2}\left(1-\mathrm{e}^{-2k^*\tilde{l}^*}\right)Z_1^{s*} + \frac{1}{4}K^{s*}\,\mathrm{Eo}\,Z_1^{s*}\,\mathrm{e}^{-2k^*\tilde{l}^*}\right] \qquad (3.60)$$

where Z_1^{m*}, c_3^{m*} and Z_1^{s*} are obtained from the non-dimensional forms of equations (3.49) – (3.51),

$$\frac{Z_1^{m*}}{G}\left[\frac{1+2\alpha^m}{1+2\alpha^s}G + \frac{1+\alpha^m}{1+\alpha^s}\right] - \frac{c_3^{m*}}{G}k^*\left[\frac{2(G-V)}{1+2\alpha^s} + \frac{1+V}{1+\alpha^s}\right] = -k^*\frac{1-V}{\left(1+\alpha^s\right)\left(1+2\alpha^s\right)} \qquad (3.61)$$

$$\frac{Z_1^{m*}}{G}\left[1+\alpha^m+\alpha^m G\right]-\frac{c_3^{m*}}{G}k^*\left[1-V\right]=-\frac{1}{2}\mathrm{Ec}\,k^{*2}-k^*\left[1-V\right] \tag{3.62}$$

$$Z_1^{s*}\left[1+\alpha^s\right]=\frac{Z_1^{m*}}{G}\left[1+\alpha^m\right]-\frac{c_3^{m*}}{G}k^*\left[1+V\right]-k^*\left[1-V\right] \tag{3.63}$$

Similarly, for the small current densities case, we obtain

$$\sigma^*=\frac{\nu_m^*}{1-c_3^{m*}}\left[k^*-\frac{1}{\mathrm{Ee}}K^{m*}C_c^*\Big|_0 k^*Z_1^{m*}+\frac{1}{4}K^{s*}\,\mathrm{Eo}\,Z_1^{s*}\right] \tag{3.64}$$

where Z_1^{m*}, c_3^{m*} and Z_1^{s*} are obtained from equations (3.61) – (3.63).

Four non-dimensional numbers appear in the above analysis. The first, the Elasto-osmotic number, is the ratio of the shear elastic modulus to the osmotic pressure of the ions and is defined as,

$$\mathrm{Eo}=\frac{G^s\left(\nu_c+\nu_{a,m}\right)}{RT} \tag{3.65}$$

It reflects the ability of elastic stresses to alter the ion transport mechanisms by producing a *pressure driven flux* in the diffusion region. The convergence of electric flux on dendrite tips destabilizes deposition. However, the elastic stresses in the separator caused by the growth of the perturbation create a pressure gradient that drives ions away from the perturbation tips. This secondary mechanism, as discussed before, is stabilizing. The Elasto-osmotic number compares the strength of this secondary stabilizing mechanism to the primary electric flux driven destabilization. The Elasto-osmotic number therefore reflects the separator elasticity non-dimensionalized by transport in the diffusion region. As elasticity has multiple mechanisms in the deposition process, we should expect at least one more

dimensionless group based on separator modulus determining the stability of deposition.

The second dimensionless group that appears in equation (3.62), is the Elastocapillary number,

$$\mathrm{Ec} = \frac{\gamma}{G^s L} \tag{3.66}$$

This group measures the relative effects of surface tension and elastic stresses and also appears in descriptions of extensional deformations of polymers with free surfaces [22], contact of soft elastic solids with liquids [23] or other solids [24]. In the present study, the magnitude of Ec indicates whether surface tension or separator elasticity has a more pronounced effect on the pressure in the electrode and the separator thereby stabilizing the deposition by modulating the *reaction equilibrium* and the *pressure-driven ionic flux*. The role of surface tension becomes more important when $k^* > 1/\mathrm{Ec}$, as can be seen from equation (3.62).

The third dimensionless group emerges from equations (3.60) and (3.64). We define it as the Electrical-Elastic number Ee,

$$\mathrm{Ee} = \frac{JL}{\nu_m \mu_c F C_0 G^s} \tag{3.67}$$

Ee compares the relative importance of *convergence of electrical flux* on perturbation tips and *elasticity-induced retardation of the deposition reaction* on the tips.

Although the four dimensionless groups defined above are sufficient to describe the growth rate, we can also define an Electrical-Bond number Eb. This dimensionless group arises when equation (3.62) is substituted into equations (3.60)

and (3.64), from the combination of the Electrical-Elastic number Ee and the Elastocapillary number Ec. As stated earlier, surface tension becomes important for deposition of modes where $k^* = \mathrm{O}(1/\mathrm{Ec})$. This suggests that for extremely soft separators, the Electrical-Elastic number should be replaced by a different group, based on the convergence of electrical flux and surface tension. The number so obtained is the Electrical-Bond number Eb,

$$\mathrm{Eb} = \frac{\mathrm{Ee}}{\mathrm{Ec}} = \frac{JL^2}{v_m \mu_c F C_0 \gamma} \tag{3.68}$$

The Electrical-Bond number (Eb) is the electrical analogue of the better-known Bond number [25, 26], which compares the role of gravitational forces to surface tension. In the analysis of electrodeposition, Eb compares the relative strength of electrical forces, here in the form of current density, to the surface tension. The Electrical-Elasticity number (Ee) can be thought of as the elasticity-equivalent of the Electrical-Bond number.

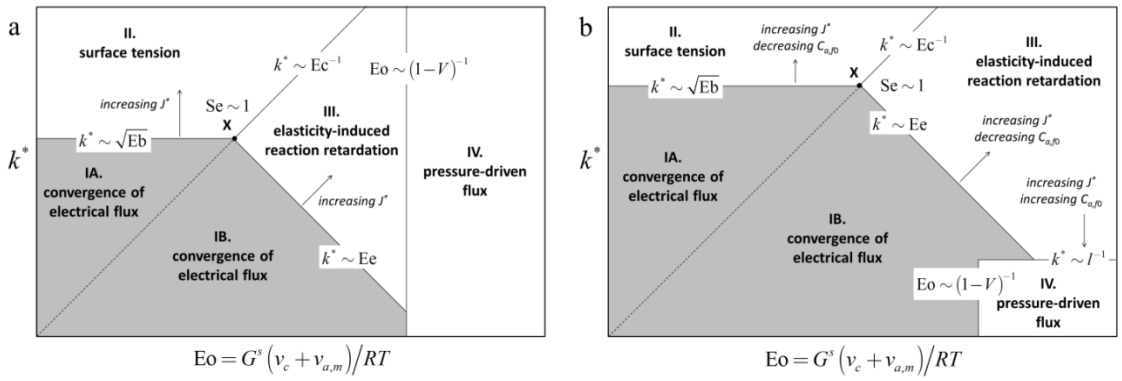

Figure 3.10: Dominant mechanism in the stability of electrodeposition at various dimensionless wavenumbers and separator moduli for (a) small current densities and (b) large current densities. The shaded region is unstable. See text for the definitions of the various dimensionless groups.

The influence of these non-dimensional groups on the stability at various separator moduli and deposition length scales is represented in the form of a map in Fig 3.10. The elastic deformation of the separator plays two fundamental roles in improving the stability. First, it alters the chemical potential gradient of the ions through the pressure, as reflected in the second and fourth terms in the square parenthesis in equation (3.60) and the second term in equation (3.64). For the mobile salt, the pressure gradient in the electrolyte/separator generates a chemical potential gradient that drives the mobile salt away from regions of high pressure, which in the present case, is on the perturbation tips. The relative contribution of this phenomenon against the convergence of electrical flux on the perturbation tips for separators much less stiff that the electrode, i.e. $G^s \ll G^m$, goes as $\mathrm{Eo}(1-V)$. The immobile salt on the other hand, has a higher concentration in regions of high pressure, thus increasing the flux. For $G^s \ll G^m$, this term makes a contribution relative to the convergence of electrical flux as $1-V$. The absence of a dependence on the Elasto-osmotic number can be explained from the fact that this mechanism is based on the volumetric compression of the separator caused by the pressure, rather than the actual value of the pressure itself. At small current densities where the transport is dominated by the mobile salt, this transport mechanism can stabilize the deposition for all modes for large separator moduli (Region IV in Fig 3.10a). For large current densities, the thickness of migration region controls the relative strengths of the mobile salt and the immobile salt in the stability of deposition. The location of this boundary, therefore, changes.

The second role played by elasticity in the stability analysis is through its effect on the interfacial dynamics, by retarding the deposition reaction on the perturbation tips. This phenomenon is captured in the third terms of equations (3.60) and (3.64) for large and small current densities respectively. The relative strength of this mechanism can be compared to the convergence of electrical flux on perturbation tips through the Electrical-Elastic number Ee and is wavenumber dependent as k^*/Ee. The retardation of the deposition reaction thus outweighs the convergence of electrical flux for $k^* \gg \mathrm{Ee}$ (Region III in Fig 3.10a). Reducing the separator modulus to extremely low values increases the Electrical-Elastic number, and thus the elasticity-induced slowing of interfacial deposition becomes important only at larger k^*.

For even smaller separator moduli, surface tension is important relative to the separator elasticity and suppresses perturbation growth by electrical flux for $k^* \gg \sqrt{\mathrm{Eb}}$ (Region II in Fig 3.10). This is consistent with our previous result [6]. The boundary between regions I and II indicates this transition. Similarly, the boundary between regions I and III denotes the transition from unstable deposition due to *convergence of electrical flux* and stable deposition caused by *elasticity induced reaction retardation*, as seen earlier. The intersection of these two boundaries thus gives the transition from surface tension induced stability to elasticity caused stability, which can be predicted by a Surface tension-Elasticity number Se,

$$\mathrm{Se} = \frac{\mathrm{Ee}}{\sqrt{\mathrm{Eb}}} = \frac{1}{G^s}\sqrt{\frac{J\gamma}{\mu_c F C_0 \nu_m}} \tag{3.69}$$

For Se < 1, elasticity is the prominent mechanism for stability. For J^* = 2 and parameter values used in Table 3.2, this transition happens for G^s > 0.81 MPa.

Both the Electrical-Bond (Eb) and Electrical-Elastic (Ee) numbers increase with current density. The boundaries between the regions I and II, and regions I and III in Fig 3.10a are hence dependent on current density and region I, viz. zone of converging electrical flux, expands as the square root of current density. The boundaries between region II and region III, based on the Elastocapillary number (Ec) signifying the importance of surface tension relative to elasticity remains invariant with current density. Region IV, which represents the role of pressure-gradient driven transport is based on the Elasto-osmotic number (Eo) and also remains independent of current density. Below the critical current density, the fixed anions have no contribution to transport and hence the above behaviors are independent of $C_{a,f0}$.

Above the critical current density, the behaviors of Eb and Ee with current density remain the same as above, as can be seen in Fig 3.10b. The formation of the migration region restricts the pressure gradient driven transport to the now smaller diffusion region, thus shrinking region IV to modes smaller than the migration region thickness only, i.e. $k^* < l^{-1}$. The migration region becomes thicker with increasing current density or fixed anion fraction, thus making this restriction stronger. The sizes of the other zones are also affected by $C_{a,f0}$ at higher current densities because the immobile anions have a significant effect on cation transport. Increasing the fraction of fixed anions reduces the electric field at the metal electrode as discussed earlier, which in turn reduces convergence of electrical flux, thus contracting region I.

3.3.4 Marginal stability

We have seen in the previous section that at large enough separator moduli (Region IV in Fig 3.10), the deposition-induced pressure gradient in the separator can reverse preferential deposition by creating a chemical potential gradient for the ions away from the perturbation tips. We also noted that this reversal occurs at all wavenumbers and therefore can stabilize deposition of all modes. This motivates a detailed search for the criteria for marginal stability – the boundary in parameter space beyond which the deposition is stable for all perturbations. As stated earlier, marginal stability occurs at separator moduli where surface tension is negligible. Ignoring surface tension in equations (3.61) – (3.63), Z_1^{m*} and Z_1^{s*} are both proportional to k^*. This implies that the first two terms of equations (3.60) and (3.64) are proportional to k^* while the third term goes as k^{*2}. As a result, in the relative competition of the corresponding mechanisms over various modes, we may expect that concentration of current density and separator compression to compete equally at all modes, while the electrode stress driven changes in deposition rate can suppress instabilities above a certain k^* value.

Thus, high wavenumber perturbations are rendered stable by the retardation of the interfacial reaction by electrode pressure, arising from the elastic deformation of the separator and surface tension on tips in both low and high current densities. Therefore marginal stability is achieved when deposition at small wavenumbers is stabilized. This gives a relation between the three parameters – the fraction of immobilized anions ($C_{a,f0}$), the Elasto-osmotic number (Eo), and the Electrical-elastic number (Ee), or in dimensional terms – the fraction of immobilized anions ($C_{a,f0}$), the

separator modulus (G^s) and the current density (J) for the boundary beyond which the deposition is universally stable. This relation can be determined by setting $\sigma_{mu} = 0$ for both large and small current densities.

For small current densities, the marginal stability limit can be obtained from equations (3.61) – (3.64) as,

$$1+\frac{1}{4}K^{s*}\,\mathrm{Eo}\,\frac{Z_1^{s*}}{k^*}=0 \tag{3.70}$$

where Z_1^{s*} is given by,

$$\frac{Z_1^{s*}}{k^*}=\frac{2}{1+\alpha^s}\left[\frac{\left\{\frac{1}{1+\alpha^s}+\frac{G-1}{1+2\alpha^s}\right\}\left\{\left(1+\alpha^m\right)\left(1-V\right)-\left(1+V\right)\left(1+\alpha^m+\alpha^m G\right)\right\}}{\left(\frac{1+2\alpha^m}{1+2\alpha^s}G+\frac{1+\alpha^m}{1+\alpha^s}\right)\left(1-V\right)-\left(1+\alpha^m+\alpha^m G\right)\left(\frac{2\left(G-V\right)}{1+2\alpha^s}+\frac{1+V}{1+\alpha^s}\right)}-1\right] \tag{3.71}$$

One can see from the above set of equations that the marginal stability criterion at small current densities is independent of Ee and $C_{a,f0}$ and attained for Eo > 2.32, or G^s > 34 MPa for the set of parameter values mentioned earlier. At this critical separator modulus, the concentration of ambipolar diffusion on the tips is counter-balanced by the pressure driven flux away from the tips. Since ambipolar diffusion is independent of the fixed anions, the critical Eo value is independent of $C_{a,f0}$. The pressure driven flux also being proportional to J makes the criterion independent of Ee and J. The marginal stability is thus attained for a separator modulus of the same order as the osmotic pressure of the solution, which is much smaller than the modulus of the metal in most cases. It is hence useful to simplify equation (3.71) in the case of $G^m \gg G^s$, i.e. $G \gg 1$, which yields the marginal stability criterion as,

$$\mathrm{Eo} = \frac{G^s\left(\nu_c + \nu_{a,m}\right)}{RT} \approx \frac{3}{1-V}\frac{3-4\nu^s}{1+\nu^s} \tag{3.72}$$

The critical G^s or Eo value is sensitive to the partial molar volumes of both ions, as well as the separator Poisson ratio, as can be seen from Fig 3.11b. It is, however, independent of the electrode's modulus and Poisson ratio since the electrode is rigid compared to the separator and does not deform.

The marginal stability criterion at large current densities depends on all three parameters, viz. $C_{a,f0}$, Eo and Ee. In this regime, the pressure gradient driven flux is destabilizing in the migration region because of its role in the migration region where it increases the concentration of the fixed salt in high pressure locations. In the diffusion region, the pressure gradient driven flux is stabilizing as in the low current density case. This makes the nature of its total effect dependent on the size of the migration region l^* as seen in the last term in (3.60), which varies as $k^* \exp\left(-2k^*l^*\right)$. In other words, the destabilizing role of pressure-driven flux in the finite sized migration region is important for modes of wavenumber of the order of $1/l^*$, and attenuated when $k^*l^* << 1$. As we move toward higher k^* values, i.e. $k^*l^* \geq 1$, the role of migration region becomes more significant, and the stabilizing effect of pressure driven flux in the diffusion region diminishes. For large k^* values, stability is obtained from elasticity-slowed reaction at the tips. Under the critical conditions, the migration region is small enough that the destabilizing contribution of the pressure-driven flux component and the concentration of electric field driven flux on tips is counter-balanced by the effect of elasticity-slowed reaction kinetics and the stabilizing pressure driven flux in the diffusion region. For separator moduli higher than this limit

or current densities below it, the deposition is stable for all perturbation modes. As the elasticity-slowed reaction kinetics mechanism gains relative importance and the role of the finite size of migration region loses significance at higher k^* values, the marginal stability at high J occurs upon stabilization of a finite wavenumber $k_f^* = \mathrm{O}\left(1/l^*\right)$ perturbation which is the final mode to be stabilized. This argument suggests that under the critical conditions, the last mode to be stabilized is the most unstable mode and the critical mode at the same time. In other words,

$$k_f^* = k_{cr}^* = k_{mu}^* \tag{3.73}$$

Substituting this result in equations (3.60) – (3.63), we obtain the following expressions, which can be solved simultaneously to obtain the relation between $C_{a,f0}$, G^s and J for marginal stability.

$$1 - \frac{1}{2}\frac{Z_1^{s*}}{k_f^*} - \frac{1}{\mathrm{Ee}} K^{m*} C_{a,f0} Z_1^{m*} + \frac{1}{4}\left(2 + K^{s*}\,\mathrm{Eo}\right)\frac{Z_1^{s*}}{k_f^*}\exp\left(-2k_f^* l^*\right) = 0 \tag{3.74}$$

$$\frac{1}{\mathrm{Ee}} K^{m*} C_{a,f0} Z_1^{m*} + \frac{1}{2} l^* \left(2 + K^{s*}\,\mathrm{Eo}\right) Z_1^{s*} \exp\left(-2k_f^* l^*\right) = 0 \tag{3.75}$$

$$\frac{Z_1^{m*}}{k_f^* G} = \frac{2(1-V)\left[\dfrac{1}{1+\alpha^s} - \dfrac{1-G}{1+2\alpha^s}\right]}{\left(\dfrac{1+2\alpha^m}{1+2\alpha^s}G + \dfrac{1+\alpha^m}{1+\alpha^s}\right)(1-V) - \left(1+\alpha^m+\alpha^m G\right)\left(\dfrac{2(G-V)}{1+2\alpha^s} + \dfrac{1+V}{1+\alpha^s}\right)} \tag{3.76}$$

$$\frac{Z_1^{s*}}{k_f^*} = \frac{2}{1+\alpha^s}\left[\frac{\left\{\dfrac{1}{1+\alpha^s} - \dfrac{1-G}{1+2\alpha^s}\right\}\left\{\left(1+\alpha^m\right)(1-V) - (1+V)\left(1+\alpha^m+\alpha^m G\right)\right\}}{\left(\dfrac{1+2\alpha^m}{1+2\alpha^s}G + \dfrac{1+\alpha^m}{1+\alpha^s}\right)(1-V) - \left(1+\alpha^m+\alpha^m G\right)\left(\dfrac{2(G-V)}{1+2\alpha^s} + \dfrac{1+V}{1+\alpha^s}\right)} - 1\right] \tag{3.77}$$

The marginal stability result is shown in Fig 3.11a, where the deposition is fully stable for conditions to the right of a curve. We plot Ee·Eo on the *y*-axis to make

it independent of separator modulus, while Eo is shown on the *x*-axis to make it dependent on separator modulus. At low current densities, we obtain that the criterion of marginal stability is independent of $C_{a,f0}$ and Ee·Eo, and is given by a fixed value of Eo. At high current densities, we see that the marginal stability depends the three parameters – $C_{a,f0}$, Eo and Ee – that shows that improving the separator modulus (Eo) or fraction of fixed anions ($C_{a,f0}$) can increase the range of stable current densities (Ee·Eo). Conversely, we can attain stability by reducing the value of Ee·Eo, which can be done either by reducing the current density or improving the cation diffusivity. For the set of values in Table 3.2 with $C_{a,f0}$ = 0.1, G^s = 180 MPa, D_c = 10^{-9} cm^2/s and C_0 = 1M, we predict that current densities J < 0.38 mA/cm^2 should experience stable deposition.

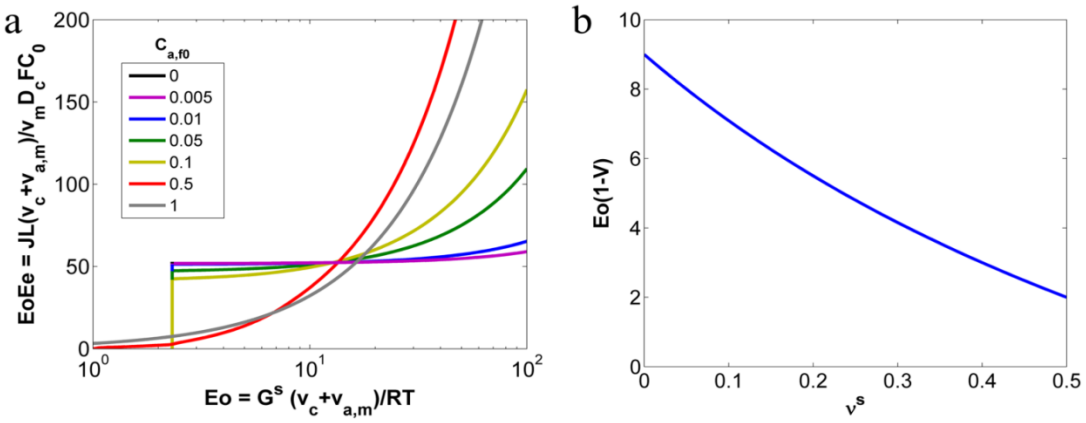

Figure 3.11: Marginal stability curves – Relation between separator modulus and current density at varying fixed anion fractions for which the deposition is stable for all modes. The deposition is fully stable at any point to the right of the corresponding curve.

3.4 Conclusions

We have shown through a linear stability analysis that morphological instabilities in electrodeposition can be suppressed through the use of solid electrolytes/separators with immobilized anions. Contrary to the popular notion in the literature that dendrite suppression requires electrolyte moduli comparable to that of the metal [4,21], our analysis reveals that the improvement in stability for electrodeposition of lithium can be achieved even for modest separator moduli of tens to hundreds of megapascals, which may be attainable even by polymer separators. This finding is shown to arise from consideration in the present analysis of the transport-driven growth of electrode surface perturbations that are suppressed by the elasticity.

Additionally, we incorporate the stabilizing role of the pressure gradient in driving the mobile ions in the inter-electrode space through a chemical potential gradient. This mechanism is shown to stabilize all modes of deposition even for separator moduli much lower than that of the metal electrode. It provides a qualitative explanation for several recent experimental observations [9-13] where stabilization of lithium metal electrodes is achieved at moderate separator moduli.

At current densities above the diffusion limit, the critical modulus for stability is reduced by increasing the fraction of immobilized anions or by reducing the applied current density. This suggests that enhancing the efficiency of anion immobilization not only facilitates stable electrodeposition of a metal, but also facilitates deposition at higher current densities. For current densities below the diffusion limit, the critical

modulus for stability is independent of the fraction of immobilized anions and current density.

It is important to point out that the critical modulus, $G^s \sim RT\left[\left(1-{}^{v_c}\!/_{v_m}\right)\left(v_c+v_{a,m}\right)\right]^{-1}$ is sensitive to the partial molar volumes of the cation (Fig 3.12) and the mobile anion in the separator, as well as the partial molar volume of the metal, which means that it is unlikely to be a universal value even for electrodeposition of lithium at a fixed temperature. The form of G^s while easily understood – the term $1-{}^{v_c}\!/_{v_m}$ determines the magnitude of pressure gradient created by the deformation, while the part of $v_c+v_{a,m}$ gives its relative significance in the chemical potential, underscores the need for experimental studies that allow measurement of the ionic partial molar volumes in solid electrolytes.

Our analysis suggests several potential strategies to mitigate rough electrodeposition of metals using solid electrolytes/separators. Primary among these approaches are immobilization of a fraction of the anions in the electrolyte, increasing the separator modulus, and reducing the current density at which deposition occurs. In quantitative terms, we find that by immobilizing even 10% of anions or increasing the modulus of a polymer separator to tens or hundreds of megapascals via cross-linking and other strategies, can lead to significant improvements over conventional salt based, liquid electrolytes. All three strategies lead to significant improvement in the range of length scales over which the electrodeposition is stable. Qualitative support for these conclusions can be found in experimental studies [9-17,27]. Other strategies include enhancing the surface tension, as noted in our previous study [6].

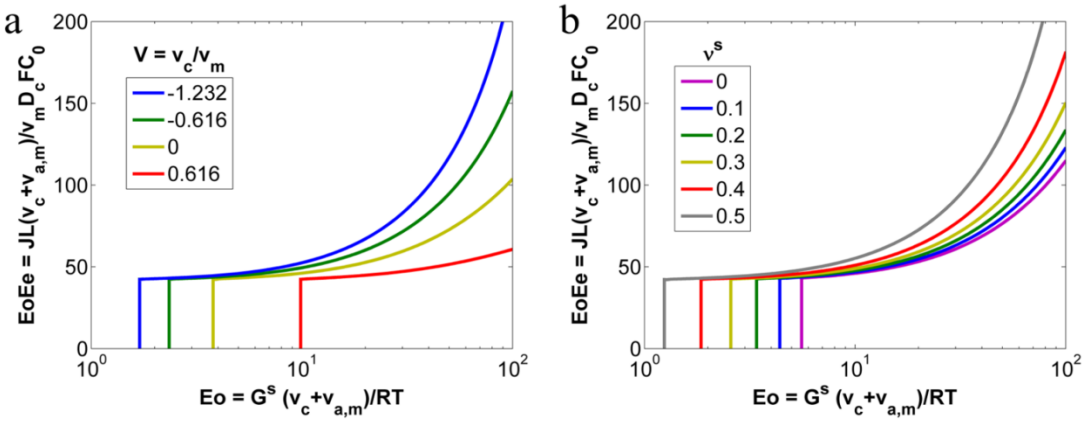

Figure 3.12: (a) Marginal stability curves for $C_{a,f0}$ = 0.1 and ν^s = 0.33 for various values of cation partial molar volume. The partial molar volumes of the mobile anion ($v_{a,m}$) and the metal (v_m) are held constant at 1.78×10^{-4} m^3/mol and 1.3×10^{-5} m^3/mol respectively. (b) Marginal stability for $C_{a,f0}$ = 0.1, v_c = -8×10^{-6} m^3/mol, $v_{a,m}$ = 1.78×10^{-4} m^3/mol, and v_m = 1.3×10^{-5} m^3/mol, for various values of separator Poisson ratio.

REFERENCES

1. Wijmans, J. G., and Baker, R. W., The solution-diffusion model: a review, *J. Membr. Sci.* **107**, 1-21 (1995)

2. Charles, R. J., Stress induced binary diffusion in a solid, *J. Electrochem. Soc.* **116 (11)**, 1514-1519 (1969)

3. Weber, N., and Goldstein, M., Stress-induced migration and partial molar volume of sodium ions in glass, *J. Chem. Phys.* **41 (9)**, 2898-2901 (1964)

4. Monroe, C., and Newman, J., The impact of elastic deformation on deposition kinetics at lithium/polymer interfaces, *J. Electrochem. Soc.* **152 (2)**, A396-A404 (2005)

5. Mani, A., and Bazant, M. Z., Deionization shocks in microstructures, *Phys. Rev. E* **84**, 061504 (2011)

6. Tikekar, M. D., Archer, L. A., and Koch, D. L., Stability analysis of electrodeposition across a structured electrolyte with immobilized anions, *J. Electrochem. Soc.* **161 (6)**, A847-A855 (2014)

7. Marcus, Y., and Hefter, G., Standard partial molar volumes of electrolytes and ions in nonaqueous solvents, *Chem. Rev.* **104**, 3405-3452 (2004)

8. It is important to note that the ensuing calculation requires a somewhat accurate knowledge of the partial molar volume of the cation and mobile anion which are difficult to know independently. We use the value reported by Marcus and Hefter (2004), who performed rigorous experiments with various salts to measure ionic partial molar volumes with a reference of a large ion's van der Waals volume, when no solvation effects are expected

9. Khurana, R., Schaefer, J. L., Archer, L. A. & Coates, G. W. Suppression of lithium dendrite growth using cross-linked polyethylene/poly(ethylene oxide) electrolytes: a new approach for practical lithium-metal polymer batteries. *J. Am. Chem. Soc.* **136**, 7395-7402 (2014)

10. Pan, Q., Smith, D. M., Qi, H., Wang, S. & Li, C. Y. Hybrid electrolytes with controlled network structures for lithium metal batteries. *Adv. Mater.* **27**, 5995-6001 (2015)

11. Ansari, Y., Guo, B., Cho, J. H., Park, K., Song, J., Ellison, C. J., and Goodenough, J. B., Low-cost, dendrite blocking polymer-Sb_2O_3 separators for lithium and sodium batteries, *J. Electrochem. Soc.* **161 (10)**, A1655-A1661 (2014)

12. Choudhury, S., Mangal, R., Agrawal, A., and Archer, L. A., A highly reversible room-temperature lithium metal battery based on crosslinked hairy nanoparticles, *Nat. Commun.* **6**, 10101 (2015)

13. Tung, S.-O., Ho, S., Yang, M., Zhang, R. & Kotov, N. A. A dendrite-suppressing composite ion conductor from aramid nanofibres, *Nat. Commun.* **6**, 6152 (2015)

14. Barton, J. L., and Bockris, J. O'M., The electrolytic growth of dendrites from ionic solutions, *Proc. R. Soc. Lond. A* **268**, 485-505 (1962)

15. Liu, S., Imanishi, N., Zhang, T., Hirano, A., Takeda, Y., Yamamoto, O., and Yang, J., Lithium dendrite formation in Li/Poly(ethylene oxide) – Lithium bis(trifluoromethanesufonyl)imide and N-methyl-N-propylpiperidinium bis(trifluoromethanesulfonyl)imide/Li cells, *J. Electrochem. Soc*. **157 (10)**, A1092-A1098 (2010)

16. Brissot, C., Rosso, M., Chazalviel, J.-N., and Lascaud, S., Dendritic growth mechanisms in lithium/polymer cells, *J. Power Sources* **81-82**, 925-929 (1999)

17. Osaka, T., Homma, T., Momma, T., and Yarimizu, H., In situ observation of lithium deposition processes in solid polymer and gel electrolytes, *J. Electroanal. Chem.* **421**, 153-156 (1997)

18. Song, J., Lee, H., Choo, M.-J., Park, J.-K., and Kim, H.-T., Ionomer-liquid electrolyte hybrid ionic conductor for high cycling stability of lithium metal electrodes, *Sci. Rep.* **5**, 14458 (2015)

19. Schaefer, J. L., Yanga, D. A., and Archer, L. A., High lithium transference number electrolytes via creation of 3-dimensional, charged, nanoporous networks from dense functionalized nanoparticle composites, *Chem. Mater.* **25 (6)**, 834-839 (2013)

20. Lu, Y., Tikekar, M., Mohanty, R., Hendrickson, K., Ma, L., and Archer, L. A., Stable cycling of lithium metal batteries using high lithium transference number electrolytes, *Adv. Energy Mater*. **5**, 1402073 (2015)

21. Stone, G. M., et al. Resolution of the modulus versus adhesion dilemma in solid polymer electrolytes for lithium metal batteries, *J. Electrochem. Soc.* **159**, A222-A227 (2012)

22. McKinley, G. H., Dimensionless groups for understanding free surface flows of complex fluids, *Soc. Rheol. Bull. 2005*, 6-9 (2005)

23. Style, R. W., Wettlaufer, J. S., and Dufresne, E. R., Surface tension and the mechanics of liquid inclusions in compliant solids, *Soft Matter* **11**, 672-679 (2015)

24. Style, R. W., Hyland, C., Boltyanskiy, R., Wettlaufer, J. S., and Dufresne, E. R., Surface tension and contact with soft elastic solids, *Nat. Commun.* **4**, 2728 (2013)

25. Bond, W. N., The surface tension of a moving water sheet, *Proc. Phys. Soc.* **47**, 549-558 (1935)

26. Hager, W. H., Wilfrid Noel Bond and the Bond number, *J. Hydraulics Res.* **50**, 3-9 (2012)

27. Tu, Z., Kambe, Y., Lu, Y., and Archer, L. A., Nanoporous Polymer-Ceramic Composite Electrolytes for Lithium Metal Batteries, *Adv. Energy Mater.*, **4**, 1300654 (2014)

CHAPTER 4

DIFFUSION OF IONS IN AND ELASTICITY OF INTERFACIAL LAYER

In the previous two sections, we have seen the benefits of using electrolytes with immobilized charges and elastic solid separators in suppressing dendrite growth. While both of these options provide stable deposition and have been widely deployed in experimental works, liquid electrolytes continue to remain popular due to their scalability to larger systems, high ionic conductivity, and low cost.

Recent research has attempted to control dendrite growth in liquid electrolytes by modifying the metal-electrolyte interface using additives in the electrolyte or coating the surface with thin polymer layers. This is of particular interest for highly reactive metals which react with the electrolyte to form insulating passivation layers. The interfacial films serve to reduce electrolyte decomposition as well as control the transport of ions and deposition at the surface to suppress the morphological instability. Using additives to stabilize electrodeposition was also the preferred method for electrodeposition of transition metals, because of the simplicity of its execution as well as its effectiveness. While experimental evidence for the effectiveness of such techniques has been abundant, the theoretical effort in this area has been lacking, rendering the process of discovery of such techniques somewhat empirical. The key roadblock to understanding the role of interfacial effects in electrodeposition is that the exact nature, composition and behavior of the interfacial layer are unknown and mostly speculative. However, there is consensus, in general, on the idea that the stability of electrodeposition is significantly influenced by the interfacial layer.

Joint Density Functional Theory calculations [1] show that a LiF-rich interfacial layer allows for lateral diffusion of Li^+ ions, which can weaken the instability significantly, compared to the Li_2CO_3 and LiO_2 films that usually form on the Li surface due to its reaction with the electrolyte. This idea has been employed in studies which use LiF as an additive in the electrolyte which then migrates to the Li surface [2] or directly coating LiF on the Li surface [3]. Some studies have used salts and additives that react with the surface to produce LiF films on the metal surface.

Other studies attempting to protect the lithium metal surface from reacting with the electrolyte are employ ion conducting polymer-based membranes. One hypothesis is that elasticity of the interfacial layer resists deformation of the surface [4] similar to the effect of using an elastic solid electrolyte. This has fueled efforts to design highly elastic and non-brittle artificial films that are applied on to the Li surface [5,6]. These two speculations, thus, open up the possibility of stabilizing deposition by controlling the transport and elastic properties of the interfacial layer. However, there are no theoretical models in the literature that capture these effects.

While the analysis of the preceding sections uses a phenomenological description of the interface in the form of surface tension, the explicit behavior of interfacial mechanisms is not included therein. To that effect, we try to incorporate interfacial transport mechanisms and elasticity into our description for electrodeposition in that order. The interfacial films (10-100nm) are typically smaller than the sizes of dendrites (~0.1-1μm) formed, which indicates that the perturbation will not decay significantly across the layer. This allows us to assume that the interfacial layer may be included as an appropriate boundary condition for the

transport equations without explicitly analyzing transport through the layer. For the present case, we ignore the fixed anions and look at these effects in a binary salt solution of monovalent ions. We first modify our standard picture of the deposition process to include the interfacial layer, followed by testing the stability of the deposition. More explicitly, we seek a description of the surface tension used in the previous sections that includes the transport in and elasticity of the interfacial layer.

4.1 Interfacial diffusion

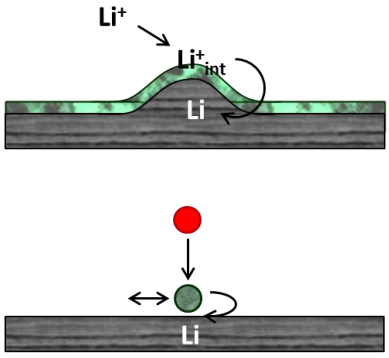

Figure 4.1: A schematic illustration of the two-step process model

To include the diffusion in the interfacial layer, we consider a two-step process in the deposition reaction (Figure 4.1). In the first step, lithium ions in the bulk electrolyte attach onto the surface layer, to form an interfacial species with surface concentration θ. We model this step as a process with fast kinetics with equilibrium constant β. The interfacial ions are free to diffuse along the surface with diffusivity D_s. In the following step, the interfacial ions are reduced to their metallic form by picking up an electron from the metal, which thus, grows the metal. We model this step using

Butler-Volmer reaction kinetics. This can, thus, be written as follows.

i. The adsorption reaction, $\mathrm{Li}^{+} \rightleftharpoons \mathrm{Li}^{+}_{\mathrm{int}}$, satisfies the equilibrium condition,

$$\beta C_c\big|_{z=0} = \theta \tag{4.1}$$

ii. The adsorbed ions reduce into the metal with Butler-Volmer kinetics as,

$$J_{rxn} = R_0 \left(C_c\big|_{z=0}\right)^{1-\alpha} \left[\exp\left((1-\alpha)\frac{\psi_s}{RT}\right) - \exp\left(-\alpha\frac{\psi_s}{RT}\right)\right] \tag{4.2}$$

where, ψ_s is the excess chemical potential at the surface defined as,

$$\psi_s = \left(\psi^{\ominus}_{ads} + RT\ln\frac{\theta}{1-\theta} + F\phi\right) - \left(\psi^{\ominus}_{m} + \gamma v_m \mathrm{K}\right), \tag{4.3}$$

R_0 is the reaction rate constant, α is the reaction symmetry factor, Γ_s is the saturation surface concentration and $\nabla_s = (\mathbf{I} - \mathbf{nn})\cdot\nabla$ is the surface gradient operator.

The interfacial ions diffuse along the surface with a flux,

$$\mathbf{J}_{sd} = -D_s \Gamma_s \nabla_s \theta \tag{4.4}$$

Additionally, conservation of ions at the surface yields,

$$J_{rxn} + \nabla_s \cdot \mathbf{J}_{sd} = J \tag{4.5}$$

The growth of the surface is through the reaction, which can be written as,

$$\frac{\partial H_c}{\partial t} = \frac{v_m}{F} J_{rxn} \tag{4.6}$$

The governing equations for cation and anion transport are the same as before,

$$\nabla^2 C_c + \frac{F}{RT}\nabla\cdot\left(C_c\nabla\phi\right) = 0 \tag{4.7}$$

$$\nabla^2 C_a - \frac{F}{RT}\nabla\cdot\left(C_a\nabla\phi\right) = 0 \tag{4.8}$$

The above system of equations can be solved to obtain concentration profiles

for two flat, parallel electrodes. We simplify the algebra with the assumption $\psi_s/RT \ll 1$ which linearizes the Butler-Volmer kinetics as $J_{rxn} = R_0 \left(C_c\big|_{z=0} \right)^{1-\alpha} \psi_s/RT$. The implies that the applied current density is smaller than the reaction exchange current, and the system has small deviation from fast kinetics.

$$C_c = C_a = C_0 \left(1 - \frac{JL}{4D_c F C_0} \right) + \frac{Jz}{2D_c F C_0} \tag{4.9}$$

$$\theta = \beta C_0 \left(1 - \frac{JL}{4D_c F C_0} \right) \tag{4.10}$$

4.1.1 Linear stability

We next study the linear stability of the system by perturbing it sinusoidally with arbitrarily small amplitude ε and known wavenumber k and evaluating the growth of the perturbation over time. The electrode surface [$\tilde{H}_c = H_c + \varepsilon e^{\sigma t} e^{ikx}$], concentration [$\tilde{C}_c = C_c + \varepsilon C_c'(z) e^{\sigma t} e^{ikx}$], potential [$\tilde{\phi} = \phi + \varepsilon \phi'(z) e^{\sigma t} e^{ikx}$] and current density [$\tilde{\mathbf{J}} = \mathbf{J} + \varepsilon \mathbf{J}'(z) e^{\sigma t} e^{ikx}$] as well as the surface coverage [$\tilde{\theta} = \theta + \varepsilon \theta' e^{\sigma t} e^{ikx}$] are perturbed this way. This gives,

$$\frac{d^2 C_c'}{dz^2} - k^2 C_c' = 0 \tag{4.11}$$

The boundary conditions are also perturbed in the same fashion. Perturbation to the equilibrium equation gives,

$$\beta \left[C_c'\Big|_{z=0} + \frac{dC_c}{dz}\bigg|_{z=0} \right] = \theta' \tag{4.12}$$

$$J'_{rxn} + D_s \Gamma_s k^2 \theta' = J' \tag{4.13}$$

$$J'_{rxn} = \frac{F}{\nu_m}\sigma = (1-\alpha)\frac{J}{C_c|_0}\left(C'_c|_0 + \left.\frac{dC_c}{dz}\right|_0\right) - R_0\left(C_c|_0\right)^{1-\alpha}\frac{\psi'_s}{RT} \tag{4.14}$$

$$\psi'_s = RT\frac{\theta'}{\theta} + F\left(\phi'|_0 + \left.\frac{d\phi}{dz}\right|_0\right) - \gamma\nu_m k^2 \tag{4.15}$$

Solving the above set of equations yields the growth rate of the perturbation as,

$$\sigma = \nu_m \frac{kJ - \gamma\nu_m \frac{D_c F}{RT}\frac{\mathrm{Da}}{\mathrm{Da}+1-\alpha}C_c|_0 k^3(1+\mathrm{Ld}\,kL)}{1+\frac{2}{\mathrm{Da}+1-\alpha}\frac{D_c F\, C_c|_0}{J}k(1+\mathrm{Ld}\,kL)} \tag{4.16}$$

where Da is the Damkohler number defined as,

$$\mathrm{Da} = \frac{2R_0\left(C_c|_0\right)^{1-\alpha}}{J} \tag{4.17}$$

Ld is a form of Dukhin number, comparing the surface conductivity of the interfacial layer to the bulk conductivity of the solution. We refer to it as the Langmuir-Dukhin number and it is defined as,

$$\mathrm{Ld} = \frac{D_s \Gamma_s \beta}{2D_c L} \tag{4.18}$$

The result suggests that the surface tension promotes dissolution of tips to ions, which are then redistributed through a combination of bulk and interfacial diffusion along the metal surface. We may, thus, say that the effective surface tension at this interface can be given by,

$$\gamma_{eff} = \gamma\frac{\mathrm{Da}}{\mathrm{Da}+1-\alpha}(1+\mathrm{Ld}\,kL) \tag{4.19}$$

which, notably, is length-scale dependent. The higher order in k for the surface

diffusion term, i.e. k^4, suggests that surface diffusion is important higher values of k, although that exact range of transition depends on the value of the Langmuir-Dukhin number.

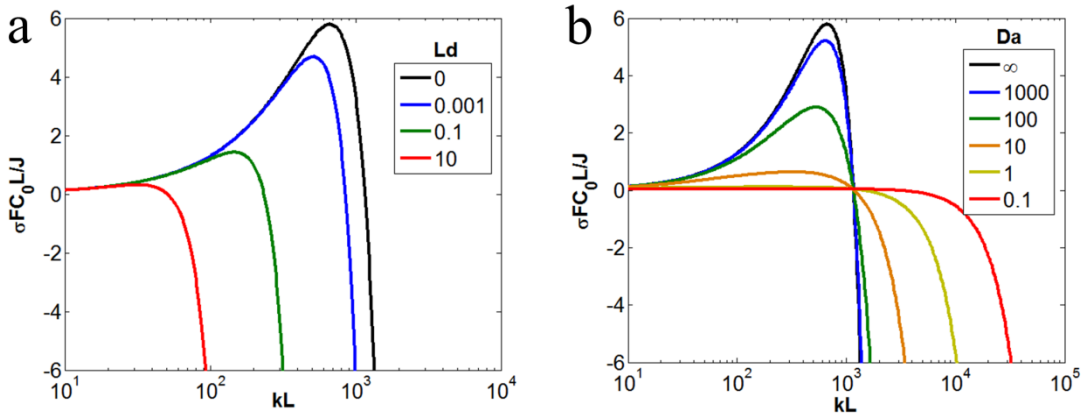

Figure 4.2: Perturbation growth rate versus wavenumber for (a) infinite Da and varying Ld and (b) zero Ld and varying Da

The role of interfacial kinetics can also be seen from the above result. For fast kinetics, i.e. $\mathrm{Da} \to \infty$, we recover the result of the previous sections, where the stability is directly the difference between the current density induced deposit growth and the surface tension induced tip dissolution. At small and finite Da, the relative contributions of the two driving forces are weighted by their respective charge transfer coefficients and the growth of the tip is scaled by the reaction rate itself, viz. the Damkohler number.

Both of these results are evident in Figure 4.2. In Figure 4.2a, for fast reaction kinetics, we see that increasing the surface diffusion relative to the bulk diffusion improves the stability of deposition. Significantly, even a relatively small value of Ld

~ 10^{-3} reduces the instability compared to no surface diffusion. From Figure 4.2b which shows the effect of varying reaction kinetics without any surface diffusion, we see that slower reaction kinetics (i.e. reduced Da) leads to a wider range of unstable modes but a slower growth of those modes. This is in agreement with several other studies, particularly nonlinear simulations, which have found that slower interfacial kinetics suppresses dendritic growth.

4.2 Interfacial layer elasticity

The effect of elasticity on the phenomenologically written surface tension is easy to evaluate. The thickness of the interfacial layer (10-100nm) is typically smaller than the dendrites (~0.1-1μm). The deformation of interfacial layer is thus constant along its thickness. The deformation and strain fields in the interfacial layer can, then, be written as,

$$\mathbf{u} = V(x)\hat{\mathbf{x}} + U(x)\hat{\mathbf{z}} \tag{4.20}$$

$$\boldsymbol{\sigma} = \frac{2\nu G}{1-2\nu}(\mathbf{I}:\boldsymbol{\varepsilon})\mathbf{I} + 2G\boldsymbol{\varepsilon} \tag{4.21}$$

$$\boldsymbol{\varepsilon} = \frac{1}{2}\left[\nabla\mathbf{u} + (\nabla\mathbf{u})^{\dagger}\right] \tag{4.22}$$

The free energy of the interfacial layer W is written in terms of its surface energy and the elastic energy of the deformed layer. This, in turn, gives the contribution of the layer to the chemical potential of the metal, which is evaluated by the change in W due to an increase δn_m in the number of atoms in the metal.

$$W = \gamma A + \int_{V_{layer}} \frac{1}{2}(\boldsymbol{\sigma}:\boldsymbol{\varepsilon})\,dV \tag{4.23}$$

$$\psi_m^{layer} = \frac{\delta W}{\delta n_m} \tag{4.24}$$

Using the deformation field above, we obtain,

$$\gamma_{eff} = \gamma + Gh \tag{4.25}$$

Thus, the effective interfacial energy is depends on shear modulus of the interfacial layer. This is because, for small deposits, the deformation of the interfacial layer is in shear mode (Fig 4.3).

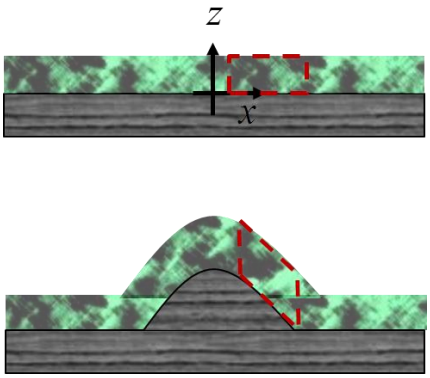

Figure 4.3: Shear mode deformation of the interfacial layer for small deposits can be seen from the change in the shape of the dashed square

4.3 Conclusions

In this chapter, we have attempted to model the behavior of the interfacial layer based on two speculated roles played by it. The results indicate that improving lateral transport in the interfacial layer or weakening surface kinetics can significantly reduce the instability of deposition, both of which confirm existing notions in the literature. We also determined that elasticity of the interfacial layer modifies the surface tension as shear modulus times the thickness of the layer, which suggests that

using a thin elastic layer on the surface can improve the stability of deposition.

REFERENCES

1. Ozhabes, Y., Gunceler, D., Arias, T. A. Stability and surface diffusion at lithium-electrolyte interphases with connections to dendrite suppression. Preprint at http://arxiv.org/abs/1504.05799 (2015)

2. Lu, Y., Tu, Z. & Archer, L. A. Stable lithium electrodeposition in liquid and nanoporous solid electrolytes. *Nat. Mater.* **13**, 961-969 (2014)

3. Choudhury, S. & Archer, L. A. Lithium fluoride additives for stable cycling of lithium batteries at high current densities. *Adv. Electron. Mater.* **2**, 1500246 (2016)

4. Aurbach, D., Zinigrad, E., Cohen, Y. & Teller, H. A short review of failure mechanisms of lithium metal and lithiated graphite anodes in liquid electrolyte solutions. *Solid State Ionics* **148**, 405–416 (2002)

5. Choudhury, S., Mangal, R., Agrawal, A., and Archer L. A. A highly reversible room-temperature lithium metal battery based on crosslinked hairy nanoparticles, *Nat. Commun.* **6**, 10101 (2015)

6. Zheng, G., et al. Interconnected hollow carbon nanospheres for stable lithium metal anodes. *Nat. Nanotech.* **9**, 618-623 (2014)

CHAPTER 5

ELECTROCONVECTION WITH POLYMER ADDITIVES

As mentioned in the previous chapter, liquid electrolytes continue to remain popular in electrodeposition and battery applications because of their low cost, high ionic conductivity and scalability. Liquid systems, however, tend to undergo convection due to electroosmotic flow driven by the electric field causing the deposition. This is termed electroconvection, and can lead to significantly unstable deposition, particularly at high current densities where the electroconvection is strong. Previous experimental studies have shown that the electroconvection typically sets the length scale of the morphological deposits at high current densities, which in turn, can modulate the electroconvection giving a coupled effect with very fast instability growth. Having learnt from Chapter 3 that the electrolyte rheology can profoundly influence the instability, we apply the same idea here.

We now evaluate the role of electroconvection in the deposition process in the presence of high molecular weight polyelectrolyte additives in the electrolyte. Polyelectrolytes are charged polymers, with useful applications in electrodeposition and batteries due to their ion conductive properties and electrochemical stability. As we have seen previously, having immobile charges in the electrolyte is useful in stabilizing the deposition by modifying the charge transport to the metal surface. In this section, we look for the possibility to modify the transport by tuning the convection in the electrolyte. Four possible effects of introducing the polymer additives are postulated. i. The viscoelasticity of the polymer may modify the

convection of the electrolyte by introducing secondary flows caused by the polymer stretch. ii. Concentration variations in the polymer driven by relative motion between the polymer and fluid and electrophoresis of the polymer can displace the fluid, thus affecting ion transport to the electrode. iii. Concentration fluctuations in the polymer may induce osmotic stress variations that can modify the fluid flow. iv. The relative motion between the polymer and fluid may cause the polymer to exert drag on the fluid, damping the convection. We will, hence, first look at a model that is capable of capturing such a large number of physical effects.

5.1 The two-fluid model and transport equations

Conventional viscoelastic mixture models are insufficient at describing electrodeposition across electrolytes with polyelectrolyte additives. This is mainly because electroconvection is driven at the metal surface by the dissolved ions that are predominantly in the fluid phase. This gives macroscopic relative motion between the more viscous polymer and fluid, leading to concentration variations in the polymer which cannot be captured in a single constitutive law. Thus, evaluating the effect of high molecular weight polyelectrolyte additives requires a two-fluid model which can describe the convective-diffusive behavior of a bicontinuous mixture of two fluids where the motion of the fluids is coupled with a relative drag and the thermodynamic forces of mixing. One way to do this is to use a model developed by Doi and Onuki [1], and elaborated further by Fredrickson and coworkers [2-4], in the study of shear banding of entangled polymer solutions. In doing so, we will assume that the concentration of the added salt is significantly higher than the charge density of the polymer, and that

the charges on the polymer are sufficiently screened from each other by the added salt. This allows us to assume that the polymer adopts a configuration identical to that of an uncharged polymer, which has well-known scaling relations for various rheological properties. The presence of charges along the polymer backbone may induce an electroosmotic flow in the solvent, which also modify the derivation from the previous studies to a small extent.

The Doi-Onuki [1] two-fluid model is based on the variational approach of Onsager [5], which is established as a corollary to the reciprocal relations. The principle states that for non-equilibrium non-inertial systems, the motion of the system is such that it minimizes energy dissipation under given driving forces. This means that, we can define an energy functional called the Rayleighian, which contains information about dissipation within the two-fluid system due to flows of the two phases, and the energy dissipated by the external and internal forces of the system. The Rayleighian R can, then, we written as the sum of viscous dissipation functional W and the time rate of change of reversible energy of the system $\dot{H}$, subject to the restriction that the system as a whole is incompressible.

The viscous dissipation functional W can be written in terms of the dissipation due to relative motion between the polymer and fluid and dissipation within the fluid. For dilute polyelectrolyte solutions, this gives,

$$W = \int d\mathbf{r} \left\{ \frac{1}{2} \zeta_{PF}(\phi) \left| \mathbf{u}_P - \mathbf{u}_F + \frac{\Lambda}{\eta_F} \nabla \Phi \right|^2 + \eta_F \left[\nabla \mathbf{u}_F + (\nabla \mathbf{u}_F)^\dagger \right] : \nabla \mathbf{u}_F \right\} \qquad (5.1)$$

where $\mathbf{u}_P$ and $\mathbf{u}_F$ are velocities of the polymer and fluid respectively, η_F is the fluid viscosity, Λ is the charge per unit length on the polymer, and ζ_{PF} is the polymer

volume fraction-dependent coupling/drag coefficient between the fluid and polymer relative motion. In the above expression, we have allowed for an electroosmotic slip of the fluid relative to the polymer due to dissociable charges on the polymer. The drag coefficient can be estimated from the solution correlation length as $\zeta_{PF}(\phi) = \eta_F / \xi^2$.

The reversible energy of the system H can, in general, depend on the polymer volume fraction ϕ and configuration $\mathbf{Q}$ defined in terms of the ensemble-averaged end-to-end vector $\mathbf{r}_P$ and its equilibrium magnitude r_{P0} as $\mathbf{Q} = \langle \mathbf{r}_P \mathbf{r}_P \rangle / r_{P0}^2$. The time rate of the reversible energy, then, is given by,

$$\frac{\partial}{\partial t} H(\phi, \mathbf{Q}) = \dot{H} = \int d\mathbf{r} \left[\frac{\delta H}{\delta \phi} \frac{\partial \phi}{\partial t} + \frac{\delta H}{\delta \mathbf{Q}} : \frac{\partial \mathbf{Q}}{\partial t} \right] \tag{5.2}$$

where, $\delta H/\delta\phi$ and $\delta H/\delta\mathbf{Q}$ are functional derivatives defined as,

$$\frac{\delta H}{\delta \phi} = \frac{\delta}{\delta \phi} \int h(\phi, \mathbf{Q}) d\mathbf{r} = \frac{\partial h}{\partial \phi} - \nabla \cdot \frac{\partial h}{\partial \nabla \phi} \tag{5.3}$$

$$\frac{\delta H}{\delta \mathbf{Q}} = \frac{\delta}{\delta \mathbf{Q}} \int h(\phi, \mathbf{Q}) d\mathbf{r} = \frac{\partial h}{\partial \mathbf{Q}} - \nabla \cdot \frac{\partial h}{\partial \nabla \mathbf{Q}} \tag{5.4}$$

The time-rate of change of the polymer volume fraction ϕ and conformation $\mathbf{Q}$ are given by their respective conservation equations, which are written in terms of the polymer velocity $\mathbf{u}_P$. Since H is the reversible component of the free energy, we only consider the flow-reversible part of the conservation of $\mathbf{Q}$ and neglect irreversible processes like reptation, constraint release and chain retraction within the tube, all of which dissipate energy into the fluid. This does not mean that the dissipative processes are negligible in general, since they affect the evolution of $\mathbf{Q}$ itself, but it means that they have no contribution to reversible energy of the system. This gives,

$$\frac{\partial \phi}{\partial t} = -\nabla \cdot \left(\mathbf{u}_P \phi \right) \tag{5.5}$$

$$\frac{\partial \mathbf{Q}}{\partial t} = -\mathbf{u}_P \cdot \nabla \mathbf{Q} + \left(\nabla \mathbf{u}_P \right)^{\dagger} \cdot \mathbf{Q} + \mathbf{Q} \cdot \nabla \mathbf{u}_P \tag{5.6}$$

The Rayleighian is minimized with a Lagrange multiplier term to address incompressibility. Thus, the functional to be minimized with respect to the velocity fields is $R_M = W + \dot{H} - L$, where $L = \int \ell \cdot d\mathbf{r} = \int d\mathbf{r} p \nabla \cdot \left[\mathbf{u}_P \phi + \mathbf{u}_F \left(1 - \phi \right) \right]$. This gives $\delta R_M / \delta \mathbf{u}_P = 0$ and $\delta R_M / \delta \mathbf{u}_F = 0$, which yield,

$$-\phi \nabla p - \zeta_{PF} \left(\mathbf{u}_P - \mathbf{u}_F + \frac{\Lambda}{\eta_F} \nabla \Phi \right) - \phi \nabla \frac{\delta H}{\delta \phi} + \nabla \mathbf{Q} : \frac{\delta H}{\delta \mathbf{Q}} + \nabla \cdot \left[2\mathbf{Q} \cdot \frac{\delta H}{\delta \mathbf{Q}} \right] = 0 \tag{5.7}$$

$$-\left(1 - \phi \right) \nabla p + \zeta_{PF} \left(\mathbf{u}_P - \mathbf{u}_F + \frac{\Lambda}{\eta_F} \nabla \Phi \right) + \eta_F \nabla^2 \mathbf{u}_F = 0 \tag{5.8}$$

The above equations provide the most general form of the polymer-solvent two-fluid model, given a description for the free energy landscape.

This only leaves us to choose an appropriate form for the free energy functional *H*. Following Peterson et al, we use the following form,

$$H = \int d\mathbf{r} \left\{ \frac{1}{2} \chi_0^{-1} \phi^2 + \frac{1}{2} G(\phi) \left[\mathrm{Tr}\left(\mathbf{Q} \right) - 3 - \log \det \left(\mathbf{Q} \right) \right] \right\} \tag{5.9}$$

The first term in the above integrand refers to the free energy of mixing of the polymer and fluid where χ_0^{-1} is called the osmotic susceptibility of the mixture and can be obtained from the Flory-Huggins solution theory. The second term is the elastic energy of the polymer as defined by Flory [6]. The main difference between the above momentum equations and those obtained by Peterson et al [4] is the presence of the electroosmotic slip of the fluid relative to the polymer in the drag term because the

polymers in the present case are charged. A less significant difference is that we have omitted the dependence of the free energy of mixing on the gradient of polymer volume fraction which adds a term as $\chi_0^{-1}\xi^2|\nabla\phi|^2/2$ to the integrand. This is because we do not expect sharp polymer concentration variations in the present case that are characteristic of the shear banding problem studied by Peterson et al [4].

In the limit of small polymer volume fraction, $\phi \ll 1$, the equations mass and momentum equations for the polymer and fluid are,

$$\nabla\cdot\left(\phi\mathbf{u}_P\right)=\nabla\cdot\mathbf{u}_F=0 \tag{5.10}$$

$$-\nabla\cdot\boldsymbol{\Pi}-\frac{\eta_F}{\xi^2}\left(\mathbf{u}_P-\mathbf{u}_F+\frac{\Lambda}{\eta_F}\nabla\Phi\right)+\nabla\cdot\left[G\left(\mathbf{Q}-\mathbf{I}\right)\right]=0 \tag{5.11}$$

$$-\nabla p+\frac{\eta_F}{\xi^2}\left(\mathbf{u}_P-\mathbf{u}_F+\frac{\Lambda}{\eta_F}\nabla\Phi\right)+\eta_F\nabla^2\mathbf{u}_F=0 \tag{5.12}$$

where the osmotic force $\nabla\cdot\boldsymbol{\Pi}$ is related to the polymer volume fraction ϕ and conformation tensor $\mathbf{Q}$ by,

$$\nabla\cdot\boldsymbol{\Pi}=\chi_0^{-1}\phi\nabla\phi+\frac{1}{2}\phi\nabla\left\{\frac{dG}{d\phi}\left[\mathrm{Tr}\left(\mathbf{Q}\right)-3-\log\det\left(\mathbf{Q}\right)\right]\right\}-\frac{G}{2}\left[\nabla\left(\mathrm{Tr}\left(\mathbf{Q}\right)\right)-\nabla\mathbf{Q}:\mathbf{Q}^{-1}\right] \tag{5.13}$$

The polymer conformation tensor $\mathbf{Q}$ evolves with the flow according to the Rolie-Poly equation [7],

$$\frac{\partial\mathbf{Q}}{\partial t}+\mathbf{u}_P\cdot\nabla\mathbf{Q}-\left(\nabla\mathbf{u}_P\right)^{\dagger}\cdot\mathbf{Q}-\mathbf{Q}\cdot\nabla\mathbf{u}_P=-\frac{\mathbf{Q}-\mathbf{I}}{\tau_D}-\frac{2}{\tau_R}\left(1-\sqrt{\frac{3}{\mathrm{Tr}\left(\mathbf{Q}\right)}}\right)\left[\mathbf{Q}+\sqrt{\frac{3}{\mathrm{Tr}\left(\mathbf{Q}\right)}}\left(\mathbf{Q}-\mathbf{I}\right)\right] \tag{5.14}$$

τ_D is the reptation time which is the time taken by the polymer chain to diffuse its own length, while τ_R is the Rouse time, which is the time required by the polymer to escape the tube formed by its neighbors.

Scaling theory [8] predicts the following scalings for various parameters with polymer volume fraction ϕ and degree of polymerization N,

$$\xi = \xi_0 \phi^{-3/4} \qquad G = G_0 \phi^{9/4} \qquad \tau_D = 6\tau_0 \frac{N^3}{N_e(1)} \phi^{3/2} \qquad \tau_R = 2\tau_0 N^2 \phi^{1/4} \tag{5.15}$$

Here N_e (1) ≈ 20 is the number of Kuhn monomers in an entanglement strand of a polymer melt and ξ_0, G_0, τ_0 are material constants. ξ_0 is the correlation length in a polymer melt and is experimentally determined [13]. G_0 is the entanglement modulus of a polymer melt and gives the entropy density of an entanglement strand. τ_0 is the diffusive time scale of a single monomer.

The above set of equations can be simplified with the assumption that the degree of polymerization is much larger than the melt entanglement strand $N \gg N_e(1)$. This gives $\tau_D \gg \tau_R$. Additionally, the osmotic susceptibility χ_0^{-1} may be estimated using Flory-Huggins solution theory as,

$$\chi_0^{-1} = \frac{RT}{V_F}(1-2\chi) \tag{5.16}$$

where χ is the Flory-Huggins interaction parameter and V_F is the fluid molar volume. The charge per unit length of the polyelectrolyte Λ can also be estimated from the number of monomers n per charge group of valence z_P using the Kuhn monomer size b_0 and Avogadro's constant $\tilde{N}_{av}$.

$$\Lambda = \frac{z_P F}{n b_0 \tilde{N}_{av}} \tag{5.17}$$

Furthermore, the cation and anion transport equations may be written as,

$$\nabla \cdot (\mathbf{u}_F C_c) = D_c \nabla^2 C_c + \frac{D_c F}{RT} \nabla \cdot (C_c \nabla \Phi) \tag{5.18}$$

$$\nabla \cdot \left(\mathbf{u}_F C_a \right) = D_a \nabla^2 C_a - \frac{D_a F}{RT} \nabla \cdot \left(C_a \nabla \Phi \right) \tag{5.19}$$

with the local electroneutrality constraint being expressed as,

$$C_a = C_c + \Lambda \phi \frac{3}{4\pi b_0^2 F} \tag{5.20}$$

The boundary conditions are given by impenetrability of the both surfaces to the polymer and fluid with Navier slip for the polymer and electroosmotic slip of the fluid at the two electrodes. The potentials at the two electrodes also need to be specified. The polymer's Navier slip relates the slip velocity to the tangential component of the polymer's elastic stress through a slip coefficient β. A previous experimental work by Mhetar and Archer [9] gives the value of the slip coefficient for a range of high molecular weight polymers. For the electroosmotic slip of the fluid along the metal surface, we use a form developed by Rubinstein and Zaltzmann [10] that includes the effect of salt concentration variations along the metal surface. This form is obtained by assuming a quasi-equilibrium potential profile in the double layer, with lateral variations in the bulk ion concentrations captured as a variation in the Debye length. The quasi-equilibrium double layer potential profile is then used in the fluid momentum equation with an electrically-driven body force, which is then integrated over the double layer to obtain the slip velocity for the flow outside the double layer. As with the conventional Helmholtz-Smoluchowski slip, this slip velocity is parametrized with the zeta potential of the surface ζ, solvent permittivity ε and viscosity η_F. Thus, at both $z = 0$ and $z = L$, we have,

$$\mathbf{n} \cdot \mathbf{u}_F = \frac{\partial H}{\partial t} \qquad \mathbf{n} \cdot \mathbf{u}_P = \frac{\partial H}{\partial t} \qquad \left(\mathbf{I} - \mathbf{nn} \right) \cdot \mathbf{u}_P = \beta G \left(\mathbf{I} - \mathbf{nn} \right) \mathbf{n} : \left(\mathbf{Q} - \mathbf{I} \right)$$

$$(\mathbf{I}-\mathbf{nn})\cdot\mathbf{u}_F=\frac{\varepsilon}{\eta_F}(\mathbf{I}-\mathbf{nn})\cdot\left[\zeta\left(\nabla\Phi+\frac{RT}{F}\cdot\frac{\nabla C_c}{C_c}\right)+\left(\frac{RT}{F}\right)^2\ln 16\frac{\nabla C_c}{C_c}\right] \quad (5.21)$$

The boundary conditions on the transport equations are given by the cation transport driving the electrode growth and the electrode being impermeable to the anions. Also, the electric potential is specified at the two electrodes. This gives,

$$-\frac{J}{F}=\mathbf{n}\cdot\left[-D_c\nabla C_c-\frac{D_cF}{RT}C_c\nabla\Phi\right]=\frac{1}{v_m}\frac{\partial H}{\partial t} \quad 0=\mathbf{n}\cdot\left[-D_a\nabla C_a+\frac{D_aF}{RT}C_a\nabla\Phi\right]$$

$$\Phi(z=0)=0 \text{ and } \Phi(z=L)=V_0 \quad (5.22)$$

In addition, the cation and polymer are conserved to their equilibrium concentration values C_0 and ϕ_0 respectively.

$$\int_0^L C_c dz=C_0L \qquad \int_0^L \phi dz=\phi_0 L \quad (5.23)$$

5.2 Base state

The framework developed in the previous section is first solved for two parallel electrodes at z = 0 and z = L. The equations are then perturbed to test the linear stability of base state solutions.

Before we present the results, it is useful to nondimensionalize the equations. We choose the following non-dimensionalization scheme, $\mathbf{u}_F^*=\mathbf{u}_F FL\eta_F/\Lambda RT$, $\mathbf{u}_P^*=\mathbf{u}_P FLG_0/\Lambda RT\cdot 6\tau_0 N^3/N_e(1)$, $\Phi^*=F\Phi/RT$, $p^*=p/\chi_0^{-1}$, $\nabla\cdot\mathbf{\Pi}^*=\nabla\cdot\mathbf{\Pi}/\chi_0^{-1}$, $C_c^*=C_c/C_0$, $C_a^*=C_a/C_0$, $x^*=x/L$, $z^*=z/L$, $k^*=kL$, $J^*=JL/D_cFC_0$. In the non-dimensionalization process, we obtain the following set of nondimensional groups,

$$\mathrm{Ed} = \frac{F\xi_0^2\chi_0^{-1}}{RT\Lambda} \qquad \mathrm{Da} = \frac{\xi_0^2}{L^2} \qquad \eta = \frac{\eta_F}{G_0\tau_{D0}} \qquad \mathrm{Pe} = \frac{\Lambda RT}{F\eta_F D_c}$$

$$t_c = \frac{D_c}{D_c + D_a} \qquad \Lambda^* = \Lambda\frac{3}{4\pi b_0^2 F C_0} \tag{5.24}$$

Ed, loosely termed the Electroosmotic-Darcy number, compares the electrical force on the polymer with the osmotic force due to the thermodynamics of its mixing. Da is the well-known Darcy number which represents the dimensionless permeability of the polymer. η is the solvent to polymer viscosity ratio and Λ is the relative charge on the polymer to ion concentration in solution. The Peclet number Pe compares the convection of the cations due to the fluid's electroosmotic flow relative to the polymer, with the diffusion of the cations. t_c is the cationic transference number. The stars in the superscript denoting nondimensional parameters are promptly dropped for compactness of notation.

For perfectly flat, parallel electrodes, the above problem can be solved to obtain,

$$\mathbf{u}_F = 0 \qquad \mathbf{u}_P = 0 \qquad \mathbf{Q} = \mathbf{I} \qquad \phi = \frac{1}{4\mathrm{Ed}^2}\left(k_2 - \Phi\right)^2$$

$$C_a = C_{a0}\exp\left(\Phi\right) \qquad C_c = C_{a0}\exp\left(\Phi\right) - \frac{\Lambda}{4\mathrm{Ed}^2}\left(k_2 - \Phi\right)^2 \tag{5.25}$$

where the constants k_2 and C_{a0} are determined with the current density J by solving the following three equations simultaneously,

$$J\left(1 + \Lambda\phi_0\right) = C_{a0}^2\left\{e^{2V_0} - 1\right\} - \frac{\Lambda}{4\mathrm{Ed}^2}C_{a0}\left\{e^{V_0}\left(k_2 - V_0\right)^2 - k_2^2\right\} \tag{5.26}$$

$$J = 2C_{a0}\left\{e^{V_0} - 1\right\} - \frac{\Lambda}{4\mathrm{Ed}^2}V_0\left\{\left(\frac{1}{2}V_0 - k_2 + 1\right)^2 + \frac{1}{12}V_0^2 - 1\right\} \tag{5.27}$$

$$4\mathrm{Ed}^2\phi_0 J = 2C_{a0}\left\{\left[e^{2V_0}-1\right]\left[1+\left(k_2-V_0+1\right)^2\right]+V_0^2-2V_0-2k_2V_0\right\} + \frac{\Lambda}{4\mathrm{Ed}^2}\left\{k_2^4\left[\frac{1}{2}-\frac{k_2}{5}\right]-\left(k_2-V_0\right)^4\left[\frac{1}{2}-\frac{k_2-V_0}{5}\right]\right\} \tag{5.28}$$

The nondimensionalized ion concentrations, polymer volume fraction and electric potential are shown in Figure 5.1. The cation and anion concentrations follow their well-known linear profiles in the low current density case, indicating that ambipolar diffusion is the mode of transport here. This is mainly due to the low density of the charge on the polyelectrolyte relative to the ion concentration in solution, which does not appreciably modify charge transport in the inter-electrode region. The polymer volume fraction variation, however, reveals an important feature of the transport problem. The negatively charged polymer undergoes electrophoresis under the electric field and moves away from the metal electrode. Since the presence of the polyelectrolyte is not critical to the ion transport in the electrolyte which can adequately be carried out by the added salt, the polymer gets depleted at the metal electrode at a critical current density. Above this current density, the polyelectrolyte may no longer be effective in the modification of the instability due to its absence from the vicinity of the metal. This critical current density (J^P_{cr}) or transport overpotential (V^P_{cr}) may be calculated by setting $\phi = 0$ at $z = 0$ in the above equations and is shown in Figure 5.2. We see that the critical current density increases with a weaker charge on the polymer since the reduced polymer charge also reduces its electrophoretic mobility. For the positively charged polymer, the polymer is carried by the electric field toward the metal electrode.

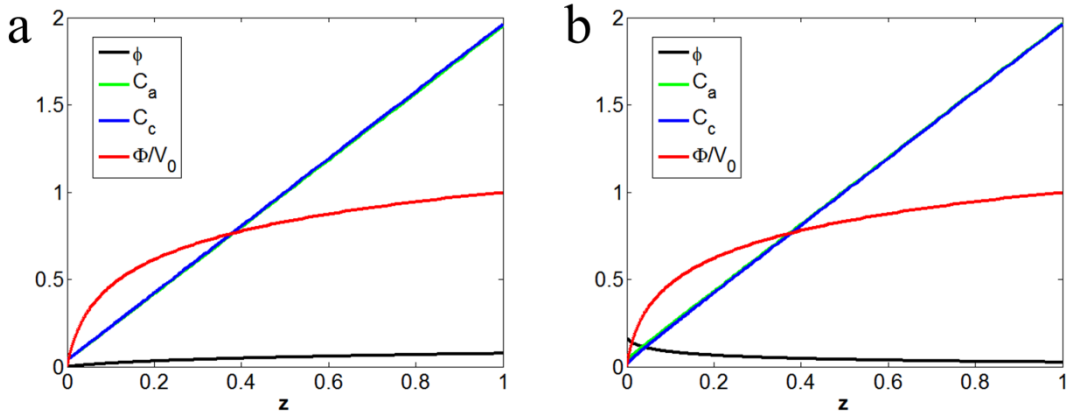

Figure 5.1: Cation and anion concentration, electric potential and polymer volume fraction profiles for $FV_0/RT = 4$ at current densities below the diffusion limit, $\phi_0 = 0.05$ (a) $\Lambda = -0.73\times10^{-10}$ C/m, i.e. $n = 2$, $z_P = -1$ and (b) $\Lambda = 0.73\times10^{-10}$ C/m, i.e. $n = 2$, $z_P = +1$. The metal electrode is at z = 0.

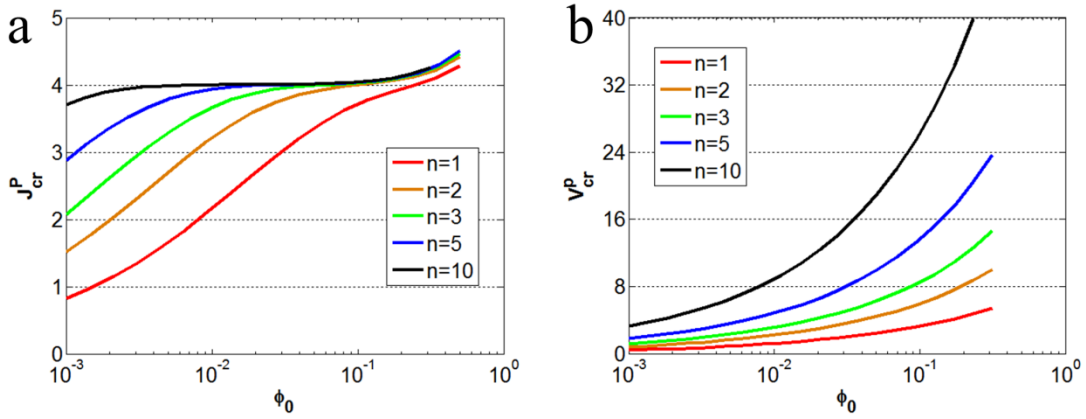

Figure 5.2: (a) Critical current density and (b) Critical transport overpotential for depletion of negatively charged polymer with $z_P = -1$ at the metal electrode as a function of volume fraction for various values of n.

5.3 Linear stability analysis at low current densities

The perturbed, nondimensional mass and momentum equations for the polymer phase and the polymer-fluid mixture are as follows:

$$\nabla\cdot\left(\phi\mathbf{u}_P'\right)=\nabla\cdot\mathbf{u}_F'=0 \tag{5.29}$$

$$-\nabla\left(\phi\phi'\right)+\mathbf{F}_P'-\mathbf{F}_D'=0 \tag{5.30}$$

$$-\nabla p' - \nabla\left(\phi\phi'\right) + \mathbf{F}_P' + \mathrm{Ed}^{-1}\,\mathrm{Da}\,\nabla^2\mathbf{u}_F' = 0 \tag{5.31}$$

where the polymer force density $\mathbf{F}_P'$ and Darcy force density $\mathbf{F}_D'$ are,

$$\mathbf{F}_P' = \mathrm{Ed}^{-1}\,\mathrm{Da}\,\phi^{15/4}\left[\nabla^2\mathbf{u}_P' + \frac{1}{3}\nabla\nabla\cdot\mathbf{u}_P' + \frac{15}{4}\frac{\nabla\phi}{\phi}\cdot\left\{\nabla\mathbf{u}_P' + \left(\nabla\mathbf{u}_P'\right)^{\dagger} - \frac{2}{3}\left(\nabla\cdot\mathbf{u}_P'\right)\mathbf{I}\right\}\right] \tag{5.32}$$

$$\mathbf{F}_D' = \mathrm{Ed}^{-1}\,\phi^{3/2}\left[\eta\mathbf{u}_P' - \mathbf{u}_F' + \nabla\Phi' + \frac{3}{2}\frac{\phi'}{\phi}\nabla\Phi\right] \tag{5.33}$$

The nondimensional cation and anion transport equations are,

$$\mathrm{Pe}\,\mathbf{u}_F'\cdot\nabla C_c = \nabla^2 C_c' + \nabla\cdot\left[C_c'\nabla\Phi + C_c\nabla\Phi'\right] \tag{5.34}$$

$$\frac{\mathrm{Pe}\,t_c}{1-t_c}\mathbf{u}_F'\cdot\nabla C_a = \nabla^2 C_a' - \nabla\cdot\left[C_a'\nabla\Phi + C_a\nabla\Phi'\right] \tag{5.35}$$

$$C_c' = C_a' - \Lambda\phi' \tag{5.36}$$

The perturbation parameters have a specific form: $\phi' = \varphi(z)e^{ikx+\sigma t}$,

$\mathbf{u}_F' = u_{Fx}(z)e^{ikx+\sigma t}\hat{\mathbf{x}} + u_{Fz}(z)e^{ikx+\sigma t}\hat{\mathbf{z}}$, $\mathbf{u}_P' = u_{Px}(z)e^{ikx+\sigma t}\hat{\mathbf{x}} + u_{Pz}(z)e^{ikx+\sigma t}\hat{\mathbf{z}}$,

$\Phi' = \mathrm{P}(z)e^{ikx+\sigma t}$, $\mathbf{F}_P' = F_{Px}'(z)e^{ikx+\sigma t}\hat{\mathbf{x}} + F_{Pz}'(z)e^{ikx+\sigma t}\hat{\mathbf{z}}$,

$\mathbf{F}_D' = F_{Dx}'(z)e^{ikx+\sigma t}\hat{\mathbf{x}} + F_{Dz}'(z)e^{ikx+\sigma t}\hat{\mathbf{z}}$. Here $\hat{\mathbf{z}}$ is the unit vector in the *z*-direction, normal to the surface, while $\hat{\mathbf{x}}$ is the unit vector in the *x*-direction, parallel to the surface. This gives,

$$iku_{Px} + \frac{du_{Pz}}{dz} + \frac{u_{Pz}}{\phi}\frac{d\phi}{dz} = 0 \tag{5.37}$$

$$iku_{Fx} + \frac{du_{Fz}}{dz} = 0 \tag{5.38}$$

The *x*- and *z*- momentum equations for the polymer become,

$$-ik\phi\varphi + F'_{Px} - \mathrm{Ed}^{-1}\,\phi^{3/2}\left[\eta u_{Px} - u_{Fx} + ik\mathrm{P}\right] = 0 \tag{5.39}$$

$$-\frac{d}{dz}\left(\phi\varphi\right) + F'_{Pz} - \mathrm{Ed}^{-1}\,\phi^{3/2}\left[\eta u_{Pz} - u_{Fz} + \frac{d\mathrm{P}}{dz}\right] + \frac{3}{2}\varphi\frac{d\phi}{dz} = 0 \tag{5.40}$$

Simplifying these, we get,

$$\frac{\phi^{3/2}}{ik}\frac{d}{dz}\left(\frac{F'_{Px}}{\phi^{3/2}}\right) - \mathrm{Ed}^{-1}\,\phi^{3/2}\frac{d}{dz}\left[\eta\frac{u_{Px}}{ik} - \frac{u_{Fx}}{ik}\right] = F'_{Pz} - \mathrm{Ed}^{-1}\,\phi^{3/2}\left[\eta u_{Pz} - u_{Fz}\right] \tag{5.41}$$

Taking the curl of the momentum equation for the polymer-fluid mixture, we get,

$$ikF'_{Pz} - \frac{dF'_{Px}}{dz} + \mathrm{Ed}^{-1}\,\mathrm{Da}\left(\frac{d^2}{dz^2} - k^2\right)\left(iku_{Fz} - \frac{du_{Fx}}{dz}\right) = 0 \tag{5.42}$$

To solve the above problem, we use a linear expansion of the base state volume fraction field around $z = 0$. This gives,

$$\phi = \phi\big|_{z=0} + z\left(\frac{d\phi}{dz}\right)\bigg|_{z=0} \tag{5.43}$$

We then observe from the base state that $\phi^{-1}\left(d\phi/dz\right)\big|_{z=0} = O(1) \ll k$. This, then, motivates regular perturbation expansions of the governing equations in terms of $g = \left(k\phi\right)^{-1}\left(d\phi/dz\right)\big|_{z=0}$. To the leading order, the polymer is assumed to have a uniform volume fraction equal to its value at the metal surface, and thus has constant properties corresponding to that volume fraction. The first order in *g* then gives the nature of the flow due to concentration variation of the polymer. Using the continuity equations to eliminate the *x*-components of polymer and fluid velocities, we can get simplified forms of the governing equations, containing the leading order and $O(g)$ terms only with $B = \left(\phi\big|_{z=0}\right)^{1/2}$

$$\begin{aligned}&\mathrm{Da}\,B^{9/2}\left\{\frac{d^4u_{Pz}}{dz^4}-2k^2\frac{d^2u_{Pz}}{dz^2}+k^4u_{Pz}+7gk\left[\frac{d^3u_{Pz}}{dz^3}-k^2\frac{du_{Pz}}{dz}\right]\right\}\\&=\eta\left\{\frac{d^2u_{Pz}}{dz^2}-k^2u_{Pz}+gk\frac{du_{Pz}}{dz}\right\}-\left\{\frac{d^2u_{Fz}}{dz^2}-k^2u_{Fz}\right\}\end{aligned}\tag{5.44}$$

$$\begin{aligned}&-B^{15/2}\left\{\frac{d^4u_{Pz}}{dz^4}-2k^2\frac{d^2u_{Pz}}{dz^2}+k^4u_{Pz}+\frac{17}{2}gk\left[\frac{d^3u_{Pz}}{dz^3}-k^2\frac{du_{Pz}}{dz}\right]\right\}\\&=\frac{d^4u_{Fz}}{dz^4}-2k^2\frac{d^2u_{Fz}}{dz^2}+k^4u_{Fz}\end{aligned}\tag{5.45}$$

The velocities can then be solved to obtain,

$$\begin{aligned}u_{Fz}=&c_3\left(1+gc_{3g}\right)e^{-kz}+gc_2B^{15/2}P_2kze^{-kz}+c_4z\left(1+gc_{4g}-gF_{41}-gF_{42}kz\right)e^{-kz}\\&+c_8\left(1+gc_{8g}+gF_{80}+gF_{81}kz-gP_{82}k_Dkz^2\right)e^{-k_Dz}\end{aligned}\tag{5.46}$$

$$\begin{aligned}u_{Pz}=&c_2\left(1+gc_{2g}-gP_2kz\right)e^{-kz}+\frac{c_4}{\eta}z\left(1+gc_{4g}+gP_{41}+gP_{42}kz\right)e^{-kz}\\&+\frac{c_8}{B^{15/2}}\left(-1-gc_{8g}+gP_{80}-gP_{81}kz+gP_{82}k_Dkz^2\right)e^{-k_Dz}\end{aligned}\tag{5.47}$$

where c_ι and $c_{\iota g}$ are integration constants that need to be determined with boundary conditions. The $P_{\iota\upsilon}$ and $F_{\iota\upsilon}$ are functions defined using,

$$k_P^2=\frac{\eta}{\mathrm{Da}\,B^{9/2}}\qquad k_F^2=\frac{B^{15/2}}{\mathrm{Da}\,B^{9/2}}\qquad k_D^2=k^2+k_P^2+k_F^2\tag{5.48}$$

as,

$$F_{80}=\frac{3}{2}\frac{5kk_D}{k_D^2-k^2}\left[\frac{5k_P^2}{k_D^2-k^2}-3\right]\qquad F_{81}=\frac{3}{8k_D^2}\left[-3k_D^2+k^2+\frac{5}{2}k_P^2+\frac{10k_P^2k_D^2}{k_D^2-k^2}\right]$$

$$P_{82}=\frac{3}{8k_D^2}\left[k_D^2-k^2-\frac{5}{2}k_P^2\right]\qquad F_{41}=\frac{k_F^2}{k_P^2\left(k_D^2-k^2\right)}\left[\frac{k_P^2+3k^2}{2}+\frac{15}{8}k_P^2\frac{k_D^2-5k^2}{k_D^2-k^2}\right]$$

$$F_{42}=\frac{15}{8}\frac{k_F^2}{k_D^2-k^2}\qquad P_2=\frac{k_P^2}{2\left(k_D^2-k^2\right)}\qquad P_{80}=\frac{3}{2}\frac{5kk_D}{k_D^2-k^2}\left[\frac{5k_F^2}{k_D^2-k^2}+\frac{7}{3}\right]$$

$$P_{81} = F_{81} - \frac{15}{4} \qquad P_{41} = \frac{k_P^2}{k_F^2} F_{41} - \frac{17}{8} \qquad P_{42} = \frac{k_P^2}{k_F^2} F_{42} - \frac{17}{8} \tag{5.49}$$

The boundary conditions are also written at the leading order and $O(g)$, which gives the following equations for the constants,

$$c_3 + c_8 = \frac{\sigma}{\mathrm{Pe}} \qquad c_2 - \frac{c_8}{B^{15/2}} = \frac{\sigma}{\eta\,\mathrm{Pe}} \qquad c_3 c_{3g} + c_8\left(c_{8g} + F_{80}\right) = 0$$

$$c_2 c_{2g} + \frac{c_8}{B^{15/2}}\left(-c_{8g} + P_{80}\right) = 0 \qquad c_2\left(2k^2 + \frac{k}{b}\right) - \frac{c_4}{\eta}\left(2k + \frac{1}{b}\right) - \frac{c_8}{B^{15/2}}\left(k_D^2 + k^2 + \frac{k_D}{b}\right) = 0$$

$$c_2\left[\left(c_{2g} + P_2\right)\left(2k^2 + \frac{k}{b}\right) - k^2 - \frac{k}{b}\right] - \frac{c_4}{\eta}\left[\left(c_{4g} + P_{41}\right)\left(2k + \frac{1}{b}\right) - k - 2kP_{42}\right]$$
$$+ \frac{c_8}{B^{15/2}}\left[\left(-c_{8g} + P_{80}\right)\left(k_D^2 + k^2 + \frac{k_D}{b}\right) + P_{81}\left(2k_D k + \frac{k}{b}\right) + 2P_{82}k_D k + k_D k + \frac{k}{b}\right] = 0$$

$$c_2 B^{15/2} P_2 k + c_4\left(c_{4g} - F_{41}\right) - k c_3 c_{3g} - c_8\left(k_D c_{8g} + k_D F_{80} - k F_{81}\right) = 0$$

$$-k c_3 + c_4 - k_D c_8 = U_{eo} k^4 \tag{5.50}$$

where U_{eo} is obtained as the comparison between two velocity scales viz. interface-driven electroosmotic slip and the electroosmotic slip due to the polymer charge as,

$$U_{eo} = \frac{\varepsilon\gamma\nu_m}{\Lambda RTL}\left(\zeta + \frac{RT}{F}\ln 4\right) \tag{5.51}$$

This can, in turn, be used to obtain the perturbation growth rate as,

$$\sigma = \nu_m\left[kJ - \frac{\gamma\nu_m}{RT}c_0^* k^3 + 2\left(k - k_D\right)A_D + 2B_D + 2B_C\right] \tag{5.52}$$

where,

$$A_D = \frac{J}{4}\frac{\mathrm{Pe}}{1 - t_c}\left[\frac{c_8 + g c_8 c_{8g} + g c_8 F_{80}}{k_D^2 - k^2} + \frac{2gkk_D c_8 F_{81}}{\left(k_D^2 - k^2\right)^2} - \frac{2gkk_D c_8 P_{82}\left(3k_D^2 + k^2\right)}{\left(k_D^2 - k^2\right)^3}\right] \tag{5.53}$$

$$B_D = \frac{J}{4}\frac{\mathrm{Pe}}{1-t_c}\left[\frac{gkc_8F_{81}}{k_D^2-k^2} - \frac{4gkk_D^2c_8P_{82}}{\left(k_D^2-k^2\right)^2}\right] \tag{5.54}$$

$$B_C = -\frac{J}{4}\frac{\mathrm{Pe}}{1-t_c}\left[\frac{c_3+gc_3c_{3g}}{2k} + \frac{c_4+gc_4\left(c_{4g}-F_{41}-F_{42}\right)+gc_2B^{15/2}P_2k}{4k^2}\right] \tag{5.55}$$

The above result is plotted in Fig 5.3. As can be seen, neither the volume fraction of the polymer nor the charge on the polymer has any significant effect on the stability of deposition. This result can be understood by examining equation (5.41) closely, which shows that the electric field induced concentration variations of the polymer induces two conflicting effects – osmotic stress driven flow of the polymer and a spatial variation in the electrophoresis of the polymer, which cancel each other. The latter effect was not predicted in our earlier hypothesis. Thus the applied electric field does not cause any net motion of the polymer or the fluid and the convection is driven entirely by the electroosmotic flow at the metal surface. The Peclet number for this flow calculated using the values – $\varepsilon = 81 \times 8.85 \times 10^{-12}$ Farads/m, $\nu_m = 1.33 \times 10^{-5}$ m^3/mol, $\gamma = 1.716$ N/m, $\zeta = 3$ V, $L = 1$ mm, and the product $\eta_F D_c = 1.12 \times 10^{-5}$ Pa·m^2/s is [11],

$$\mathrm{Pe}_{eo} = \frac{\varepsilon\gamma\nu_m}{FL\eta_F D_c}\left(\zeta + \frac{RT}{F}\ln 4\right) \approx 5.6\times10^{-4} \tag{5.56}$$

While the drag exerted by the polymer on the fluid damps this convection, the Peclet number for this flow is small. Thus, the electroconvection has an insignificant contribution to the stability of deposition. Hence, at current densities below the diffusion limit, controlling the electroconvection with polyelectrolytes does not improve the stability of electrodeposition appreciably.

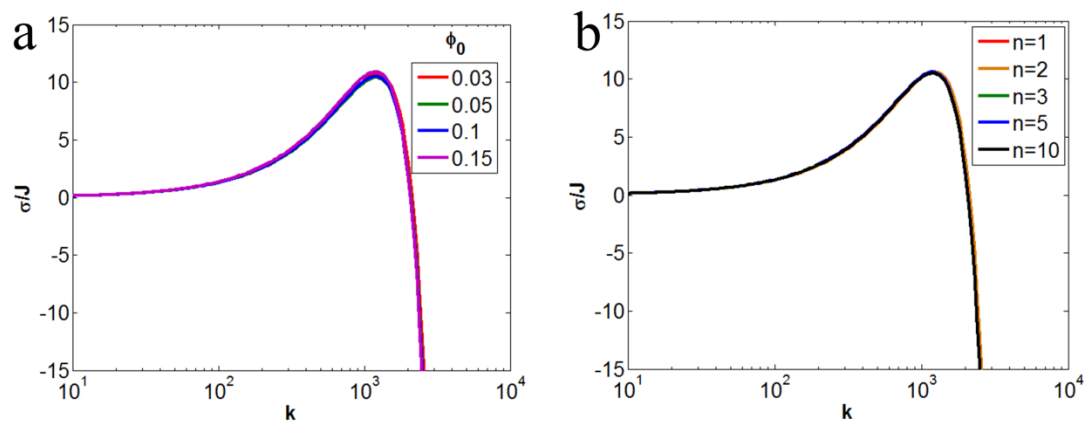

Figure 5.3: Growth rate versus wavenumber for z_P = -1 and varying values of (a) Equilibrium polymer concentration ϕ_0 with n = 2 and (b) ϕ_0 = 0.05 and varying values of n.

5.4 Electroconvection at high current densities

At or above the diffusion limited current density, the electric field diverges at the metal electrode in steady state. As a constant current is passed between the electrodes, the cations are consumed at the metal electrode and regenerated at the counter electrode. At a critical time called the Sand's time [12], the cation concentration at the metal surface drops to zero and a space charge region forms near the metal surface. A negatively charged polyelectrolyte will then be depleted at the metal surface and is no longer effective at modifying the electroconvection. For this reason, we consider the effect of uncharged polymers as additives to modify the electroconvection at high current densities.

To incorporate the role of convective instability, we restore the time-dependent terms in the governing equations. This gives,

$$\frac{\partial \phi}{\partial t} + \nabla \cdot \left(\phi \mathbf{u}_P \right) = 0 \tag{5.57}$$

$$-\frac{\partial \phi}{\partial t}+\nabla\cdot\mathbf{u}_F=0 \tag{5.58}$$

$$-\phi\nabla\phi+\mathrm{Ed}^{-1}\,\mathrm{Da}\,\phi^{15/4}\left[\nabla^2\mathbf{u}_P+\frac{1}{3}\nabla\nabla\cdot\mathbf{u}_P\right]-\mathrm{Ed}^{-1}\,\phi^{3/2}\left[\eta\mathbf{u}_P-\mathbf{u}_F\right]=0 \tag{5.59}$$

$$-\nabla p+\mathrm{Ed}^{-1}\,\mathrm{Da}\,\nabla^2\mathbf{u}_F+\mathrm{Ed}^{-1}\,\phi^{3/2}\left[\eta\mathbf{u}_P-\mathbf{u}_F\right]=0 \tag{5.60}$$

The cation and anion concentrations evolve as,

$$\frac{\partial C_c}{\partial t}+\mathrm{Pe}\,\mathbf{u}_F\cdot\nabla C_c=\nabla^2 C_c+\nabla\cdot\left[C_c\nabla\Phi+C_c\nabla\Phi\right] \tag{5.61}$$

$$\frac{t_c}{1-t_c}\left[\frac{\partial C_a}{\partial t}+\mathrm{Pe}\,\mathbf{u}_F\cdot\nabla C_a\right]=\nabla^2 C_a-\nabla\cdot\left[C_a\nabla\Phi+C_a\nabla\Phi\right] \tag{5.62}$$

$$C_c=C_a \tag{5.63}$$

The boundary conditions are the same as before with two exceptions. The electroosmotic slip of the fluid takes a different form corresponding to electrooosmosis of the second kind as obtained by Rubinstein and Zaltzmann [10]. The second difference is that the salt is depleted at the metal surface.

$$\mathbf{n}\cdot\mathbf{u}_F=\frac{1}{\mathrm{Pe}}\frac{\partial H}{\partial t}\qquad \mathbf{n}\cdot\mathbf{u}_P=\frac{1}{\eta\,\mathrm{Pe}}\frac{\partial H}{\partial t}\qquad (\mathbf{I}-\mathbf{nn})\cdot\mathbf{u}_P=b(\mathbf{I}-\mathbf{nn})\mathbf{n}:(\mathbf{Q}-\mathbf{I})$$

$$(\mathbf{I}-\mathbf{nn})\cdot\mathbf{u}_F=-\frac{V_0^2}{8}(\mathbf{I}-\mathbf{nn})\cdot\nabla\ln(\mathbf{n}\cdot\nabla C_c)$$

$$-J=\mathbf{n}\cdot\left[-\nabla C_c-C_c\nabla\Phi\right]=\frac{1}{\nu_m}\frac{\partial H}{\partial t}\qquad 0=\mathbf{n}\cdot\left[-\nabla C_a+C_a\nabla\Phi\right]$$

$$\Phi(z=0)=0,\ \Phi(z=L)=V_0\ \text{ and }\ C_c(z=0)=0 \tag{5.64}$$

The base state solution can be obtained as,

$$\mathbf{u}_F=0\qquad \mathbf{u}_P=0\qquad \mathbf{Q}=\mathbf{I}\qquad \phi=\phi_0 \tag{5.65}$$

The cation and anion concentrations are obtained from Sand's result as,

$$c = C_c = C_a = 1 - \frac{J}{4} + \frac{J}{2} z + \frac{2J}{\pi^2} \sum_{n=1}^{\infty} \frac{\cos\left[(2n-1)\pi z\right] \exp\left[-(2n-1)^2 \pi^2 t\right]}{(2n-1)^2} \quad (5.66)$$

This concentration profile is valid up until the Sand's time, at which the salt is completely depleted at the metal electrode. This is shown in Fig 5.4. At the Sand's time, the depletion of the salt near the metal surface creates a space charge region with very high electric fields. This can drive an electroconvective instability called electroosmosis of the second kind, which allows for the passage of current above the diffusion limit. However, the convection rolls of electroosmosis of the second kind can also enhance the growth of morphological instabilities at the surface.

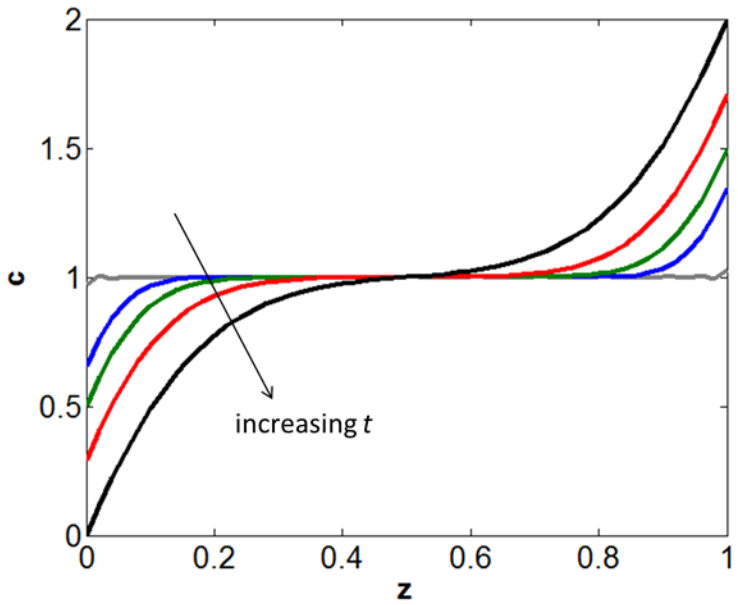

Figure 5.4: Evolution of the salt concentration with time. The current density used here is four times the diffusion limit. The black line shows the profile at Sand's time.

To perform linear stability analysis, we start with the concentration profile at Sand's time. We only consider perturbations with wavelengths smaller than the interelectrode distance, i.e. $k >> 1$ and study the growth of perturbations with a quasi-steady base state. This lets us write the local concentration distribution as,

$$c = C_c = C_a = \frac{J}{2} z \tag{5.67}$$

As before, the perturbations follow as $\phi' = \phi'(z) e^{ikx+\sigma t}$, $C_c' = C_c'(z) e^{ikx+\sigma t}$, $\mathbf{u}_F' = u_{Fx}(z) e^{ikx+\sigma t} \hat{\mathbf{x}} + u_{Fz}(z) e^{ikx+\sigma t} \hat{\mathbf{z}}$, $\mathbf{u}_P' = u_{Px}(z) e^{ikx+\sigma t} \hat{\mathbf{x}} + u_{Pz}(z) e^{ikx+\sigma t} \hat{\mathbf{z}}$. The perturbed equations thus are,

$$\sigma \phi' + \nabla \cdot (\phi \mathbf{u}_P') = 0 \tag{5.68}$$

$$-\sigma \phi' + \nabla \cdot \mathbf{u}_F' = 0 \tag{5.69}$$

$$-\phi_0 \nabla \phi' + \mathrm{Ep}\,\mathrm{Da}\, \phi_0^{15/4} \left[\nabla^2 \mathbf{u}_P' + \frac{1}{3} \nabla \nabla \cdot \mathbf{u}_P' \right] - \mathrm{Ep}\, \phi_0^{3/2} \left[\eta \mathbf{u}_P' - \mathbf{u}_F' \right] = 0 \tag{5.70}$$

$$-\nabla p' + \mathrm{Ep}\,\mathrm{Da}\, \nabla^2 \mathbf{u}_F' + \mathrm{Ep}\, \phi_0^{3/2} \left[\eta \mathbf{u}_P' - \mathbf{u}_F' \right] = 0 \tag{5.71}$$

The electroosmotic Darcy number has been replaced with the electroosmotic Peclet number for the polymer as $\mathrm{Ep} = \varepsilon R^2 T^2 / F^2 \xi_0^2 \chi_0^{-1}$, and it gives the Peclet number for the polymer under the flow driven by the second kind electroosmosis. The cation and anion concentrations evolve as,

$$\sigma C_c' + \mathrm{Pe}\, \mathbf{u}_F' \cdot \nabla C_c = \nabla^2 C_c' + \nabla \cdot \left[C_c' \nabla \Phi + C_c \nabla \Phi' \right] \tag{5.72}$$

$$\frac{t_c}{1 - t_c} \left[\sigma C_a' + \mathrm{Pe}\, \mathbf{u}_F' \cdot \nabla C_a \right] = \nabla^2 C_a' - \nabla \cdot \left[C_a' \nabla \Phi + C_a \nabla \Phi' \right] \tag{5.73}$$

$$C_c' = C_a' \tag{5.74}$$

These can be solved to obtain,

$$\phi' = A_\phi e^{-k_\phi z} \tag{5.75}$$

$$u_{Fz} = \left(c_3 + c_4 z\right) e^{-kz} + c_8 e^{-k_D z} - \frac{\sigma k_\phi A_\phi}{k_\phi^2 - k^2} e^{-k_\phi z} \tag{5.76}$$

$$u_{Pz} = \left(c_2 + \frac{c_4}{\eta} z\right) e^{-kz} - \frac{c_8}{\phi_0^{15/4}} e^{-k_D z} + \frac{\sigma k_\phi A_\phi}{\phi_0 \left(k_\phi^2 - k^2\right)} e^{-k_\phi z} \tag{5.77}$$

$$C_c' = A_c e^{-k_c z} + \frac{\mathrm{Pe}\, J}{4\left(1 - t_c\right)} \left\{ \begin{array}{l} \dfrac{B_\phi e^{-k_\phi z}}{k_\phi^2 - k_c^2} \left[\dfrac{2\left(k_\phi^2 - k^2\right)}{k_\phi^2 - k_c^2} - 1 + z \dfrac{\left(k_\phi^2 - k^2\right)}{k_\phi} \right] \\ + \dfrac{c_8 e^{-k_D z}}{k_D^2 - k_c^2} + \dfrac{\left(c_3 + c_4 z\right)\left(k^2 - k_c^2\right) + 2c_4 k}{\left(k^2 - k_c^2\right)^2} e^{-kz} \end{array} \right\} \tag{5.78}$$

where B_ϕ, A_c, c_2, c_3, c_4 and c_8 are integration constants and,

$$k_\phi^2 = k^2 + \frac{\mathrm{Ep}\, \phi_0^{\frac{1}{2}} \left(1 + \eta / \phi_0\right) \sigma}{1 + \frac{4}{3} \mathrm{Ep}\, \mathrm{Da}\, \phi_0^{\frac{7}{4}} \sigma} \qquad\qquad k_c^2 = k^2 + \frac{\sigma}{2\left(1 - t_c\right)} \tag{5.79}$$

The boundary conditions give a set of equations with which to determine the integration constants. These are,

$$c_3 + c_8 - B_\phi = \frac{\sigma}{\mathrm{Pe}} \tag{5.80}$$

$$c_2 - \frac{c_8}{\phi_0^{15/4}} + \frac{B_\phi}{\phi_0} = \frac{\sigma}{\eta\, \mathrm{Pe}} \tag{5.81}$$

$$\eta c_2 - c_3 + \frac{2c_4 k}{k_P^2} = 0 \tag{5.82}$$

$$\left(-k c_2 + \frac{c_4}{\eta}\right)\left(1 + 2bk\right) + \frac{c_8}{\phi_0^{15/4}} \left(k_D + bk^2 + bk_D^2\right) = \frac{B_\phi}{\phi_0} \frac{k^2}{k_\phi} \left(1 + 2bk_\phi\right) \tag{5.83}$$

$$\frac{\sigma}{2v_m}\frac{k^2V_0^2}{4J} = -B_\phi\frac{k^2}{k_\phi} + kc_3 - c_4 + k_D c_8 \tag{5.84}$$

$$A_c + \frac{\mathrm{Pe}\,J}{4(1-t_c)}\left\{\frac{B_\phi}{k_\phi^2-k_c^2}\left[\frac{2\left(k_\phi^2-k^2\right)}{k_\phi^2-k_c^2}-1\right] + \frac{c_8}{k_D^2-k_c^2} + \frac{c_3\left(k^2-k_c^2\right)+2c_4k}{\left(k^2-k_c^2\right)^2}\right\} = -\frac{J}{2} \tag{5.85}$$

$$\frac{\sigma}{2v_m} = -k_c A_c + \frac{\mathrm{Pe}\,J}{4(1-t_c)}\left\{\begin{array}{l}\dfrac{k_\phi B_\phi}{k_\phi^2-k_c^2}\left[1-\dfrac{\left(k_\phi^2+k_c^2\right)\left(k_\phi^2-k^2\right)}{k_\phi^2\left(k_\phi^2-k_c^2\right)}\right] - \dfrac{k_D c_8}{k_D^2-k_c^2} \\ -\dfrac{kc_3\left(k^2-k_c^2\right)+c_4\left(k^2+k_c^2\right)}{\left(k^2-k_c^2\right)^2}\end{array}\right\} \tag{5.86}$$

The above analysis gives three equations,

$$\sigma\left(\frac{1}{\mathrm{Pe}}-\frac{kV^2}{2v_m\cdot 4J}\right) + B_\phi\left[1-\frac{k}{k_\phi}-\frac{k_P^2}{2k^2}\left(1+\frac{\eta}{\phi_0}\right)\right] + c_8\left[\frac{k_D}{k}-1-\frac{k_P^2}{2k^2}\left(1+\frac{\eta}{\phi_0^{15/4}}\right)\right] = 0 \tag{5.87}$$

$$\frac{\sigma}{2v_m}\frac{kV^2}{4J} + \frac{B_\phi}{\phi_0}\left[\frac{k}{k_\phi}\left\{\frac{\eta}{1+2bk}+\phi_0\right\} - \left\{1+\frac{\eta}{1+2bk}\right\}\right] - c_8\left[\frac{k_D}{k}-1\right]\left[1+\frac{\eta}{\phi_0^{15/4}}\frac{1+bk+bk_D}{1+2bk}\right] = 0 \tag{5.88}$$

$$\sigma\left(\frac{1}{v_m}-\frac{J}{2(1-t_c)(k+k_c)}\right) - k_c J = \frac{\mathrm{Pe}\,J}{2(1-t_c)}\left\{\begin{array}{l} B_\phi\left[\dfrac{k_\phi k_c+k^2}{k_\phi\left(k_\phi+k_c\right)^2}-\dfrac{1}{k+k_c}-\dfrac{k_P^2/2k}{\left(k+k_c\right)^2}\left(1+\dfrac{\eta}{\phi_0}\right)\right] \\ +c_8\left[\dfrac{1}{k+k_c}-\dfrac{1}{k_D+k_c}-\dfrac{k_P^2/2k}{\left(k+k_c\right)^2}\left(1+\dfrac{\eta}{\phi_0^{15/4}}\right)\right]\end{array}\right\} \tag{5.89}$$

which can be solved for σ, B_ϕ and c_8, while remembering that k_ϕ and k_c depend implicitly on σ as given in (5.79).

Before looking at the results of the two-fluid model, it is useful to study the evolution of the instability in a Newtonian fluid as a benchmark. The above problem is solved by setting the polymer volume fraction to zero to obtain the single fluid Newtonian model. As a special case to that, the growth of the interface due to the

transport of ions to its surface is turned off. This yields the growth of the electroconvective component of the instability, which has an analytical form also seen in Rubinstein and Zaltzman [10],

$$\sigma = 2\left(1-t_c\right)k^2\left[\frac{V_0^2\,\mathrm{Pe}}{16\left(1-t_c\right)} - \frac{V_0}{2}\sqrt{\frac{\mathrm{Pe}}{1-t_c}}\right] \tag{5.90}$$

The growth rates with wavenumber of the purely hydrodynamic instability and the coupled hydrodynamic and morphological instability are shown in Fig 5.5. As seen, the growth rates of the two instabilities are very close at all wavenumbers with a scaling of k^2, reflective of the above analytical result for the electroconvective instability. This suggests that the growth of the interface is strongly driven by electroconvective instability, with the contribution of the diffusive mechanism being negligible. A simple prediction would then be that if the hydrodynamic instability is damped by the polymer, the instability in the presence of polymer additives should grow at a different rate reflective of the diffusive transport in the interelectrode gap.

We now return to the instability in the two-fluid system. The growth rate versus wavenumber plots for various values of polymer molecular weight and volume fraction are shown in Fig 5.6. Decreasing the polymer viscosity by reducing the index of polymerization, allows for easier convection of the polymer due to the drag exerted by the fluid as seen from Fig 5.6a. This, in turn, reduces the damping effect of the polymer on the fluid's electroosmotic flow and the instability growth is similar to that without the polymer.

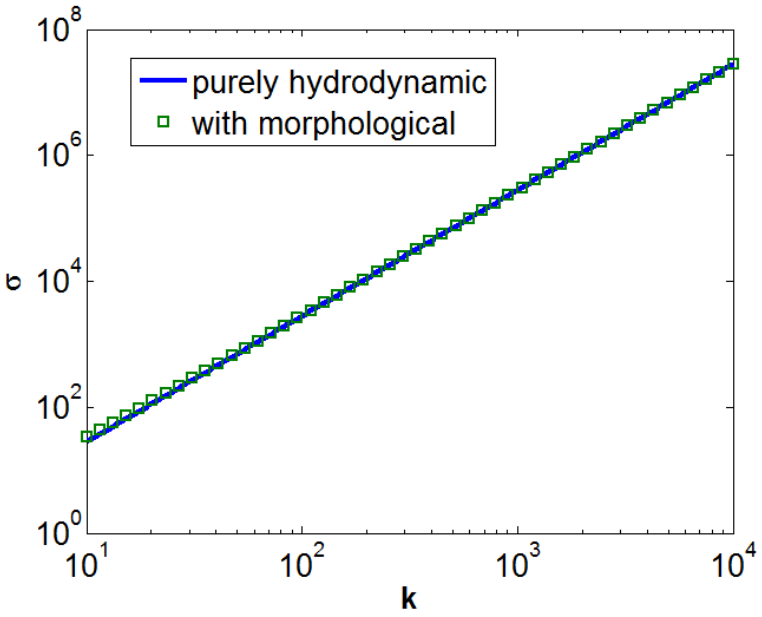

Figure 5.5: Linear growth rates of the purely electroconvective and electroconvective and morphological instabilities in a Newtonian fluid

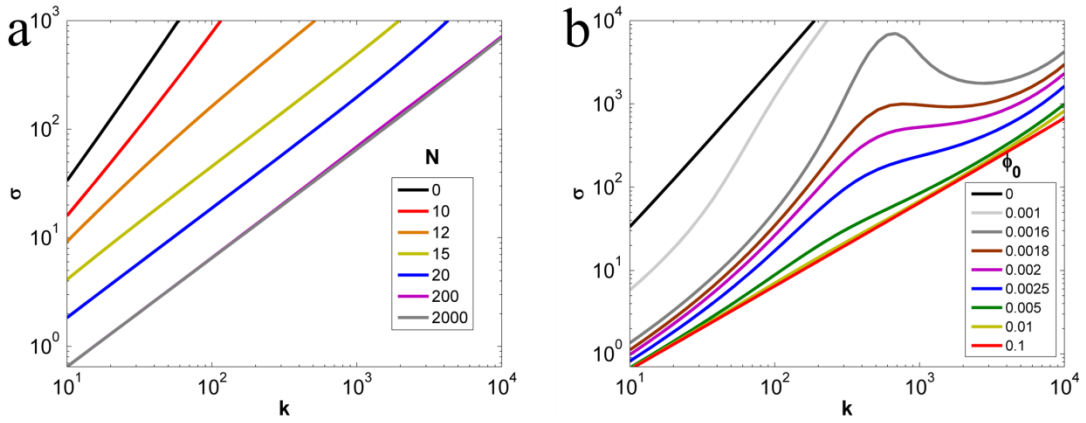

Figure 5.6: Growth rate versus wavenumber varying values of (a) Polymerization index N at $\phi_0 = 0.05$ and (b) Volume fraction ϕ_0 for N = 2000.

A similar effect is seen when the polymer volume fraction is varied. For volume fractions of 0.1%, we find that the behavior of the instability growth is similar to that of the Newtonian fluid. At higher fractions of 5% and 10%, the

electroconvection is completely damped by the polymer and the instability growth rate deviates from the previously seen k^2 scaling law and instead grows as k due the nature of unstable diffusive transport of ions in the electrolyte. This scaling as k is the same as the one seen in previous chapters. Unlike the index of polymerization, the volume fraction affects a wide range of system properties, and hence has a much more complex effect on the nature of the curves in Fig 5.6b. For volume fractions of 0.0016, 0.0018 and 0.002, the ratio of the viscosities of the polymer and fluid is finite. In this case, as k increases, so does the strength of the electroconvective instability. As a result, the polymer starts to move, and the growth rate goes from its diffusive k behavior to the convective k^2 variation. At large enough k values, the growing surface compresses the polymer, which in turn damps the fluid motion and suppresses the instability. This is reflected in the observed maximum in the growth rate.

5.5 Conclusion

We have thus shown that polymer additives are effective in modifying electroconvection in electrodeposition. At low current densities, the electroconvection is driven primarily by interfacial tension of the metal-electrolyte interface and is a weaker transport mechanism relative to the diffusion of ions in the electrolyte. At high current densities, electroosmosis of the second kind drives a strong flow in the interelectrode region, which can lead to significantly unstable deposition. Entangled polymers can be used as additives in small concentrations in this case. The entanglement of the polymer can give high viscosity that damps the convection, even at small volume fractions that do not impede ion diffusion.

REFERENCES

1. Doi, M. & Onuki, A., Dynamic coupling between stress and composition in polymer solutions and blends. *J. Phys. II* **2 (8)**, 1631-1656 (1992)

2. Fredrickson, G. H., Dynamics and rheology of inhomonegenous polymeric fluids: a complex Langevin approach. *J. Chem. Phys.* **117**, 6810-6820 (2002)

3. Cromer, M., Fredrickson, G. H. & Leal, L. G., A study of shear banding in polymer solutions. *Phys. Fluid.* **26**, 063101 (2014)

4. Peterson, J. D., Cromer, M., Fredrickson, G. H. & Leal, L. G., Shear banding predictions for the two-fluid Rolie-Poly model. *J. Rheol.* **60**, 927–951 (2016)

5. Onsager, L. Reciprocal relations in irreversible processes. II, *Phys. Rev.* **38**, 2265-2279 (1931)

6. Flory, P. J., Theory of elasticity of polymer networks. The effect of local constraints on junctions, *J. Chem. Phys.*, **66 (12)**, 5720-5729 (1977)

7. Likhtman, A. E. & Graham, R. S., Simple constitutive equation for linear polymer melts derived from molecular theory: Rolie-poly equation. *J. Non-Newton. Fluid* **114**, 1-12 (2003)

8. Dobrynin, A. V., Colby, R. H. & Rubinstein, M., Scaling theory for polyelectrolyte solutions, *Macromolecules* **28**, 1859-1871 (1995)

9. Mhetar, V. & Archer, L. A., Slip in entangled polymer solutions. *Macromolecules* **31**, 6639-6649 (1998)

10. Rubinstein, I. & Zaltzman, B., Electro-osmotically induced convection at a perm-selective membrane, *Phys. Rev. E* **62**, 2238-2251 (2000)

11. Kondo, et al., Conductivity and solvation of Li^+ ions of $LiPF_6$ in propylene carbonate solutions, *J. Phys. Chem. B*, **104**, 5040-5044 (2000)

12. Sand, H. J. S. On the concentration at the electrodes in a solution, with special reference to the liberation of hydrogen by electrolysis of a mixture of copper sulphate and sulphuric acid. *Phil. Mag.* **1**, 45-79 (1901)

13. Tao, H., Huang, C., and Lodge, T. P., Correlation length and entanglement spacing in concentrated hydrogenated polybutadiene solutions, *Macromolecules*, **32**, 1212-1217 (1999)

CHAPTER 6

CONCLUDING REMARKS

We have thus seen, four different models based on linear stability analysis to suppress dendritic electrodeposition. The conclusions of each of the model can be summarized as follows,

1. The morphological instability on the metal surface driven by unstable ion transport can be suppressed by immobilizing a fraction of the anions spatially within the electrolyte. Even 10% of immobilization captures most of the stabilization effect.
2. An elastic solid separator can suppress the growth of the instability. Large, metal-like moduli are not required of the separators to suppress the instability completely. Even polymer-like moduli of 10-100 MPa are sufficient.
3. Physicochemical properties of the metal-electrolyte interface have significant influence on the growth of the instability. High ionic diffusivities in the solid-electrolyte interphase can improve the stability of deposition.
4. Electroconvection in the electrolyte can enhance the instability of deposition and dendritic growth and can be effectively suppressed through polymer additives in the electrolyte.

The fixed anions and polymer additives in liquid electrolytes are particularly useful at high current densities where extreme driving forces such as high electric fields and electroconvection drive fast growth of the morphological instability. In contrast, separator elasticity and interfacial modifications can effectively suppress

dendritic deposition at low current densities, which makes them useful for lithium battery applications.

While these studies provide valuable insights into the mechanisms of dendrite growth and their suppression methods, the picture remains largely incomplete. Key among these deficiencies is poor understanding of the role of the interfacial layer. While it is known that the solid-electrolyte interphase is a spontaneously formed physical barrier on the metal surface, its composition, physical and chemical properties are largely unknown. This picture can predominantly be improved by visualization studies that explore the growth of metallic deposits with various chemical entities present at the surface. This can, then, be used to understand the role played by the interfacial layer in the growth of dendrites. Another key effect not included here is the electric field driven modification to the structure and properties of the electrolyte. This may be useful in controlling dendrite growth by allowing for phase transition and modification to charge transport behavior in electrolytes when the electric field increases in the neighborhood of a dendrite tip.

A large class of materials viz. ionic liquids also has not been modeled in theoretical studies. Numerous studies have shown the benefits of ionic liquid and ionic liquid-based electrolytes in improving both the chemical stability of the electrolyte as well as the stability of deposition under them [1, 2]. Previous studies have used Bikerman's model [3, 4] for the electrical double layer to study double layer structure and electrophoresis of charged particles in low dielectric constant solvents such as ionic liquids. These can be incorporated into existing formulations of electroconvection and charge transport. The effect of large salt concentrations on transport properties also

needs to be understood from a theoretical standpoint. Most existing models, including ours, rely on dilute limit simplifications to perform stability analysis of electrodeposition. However, salt solutions in practical systems are rarely dilute in nature, particularly for achieving high conductivities. The Debye-Huckel theory for concentrated solutions is an excellent starting point for such an effort.

On a larger scale, it is useful to understand the effects of various physical phenomena on the morphology of deposits. Such studies can help to explain the difference in the shape of deposits in various metals as well as write design rules to control the structure of metallic deposits as required. These will need the use of nonlinear simulations such as phase-field models and diffusion-limited aggregation, while accounting for the role of the SEI. The effects of electroconvection also require complex simulations to explore the coupled relationship between the hydrodynamic and morphological instabilities. This is particularly true in highly confined systems where the interelectrode gap is comparable to the electrocapillary length as is the case with ultrathin batteries that utilize small quantities of electrolyte.

In summary, it may be said that unstable electrodeposition provide a wide range of fundamental problems for study and serves as an excellent starting point to address the real world problem of dendrite growth in lithium metal batteries. A synergistic approach between theory and experiments can provide systematic strategies to explore a broad range of possible solutions for what is a significant technological challenge of the present times.

REFERENCES

1. Lu, Y., Korf, K., Kambe, Y., Tu, Z., & Archer, L. A. Ionic-liquid-nanoparticle hybrid electrolytes: applications in lithium metal batteries. *Angew. Chem. Int. Ed.* **53**, 488-492 (2014)

2. Al Sadat, W. I. & Archer, L. A. The O_2-assisted Al/CO_2 electrochemical cell: a system for CO_2 capture/conversion and electric power generation. *Sci. Adv.* **2**, e160098 (2016)

3. Bikerman, J. J. XXXIX. Structure and capacity of electrical double layer. *Lond. Edinb. Dubl. Phil. Mag.* **33**, 382-397 (1942)

4. Khair, A. S. & Squires, T. M. Ionic steric effects on electrophoresis of a colloidal particle. *J. Fluid Mech.* **640**, 343–356 (2009)

APPENDIX

Two results not covered in the main thesis are briefly mentioned here:

1. Transient transport concentration plots: Sand's result for concentration as a function of time also applies below the diffusion limited current density. This gives the following concentration profile.

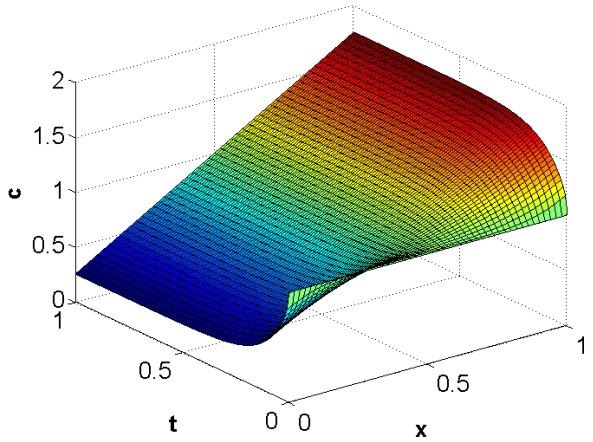

Figure A1: Transient concentration profiles at 3/4th the diffusion limit

The concentration at the metal electrode as a function of time is,

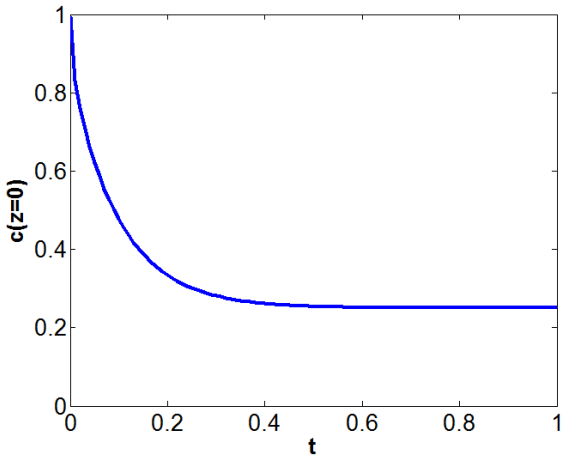

Figure A2: Concentration at the metal electrode over time

This result shows that the cations are never depleted in the interelectrode region at current densities below the diffusion limit.

2. Non-quasisteady perturbed equations

   If the time derivative is included in the transport equations of Section 2, we obtain the growth rate at small current densities as,

$$\sigma = \frac{\dfrac{\nu_m k}{F \tanh kL}\left[J - \dfrac{D_c F \gamma \nu_m k^2 C_c\big|_L}{RT} \right]}{1 + \dfrac{\nu_m C_0}{kL \sinh kL}\left\{1 - \cosh\left[kL\right]\right\}} \tag{A1}$$

   and the large current densities as,

$$\sigma = \frac{\dfrac{\nu_m k}{F \tanh kL}\left[J - \dfrac{D_c F \gamma \nu_m k^2 C_a^f}{RT} \right]}{1 + \dfrac{\nu_m C_0}{kL \sinh kL}\left\{1 - \cosh\left[k\left(L - l\right)\right]\right\}} \tag{A2}$$

   Both modifications to the previous results are small since the molar volume of the metal is much smaller than the salt concentration, which evolves much faster than the metal, thus justifying the quasi steady assumption.